CLS
COLLECTE LOCALISATION SATELLITES

Consortium Members

ESA Sea Level CCI

Climate Assessment Report (CAR)
WP5100: User Assessment
WP5200: MSL Closure Budget

Reference:	CLS-SL_CCI-17-0002
Nomenclature:	SL_CCI-CAR-079
Issue:	2. 1
Date:	Nov. 14, 17

European Space Agency

Chronology Issues:			
Issue:	Date:	Reason for change:	Author
1.0 (DRAFT)	06.08.2015	Updates from v1.2 in phase I	M. Scharffenberg
1.0	22.09.2015	Input of different sub work packages	M. Scharffenberg, M. Balmaseda, J. Johannessen, A. Cazenave, JF Legeais
1.1	09.11.2015	Modification after ESA's review	M. Scharffenberg, M. Balmaseda, J. Johannessen, A. Cazenave, JF Legeais
1.2	23.06.2016	Updates for KO+27 milestone	M. Scharffenberg, H. Zuo
1.3	14/09/2016	Update after ESA's review	JF Legeais, M. Scharffenberg, H. Zuo
2.0	15/05/2017	Final issue for KO+36 of Phase II	M. Scharffenberg, H. Zuo, J. Johannessen, R. R. Raj, J.E. Nilsen, F. Counillon, A. Cazenave
2.1	14/11/2017	Update after ESA's review	S.Mabjon, M. Scharffenberg, H. Zuo, J. Johannessen, J. Legeais

People involved in this issue:		
Written by (*):	CRG	Date + Initials:(visa or ref)
Checked by (*):	S. Mbajon Njiche, G. Timms	Date + Initial:(visa ou ref)
Approved by (*):	J.F. Legeais	Date + Initial:(visa ou ref)
Application authorized by (*):	J. Benveniste	Date + Initial:(visa ou ref)

**In the opposite box: Last and First name of the person + company if different from CLS*

Index Sheet:	
Context:	
Keywords:	Oceanography, sea level

FORM-NT-GB-7-1

Hyperlink:	

Distribution:		
Company	Means of distribution	Names
ESA	Email	Jérôme Benveniste, Americo Ambrozio, Marco Restano
CLS	Email	J.F. Legeais, M. Ablain, G. Larnicol
CGI	Email	Gary Timms
SL_cci team	SL_cci ftp site	

List of tables and figures

List of tables

List of figures

Applicable documents

AD 1 Sea level CCI project Management Plan
CLS-DOS-NT-13-185

List of Acronyms

ACC	Antarctic Circumpolar Current
AMOC	Atlantic Meridional Overturning Circulation

AMSRE	Advanced Microwave Scanning Radiometer Earth Observing System
AT	Along-Track
AVISO	CNES Reference Satellite Altimetry Data Portal
BG	Beaufort Gyre
CAR	Climate Assessment Report
CERA-SAT	ECMWF's Coupled data assimilation system for climate ReAnalysis - for the SATellite period
CLS	Collecte Localisation Satellites
CMIP5	Coupled Model Intercomparison Project Phase 5 model - promotes a standard set of model simulations
CNT-H	High resolution model run without assimilation
CNT-L	Low resolution model run without assimilation
CORA	Coriolis Ocean database ReAnalysis
CRG	ESA CCI Climate Research Group
CSIRO	Commonwealth Scientific and Industrial Research Organisation
CSR	Center for Space Research, Texas
CU	University of Colorado
DA	Data Assimilation
DJF	Boreal Winter
DOI	Digital Object Identifier
DTU	Danish Technical University
DUACS	Data Unification and Altimeter Combination System
ECMWF	European Center for Medium-range Weather Forcast
EBP	Equivalent Bottom Pressure
ECV	Essential Climate Variable
EFL	Effective Filter Length Scales
EM	Ensemble Mean
EN3	MET Office - quality controlled subsurface ocean temperature and salinity data set
ENSO	El Nino Southern Oscillation
EOF	Empirical Orthogonal Function
ESA	European Space Agency
FGAT	First Guess at Appropriate Time
FL	Filter Length Scale
GECCO	German Estimation of the Circulation and Climate of the Ocean
GFZ	German research institute on geodesy
GIA	Global Isostatic Adjustment
GLDAS	Global Land Data Assimilation
GM	Global Mean
GMSL	Global Mean Sea Level

GOCE	Gravity Field and Ocean Circulation Explorer
GOM	Global Ocean Mass
GRACE	Gravity Recovery and Climate Experiment
GSFC	NASA's Godard Space Flight Center
GX_SLX	Weighted RMS differences based skill score between 1) the GECCO2 model solution *GX* and 2) a sea level product *SLX*. "*X*" are used as wild-cards, they can be 0/1/1.1/2.0 to describe the skill score for e.g. *G0_SL1.1* or *G1.1_SL2.0*.
HADGEM	Hadley Centre Global Environment Model
HadSST2	Hadley Centre Sea Ice and Sea Surface Temperature data set
HPF9	High Pass Filter
IK	Ishii and Kimoto
IMBIE	Ice sheet Mass Balance Inter-comparison Exercise
IPRC	International Pacific Research Center
IPSL	Institute Pierre Simon Laplace Model, Paris
ISBA	Interaction Soil Biosphere Atmosphere
JAMSTEC	Japan Agency for Marine-Earth Science And Technology
JJA	Boreal Summer
JPL	Jet Propulsion Laboratory
KVS	Karina Von Schuckmann (update from Von Shuckmann and Le Traon, 2011)
LB	Lofoten Basin
LSA	NOAA's Laboratory for Satellite Altimetry
MAM	Boreal Spring
MDT	Mean Dynamic Topography
MERRA	NASA's Modern-Era Retrospective Analysis for Research and Applications
MSL	Mean Sea Level
MSLA	Map of Sea Level Anomalies
MSS	Mean Sea Surface
NAC	North Atlantic Current
NANSHY	Nansen Hydrographic data base
NCEP	National Centers for Environmental Prediction
NEMO	Nucleus for European Modelling of the Ocean
NEMOVAR	Variational data assimilation system for the NEMO ocean model (Mogensen et al. 2012).
NERSC	Nansen Environmental and Remote Sensing Center
NOAA	National Oceanic and Atmospheric Administration
NoAlti	Different model runs of the NEMOVAR model - NoALti assimilates T and S but no altimeter data
NorCPM	Norwegian Climate Prediction Model
NorESM	Norwegian Earth System Model
NS	North / South

OBE	OBservation Errors
OGCM	Ocean Global Circulation Model
ORAS	Ocean Reanalyses
ORAS-LW	ORAS5 Equivalent Low Resolution Reanalysis
ORCA025	DRAKKAR 1/4 degree ORCA configurations (see Barnier et al. 2006) for NEMO model
ORCA1	ORCA1 is the generic name that refers to the tripolar grids used by the NEMO model in approximately 1 degree resolution in the Extratropics.
OSI-SAF	Ocean Sea Ice – Eumetsat Satellite Application Facilities
OSTIA	Operational Sea Surface Temperature and Sea Ice Analysis
OSTM	Ocean Surface Topography Mission
PC	Principal Component
PSD	Power Spectral Density
RMS	Root Mean Square
SIC	Sea Ice Concentration
SCRIPPS	Scripps Oceanographic Institution, CA, USA
SL	Sea Level
SLA	Sea Level Anomaly
SLTAC	Sea Level Thematic Assembly Center
SLR	Sea Level Rise
SON	Boreal Autumn
SPG	SubPolar Gyre
SSH	Sea Surface Height
SSHA	Sea Surface Height Anomaly
SST	Sea Surface Temperature
STD	Standard Deviation
TOPAZ	(Towards) an Operational Prediction system for the North Atlantic European coastal Zones
TP	TOPEX-Poseidon
TRIP	Total Runoff Intregrating Pathways
TIW	Tropical Instability Waves
WGHM	Water Gap Hydrological Model
WP	Work Package

List of Contents

1. Assessment by the Climate Research Group

Today, many users are interested in altimetric SSH measurements. However, more quantitative comparisons need to be performed. This requires easy to use data formats as well as data uncertainty measures. In the future we can also anticipate that satellite data will be assimilated into climate models. At that point coupled models are used to test the data.

In the ocean modelling community satellite data, especially SSH fields, are now being assimilated on a regular basis. The need of assimilating SSH fields originates from their dynamical relevance in constraining the ocean's flow field. This is in strong contrast to other satellite observations of the ocean, measuring sea surface temperature (SST) and ocean color.

As indicated above, different levels of complexity and maturity exist in the ocean and climate modelling, which are accounted for in those WPs: Ocean models assimilate all available ECVs with measurable success. Respective results are available from many models. Results are inter-compared and are used for assessing processes involved in SSH changes.

Because of those differences, different model strategies are involved in WP 5100 as outlined in Table 1 ocean assimilation (WP5110 and WP5120) and coupled modelling (WP5130). Together, these three sub-work packages provide different and mutually complementary approaches, which in total provide a very strong package to test the new ECVs, but also to prepare a data stream suitable to the entire modelling community.

The different approaches include:

SYSTEM	EXPERIMENT	ASSIMILATION OF	COMPARISON TO
GECCO	GECCO 2	Almost all climate variables including SL (*SL0* and *SL1.1*, along track)	*SL0* *SL1* *SL1.1* *SL2.0* (gridded and along-track)
NEMOVAR	ASSIM (1x1)	T, S, *SL0* (along track)	*SL1* (gridded)
	NoAlti (1x1)	T, S	*SL1* *SL0* (hr/lr) (gridded)
	CNT-L (1x1)	-	
	CNT-H (1/4x1/4)	-	
NorESM	CMIP5	-	*SL0* *SL1* other ESA ECV in situ data
HADGEM	CMIP5	-	
IPSL	CMIP5	-	

Table 1: Assimilation and inter-comparison experiments conducted in the different systems from WP5100. The previous and the current versions of the SL_cci ECV are called *SL1*, *SL1.1* and *SL2.0* respectively and the AVISO data-set is called SL0.

(1) Comparison studies with ocean and/or coupled models to compare trends, multi annual, decadal variability, etc. A question that has been addressed is:

Are the structures observed by sea level products consistent with models outputs?

(2) Assimilation studies with ocean and/or coupled models, through which the new ECV is being used as a constraint jointly with all other available ECVs over the ocean and with in situ data. Questions to address here include:

How to use or improve the use of ECV products?

What is the impact of the improved data-set in comparison to the AVISO data-set?

A synthesis of the experiments that have been conducted in WP5100 is given in Table 1.

1.1. WP5110: UoH Sea level ECV assessment via global ocean model assimilation

1.1.1. Introduction

Testing the quality of the SL_ECVs may imply different aspects or approaches including direct scientific analyses and the interpretation of information from one data-set in conjunction with the information available from others. As an example, steric sea level changes can be studied in conjunction with temperature measurements, as steric sea level is the part of sea level changes that is due to thermal expansion and salinity variations in the ocean.

On the other hand, it is not always possible to test data-sets against independent data-sets. Therefore, we usually have to search for independent information. This is generally available in the form of ocean dynamics, as it is embedded in our climate models. Because of this, ocean models and ocean dynamics were used in the past to test and to interpret altimetric data.

Testing the consistency of observations with ocean dynamics and with a-prior information on uncertainties relies very much on mathematically consistent data assimilation approaches, e.g., as embedded in smoother or adjoint models. A dynamically consistent ocean state estimation adjusts uncertain model parameters to bring the model into consistency with ocean observations.

For the WP5110, the recent and higher resolution GECCO2 ocean synthesis framework is used to assess the quality of satellite altimeter data from the ESA climate change initiative (cci) project aimed at improving SSH data. The improved SSH fields (*SL1* and *SL1.1*, Cazenave et al., 2014, as well as *SL2.0*) represent the ECV of sea level (SL) computed in the framework of the ESA SL_cci (Ablain et al., 2015). As we will show below, the GECCO procedure does identify a significant level of improvement in the new *SL1.1* and *SL2.0* products when compared to the previous versions *SL1* and the original product *SL0* (from AVISO) in terms of global and regional dynamics, trends, seasonal cycle etc.

During Phase 1, the focus has been on the comparison of existing GECCO2 solutions (Köhl and Stammer, 2008a, b), referred to as *G0*, with the data-sets *SL0* and *SL1*, and the respective analysis of residuals in both cases. The metric that has been used here is that smaller residuals are interpreted as a better data-set. Strictly speaking this is not the case everywhere but has been a good guiding principle. Smaller residuals were expected for the SL_cci products. Residuals were investigated in this respect globally and regionally, not only as normalized RMS differences, but also in terms of seasonal cycle, SSH trends, among other dynamical parameters.

During Phase 2, the focus has been moved to the updated SL_cci product, *SL1.1*. Only to the end of the project the latest SL_cci product *SL2.0* has been available. To start, the existing *G0* solution has been compared to both data-sets *SL0* and *SL1.1* with an analysis of residuals, demonstrating an improvement of *SL1.1* over *SL0*. Further, the *SL1.1* product has been assimilated into the GECCO2 model producing a new GECCO2 solution (*G1.1*). As before, the new *G1.1* solution has then been compared to both data-sets *SL0* and *SL1.1*, again with an analysis of the residuals that emerge in both cases. In a third assimilation run the additional information content in the new ESA SST_cci data sets (Merchant et al., 2014) have been tested by including them also into the GECCO2 state estimation. This third GECCO2 solution, *G1.1sst*, has again been compared to both SL data sets, *SL0* and *SL1.1*. The results are summarized in Scharffenberg et. al (2017).

Towards the end of Phase 2, the latest update of the SL_cci product, *SL2.0*, had been released. Version *SL2.0* has been compared to both GECCO2 model solutions *G0* and *G1.1* with the same analysis of residuals between the model results and the SL product itself. However, due to a change of the reference positions as well as a change in filter length scale, the comparisons between *SL2.0* and the previous versions *SL0*, *SL1* and *SL1.1,* do not provide directly comparable results and are not straight forward.

1.1.2. Used Data-sets

The output of the GECCO2 assimilation approach (Köhl and Stammer, 2008a, b), *G0*, was used to compare *SL0* to versions *SL1*, *SL1.1* and *SL2.0*, for the time period 01/1992 until 12/2010 (see Table 2).

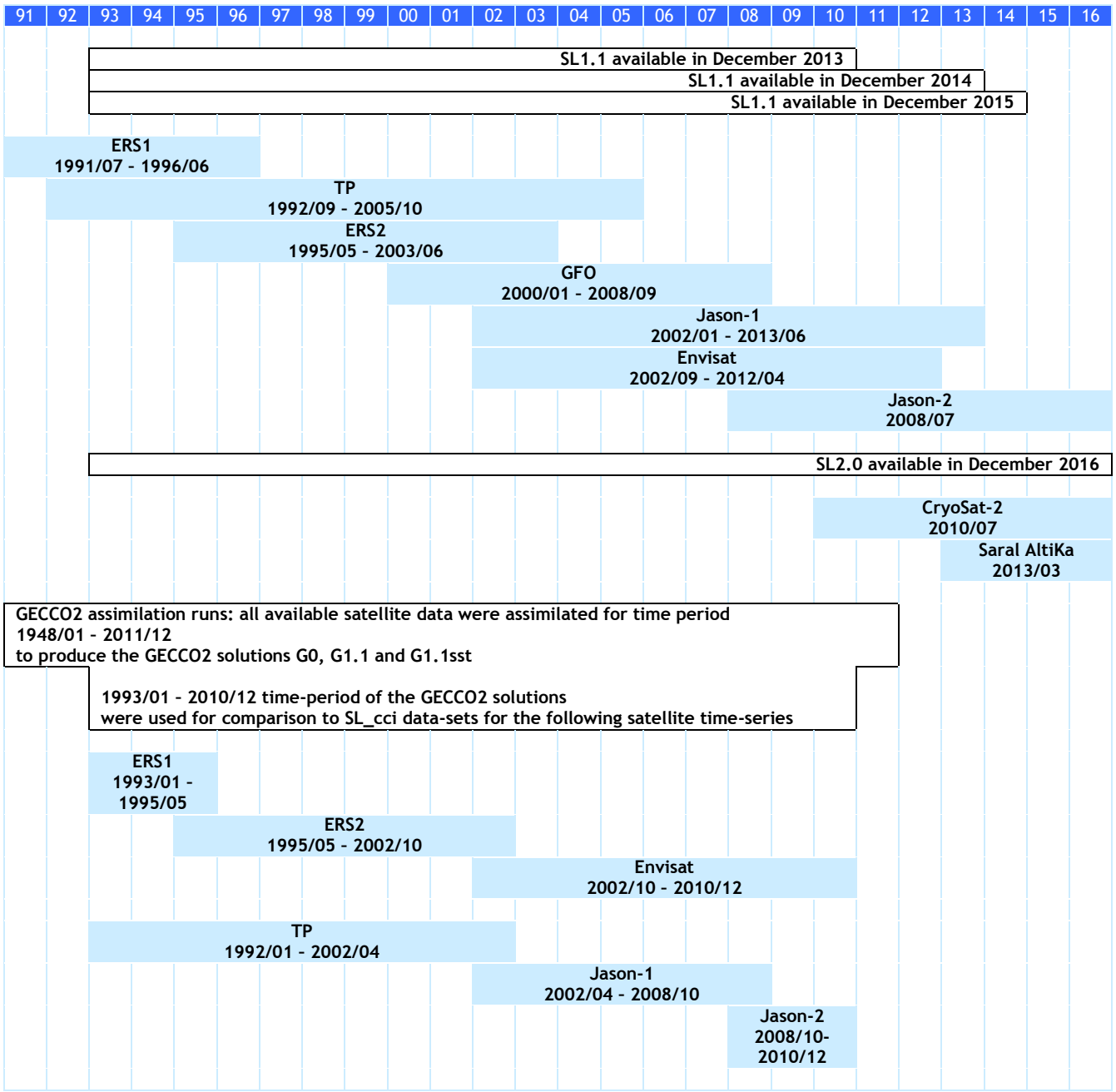

Table 2: Time-periods of: the available satellites, the SL_cci products, the GECCO2 assimilation runs, the GECCO2 solutions used for the comparison with the SL_cci data-sets, as well as the used SL_cci TP- and ERS-time-series.

The *G1.1* and *G1.1sst* solutions were used to compare *SL0* to versions *SL1.1* and *SL2.0*. The comparisons have been done separately for the ESA satellite series (ERS-1, ERS-2 and ENVISAT) and

for the TOPEX/POSEIDON satellite series (TOPEX/POSEIDON (T/P) Jason-1 and Jason-2). The three satellite products (*SL1*, *SL1.1*, Cazenave et al., 2014, and *SL2.0*) that have been provided within the SL_cci project consist of Sea Surface Height (SSH) anomalies, which have been reprocessed using new updated geophysical standards and multi mission cross calibration. Two versions of this product were provided to the scientific community, respectively:

(1) A set of SSHA grids combining all altimetric satellite measurements, with a regular spatial resolution of 0.25°x 0.25°, with monthly temporal resolution from 1993 to 2013, and

(2) A set of along-track SSH anomalies for each altimetric satellite, from 1992/93 to 2013.

For versions *SL1.0* and *SL1*.1, the along-track SSH level 3 products were previously filtered by the SL_cci project with a filter length scale that varied by latitude and were interpolated onto latitudinally varying reference positions prior to delivery. The applied filter length scales are 250 km (0° to 10°), 200 km (10° to 20°), 150 km (20° to 30°), 100 km (30° to 40°) and 65 km (40° to 90°). The original along-track resolution of about 6.2 km has been interpolated onto 18.6 km (90° to 30°), 24.9 km (30° to 20°), 31.8 km (20°), 37.4 km (20° to 10°) and 43.7 km (10° to the equator).

For version *SL2*.0, the along-track SSH level 3 product has been kept at its exact measurement positions every ~5.9 (~6.6) km. Further, the along-track filtering and subsampling has been kept less restrictive with a 10 point Lanczos filter and a 1 out of 2 point sub-sampling leading to measurements every ~11.7 (13.1) km. Due to updates in the level 2 (L2) altimeter corrections, the *SL2.0* data set now has an improved data coverage in the Arctic as well as in the Antarctic region, as can be seen e.g. in the Weddell sea in Figure 4, Figure 5, Figure 7, Figure 11 and Figure 12. In order to allow for a comparison to the previous data sets, the *SL2*.0 had to be interpolated onto the same AT reference positions as the previous *SL0*, *SL1* and *SL1.1* data sets. Due to the smaller SL_cci filter length scale of 10 points, the comparisons to the GECCO2 model output are expected to be different and less good as for *SL1.1*, equatorward 40°, as the model is not able to resolve the small scale processes in the *SL2.0* data.

The length scales are summarized in Table 3. The effective filter length scales (EFL) are calculated as: $EFL = (AT * F) + (FL - AT)$, with AT being the along-track resolution, F the filter as number of filtered points (f7, f9, f5 or f11), and FL the filter length scale that has been applied for the calculation of the along-track measurements. The filter f5 of *SL2.0* (7th column) is chosen to match the filter length scale of *SL0*, *SL1* and *SL1.1* (2nd column), and the filter f11 of *SL2.0* (8th column) is chosen to match the effective filter length scale of filter f9 of *SL0*, *SL1* and *SL1.1* (6th column). Filter f9 is the filter that is closest to the GECCO2 model cut off, discussed in section 1.1.7 and shown in Figure 6.

Latitudinal range	Filter length scale [km] SL_cci		SL_cci AT resolution [km] TP (ERS)	Effective filter length scale [km] TP (ERS)			
	SL0 SL1 SL1.1	SL2.0		SL0 SL1 SL1.1		SL2.0	
				f7	f9	f5	f11
90° - 40°	65	10 points 59 (66)	18.6 (19.7)	176.6 (183.2)	213.8 (222.6)	133.4 (144.8)	245 (263)
40° - 30°	100						
30° - 20°	150		24.9 (26.4)	249.4 (258.4)	299.2 (311.2)	158.6 (171.6)	308 (330)
20°			31.2 (33.0)	337.2 (348.0)	399.6 (414.0)	183.8 (198.0)	371 (396)
20° - 10°	200		37.4 (39.7)	424.4 (438.2)	499.2 (517.6)	208.6 (224.8)	433 (463)
10° - 0°	250		43.7 (46.4)	512.2 (528.4)	599.6 (621.2)	233.8 (251.6)	496 (530)

Table 3: SSH along-track filter length scales (FL), interpolated along-track (AT) resolutions, as well as effective filter length scales (EFL) for TP and ERS.

1.1.3. The GECCO2 synthesis

Obtaining dynamically self-consistent estimates of the ocean circulation requires the use of mathematically consistent "smoother" data assimilation approaches as realized by adjoint methods. Any smoother assimilation approach adjusts uncertain model parameters to bring the model into consistency with ocean observations; see Stammer et al. (2016) for details on the various methods used during assimilation efforts. In the case of the GECCO2 estimate (Köhl, 2015), those are the initial temperature and salinity conditions and the atmospheric state variables from which surface forcing fields are derived via bulk formulae. In this way, the ocean state estimation ultimately leads to new estimates of the surface forcing fields that are required to simulate the observed ocean in a best possible way (given the model resolution and the model physics). Stammer et al. (2004) have shown that outside of western boundary current regions the resulting surface flux fields show improved skill, and that large biases present in the NCEP fields seemed to be remedied (see also Menemenlis et al. (2005), who came to a similar conclusion).

This present study is based on a previous GECCO2 solution covering the period from 1948 to 2011 that had been optimized over 23 iterations. See Köhl (2015) for a description of the GECCO2 ocean state estimate and the data sets used as constraints. Starting from this already optimized state, 3 additional assimilation runs were performed as part of this study, all starting from iteration 23, carrying out 5 additional iterations. The only difference between these 3 assimilation runs (*G0*, *G1.1*, and *G1.1sst*) are the different SSH and SST data sets used as constraints. As before, the GECCO2 model continued to assimilate in situ temperature and salinity data, SST data and a mean dynamic topography. For each experiment 5 iterations were added to the previous solution to have a consistent set of solutions.

The first assimilation run is a continuation of the original GECCO2 synthesis which assimilates the AVISO SSH fields *SL0*. In contrast the second assimilation run uses the updated SL product *SL1.1* as SSH constraint. The small number of just 5 additional iterations is justified by the small differences between the different SL products *SL0* and *SL1.1* which do not warrant a complete new synthesis. Over the course of the five additional iterations the cost function contribution (sum of weighted squared differences to the data) representing the altimeter data misfit reduced typically by 20 %; however, during the last iterations the initial steep improvement flattened out suggesting that the additional optimization found a new minimum. The global mean sea level (GMSL) of the GECCO2 model is zero at each time step, thus GECCO2 does not have a GMSL rise. Therefore, before assimilation, the GMSL computed from mapped altimeter data was subtracted from the along track data (*SL0* and *SL1.1*) at each time. A third assimilation run assimilated *SL1.1*, and additionally an updated sea surface temperature product from the ESA SST_cci. In the following, the three resulting GECCO2 outputs will be referred to as *G0*, *G1.1* and *G1.1sst* respectively. For future GECCO assimilation runs we would prefer using *SL2.0* and higher, depending on its timely availability.

1.1.4. Methodology

It is important to note that the GECCO2 synthesis adapts to the assimilated *SL0* and *SL1.1* data products, respectively, and also to additional data sources, such that a cost function that measures the weighted quadratic differences between model and data, is being minimized. Due to the assimilation of additional data, the assimilation procedure is able to compensate for observational errors in one data source. As was shown before, GECCO2 rejects components in the assimilated altimeter data, such, that are dynamically incompatible with the model solution; by comparing the SL_ECVs against the synthesis, errors in the data can then be revealed. These capabilities have been demonstrated for the mean dynamic topography (Stammer et al., 2007). Although the model suffers from large biases and its resulting sea level fields cannot be assumed free of error or even of smaller error than the assimilated data, the improvement of the data shows up as a reduction in model data

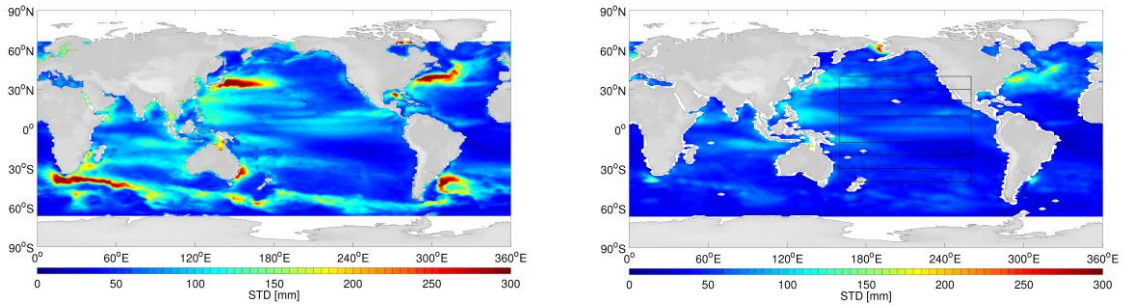

Figure 1: STD on the TP-tracks for *SL1.1* (left) and for GECCO2 (*G1.1*, right). The STD are from the along-track analysis.

residuals since the improved data will be in better agreement with additionally assimilated data. This is because the error of different data sources can be assumed to be uncorrelated.

To illustrate the variability present in the SL products, as compared to the GECCO2 synthesis, Figure 1 compares the standard deviation (STD) of the SL product *SL1.1* with that obtained from the GECCO2 synthesis product *G1.1*. The GECCO2 synthesis *G1.1* can reproduce the general large scale variability seen in the SL-data (*SL1.1*), however, as the model is in zonal direction set up on a 1° grid and in meridional direction on a 1/3° grid (for details see Köhl, 2015), it is not able to resolve eddies and lacks of variability in regions of high mesoscale activity such as the boundary currents or along the Antarctic Circumpolar Current (ACC) in the Southern Ocean.

To assess the improvement of *SL1*, *SL1.1* and *SL2.0*, the daily output fields of SL from all three GECCO2 solutions (*G0*, *G1.1* and *G1.1sst*) are compared to the four along track SL products *SL0*, *SL1*, *SL1.1* and *SL2.0* itself, using two different approaches:

(1) The first approach uses the GECCO2 model grid (M) as basis for the analysis of the root mean squared (RMS) differences. Here, the along-track data-sets (SL), have been interpolated onto the model grid, whereas

(2) The second approach, uses the full resolution of the SL data-sets and performs the same analysis for each along-track satellite position (AT) individually. The daily model output was interpolated onto the satellite tracks that matched the respective days for the respective along-track positions.

As noted above, the along track data sets (*SL0*, *SL1*, *SL1.1* and *SL2.0*) have been interpolated onto reference positions along the satellite tracks. The daily GECCO2 synthesis results (*G0*, *G1.1* and *G1.1sst*) were interpolated onto the satellite tracks that matched the respective days for the respective along-track positions. For display purpose only, the data (*SL0*, *SL1*, *SL1.1* and *SL2.0*) and the synthesis results (*G0*, *G1.1*, *G1*sst) have been gridded on a 1°x 1° grid for the ERS-time series and on a 2°x 1° grid for the TP-time series. 190 and 664 repeat cycle were used from the ERS- and from the TP-time series respectively. A comparison between the analysis at model and along-track resolution is given in Table 4.

The first step was to compare the *G0* solution to *SL0* and to the updated SL products *SL1* and *SL1.1*. In the second step, the updated SL product *SL1.1* has been assimilated into the GECCO2 model, producing the *G1.1* solution as well as the *G1.1*sst solution, that additionally assimilated the new SST from the ESA SST_cci project. Both GECCO2 solutions (*G1.1* and *G1.1sst*) have been compared to the SL products *SL0* and *SL1.1*, as respective analysis of the residuals that emerge in all cases. Further, the *G1.1* solution has also been compared to *SL2.0*.

The assessment of data products has been done separately for the ERS- and the T/P-satellite data sets. In each case residuals were investigated globally and regionally, as normalized RMS differences. Smaller residuals were expected for the updated SL products *SL1*, *SL1.1* and *SL2.0*, but strictly speaking this is not the case everywhere. The normalized RMS differences are calculated as a measure to determine the difference of the SL products *SL0*, *SL1*, *SL1.1* and *SL2.0* compared to all three GECCO2 solutions. The normalized RMS difference based skill score have been calculated as:

$$G0\_SL0 = \sigma_{(G0\,-\,SL0)} \,/\, \mathrm{sqrt}(\sigma^2_{G0} + \sigma^2_{SL0})$$

$$G0\_SL1 = \sigma_{(G0\,-\,SL1)} \,/\, \mathrm{sqrt}(\sigma^2_{G0} + \sigma^2_{SL0})$$

$$G0\_SL1.1 = \sigma_{(G0 - SL1.1)} / \mathrm{sqrt}(\sigma^2_{G0} + \sigma^2_{SL0})$$

$$G0\_SL2.0 = \sigma_{(G0 - SL2.0)} / \mathrm{sqrt}(\sigma^2_{G0} + \sigma^2_{SL0})$$

$$G1.1\_SL0 = \sigma_{(G1.1 - SL0)} / \mathrm{sqrt}(\sigma^2_{G1.1} + \sigma^2_{SL0})$$

$$G1.1\_SL1.1 = \sigma_{(G1.1 - SL1.1)} / \mathrm{sqrt}(\sigma^2_{G1.1} + \sigma^2_{SL0})$$

$$G1.1\_SL2.0 = \sigma_{(G1.1 - SL2.0)} / \mathrm{sqrt}(\sigma^2_{G1.1} + \sigma^2_{SL0})$$

$$G1.1sst\_SL0 = \sigma_{(G1.1sst - SL0)} / \mathrm{sqrt}(\sigma^2_{G1.1sst} + \sigma^2_{SL0})$$

$$G1.1sst\_SL1.1 = \sigma_{(G1.1sst - SL1.1)} / \mathrm{sqrt}(\sigma^2_{G1.1sst} + \sigma^2_{SL0})$$

with **σ** being the STD of the time series and GX_SLX the normalized RMS residuals. Note that the notation RMS differences of anomalies is trivially the same as the STD of anomalies, while referenced to the same averaging period. Again, *G0*, *G1.1* and *G1.1sst* denote the GECCO2 model runs that assimilated *SL0*, *SL1.1* and SST_cci solutions, respectively. Further, *SL0*, *SL1*, *SL1.1* and *SL2.0* SL-data-sets themselves, have been used for the comparison, respectively. Smaller residuals indicate an improvement of the *SL1.1* and *SL2.0* compared to *SL0*. The skill score is designed such that zero indicates perfect skill while a value of one is yield by two white noise time series and consequently corresponds to no skill Table 4 lists the possible comparisons.

Of the possible normalized RMS differences, *G0_SL0* is shown exemplarily in Figure 2, illustrating that the normalized RMS differences varies regionally. In the tropical regions GECCO2 and the SL product are very close together (blue) indicating a very good representation of the GECCO2 model solution of the assimilated SL data, whereas especially in energetic regions both clearly differ from each other (red). The analysis shows where the GECCO2 solution represents the assimilated SL product well. As it has been shown in Figure 1 for the STD, GECCO2 is missing energy in energetic regions. The model is not able to adjust for mesoscale features, mainly because they are not represented by the limited resolution of the model. However, the exercise of comparing Figure 1 and Figure 2 reveals that not all regions with large discrepancies are associated with high variability. In particular in the mid-latitude eastern Pacific lower skill can be found in quiet regions. The overall normalized RMS differences for both, the T/P and the ERS data sets are the same; however, as result of the unequal sampling dictated by the different satellite orbits, the small scale structures differ from each other. The following chapters discuss the disparities of the individual normalized RMS differences.

Assimilation run	GECCO2 + SL0 (*G0*)															
Compared product SL_ECV	*SL0*				*SL1*				*SL1.1*				*SL2.0*			
Time series	ERS		TP		ERS		TP		ERS		TP		ERS		TP	
Resolution	M	AT	M	AT	M	AT	M	AT	M	AT	M	AT		AT		AT

Assimilation run	GECCO2 + SL1.1 (*G1.1*)															
Compared product SL_ECV	*SL0*				*SL1*				*SL1.1*				*SL2.0*			
Time series	ERS		TP		ERS		TP		ERS		TP		ERS		TP	
Resolution	M	AT	M	AT	M	AT	M	AT	M	AT	M	AT		AT		AT

Assimilation run	GECCO2 + SL1.1 + SST (*G1.1*sst)

Assimilation run	GECCO2 + SL1.1 + SST (*G1.1*sst)									
Compared product SL_ECV	*SL0*					*SL1.1*				
Time series	ERS		TP			ERS		TP		
Resolution	M	AT	M	AT		M	AT	M	AT	

Table 4: Performed comparisons using the solutions from all three GECCO2 assimilation runs *G0*, *G1.1* and *G1.1*sst. Comparisons have been carried out for the four sea level products *SL0*, *SL1*, *SL1.1* and *SL2.0*, for both satellite series, ERS and TOPEX/POSEIDON, and on the model grid (M) as well as for the along-track positions (AT).

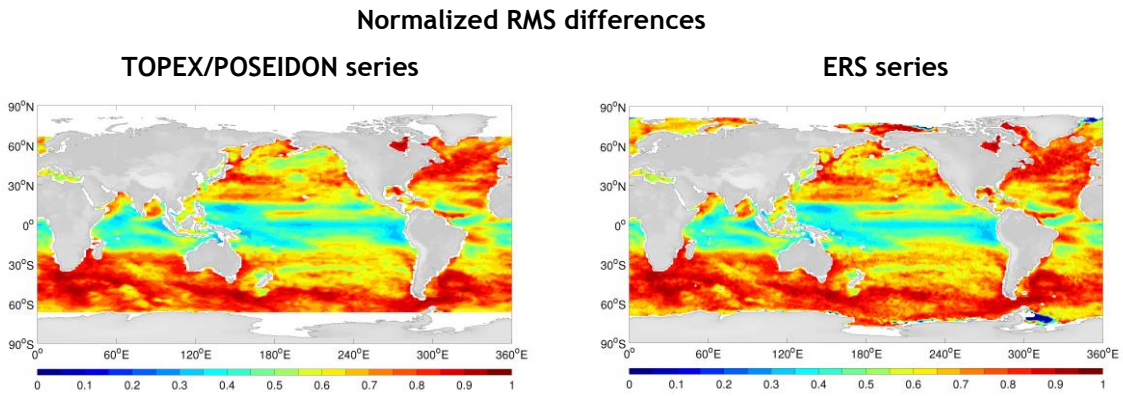

Figure 2: Normalized RMS differences *G0_SL0* between the GECCO2 model solution *G0* and the satellite-time-series of TOPEX/POSEIDON, Jason-1 and Jason-2 (left) and of ERS-1, ERS-2 and ENVISAT (right), for the analysis at AT resolution.

1.1.5. Pre-test at model resolution

In the first case, the model resolution has been taken as the basis for the comparison of both ECV products. The along-track data-sets of *SL0*, *SL1* and *SL1.1* have been interpolated onto the model grid and the analysis has been carried out at model resolution. Figure 3 shows the ratios of the normalized RMS differences in order to provide a measure of the improvement of *SL1* and *SL1.1*. The comparison (ratios) is shown for TP-series (left) and for ERS-series (right).

The panels show the ratio of *G0_SL0* / *G0_SL1* (1st row), *G0_SL0* / *G0_SL1.1* (2nd row), and *G1.1_SL0* / *G1.1_SL1.1* (3rd row), *G1.1sst_SL0* / *G1.1sst_SL1.1* (4th row), as percentages of improvement of *SL1* and *SL1.1* compared to *SL0*. In all panels red indicates an improvement whereas blue indicates degradation.

Ratio *G0_SL0* / *G0_SL1* (1st row) shows remarkable improvements in the north Atlantic, in the Indian Ocean through flow and in many other parts of the ocean.

Ratio *G0_SL0* / *G0_SL1.1* (2nd row) demonstrates the outstanding improvements from *SL1* to *SL1.1* in all tropical oceans. The regions in blue where the *SL1* and *SL1.1* show less skill compared to the *SL0* are the ones where the GECCO2 *G0* solution has adapted very well to the *SL0* and at the same time where the STD of the data-sets (Figure 1) are very small, indicating a small signal to noise ratio in these regions. Therefore, the model might have adapted to the not as good *SL0* data, and thus gives less skill in comparison to the improved *SL1* and *SL1.1* data-sets.

Ratio *G1.1_SL0* / *G1.1_SL1.1* (3rd row) indicates the improvements seen due to the assimilation process of the *SL1.1* data set, instead of *SL0* before. In the further improved regions, the model

physics have adapted closer to the assimilated *SL1.1* product, and therefore, are in closer agreement to the *SL1.1* data set itself.

The ratio *G1.1sst_SL0* / *G1.1sst_SL1.1* (4th row) indicates the improvements seen due to the assimilation process of the *SL1.1* and additionally, of the updated SST. The improvement from the assimilation run *G1.1* to *G1.1sst* is only marginal. Further improved regions can be seen e.g. for North Atlantic, the subtropical South Atlantic, the tropical Indian Ocean as well as for parts of the ACC.

From the analysis on the model grid, we found that the *SL1.1* product has been improved in many regions compared to *SL0*. As the analysis at the model grid showed promising results, this test encourages the assessment at along-track resolution. Therefore, in the following sections, we make use of the full resolution of the along-track product at the satellite tracks.

Ratios of normalized R**MS differences at model resolution**

TOPEX/POSEIDON series **ERS series**

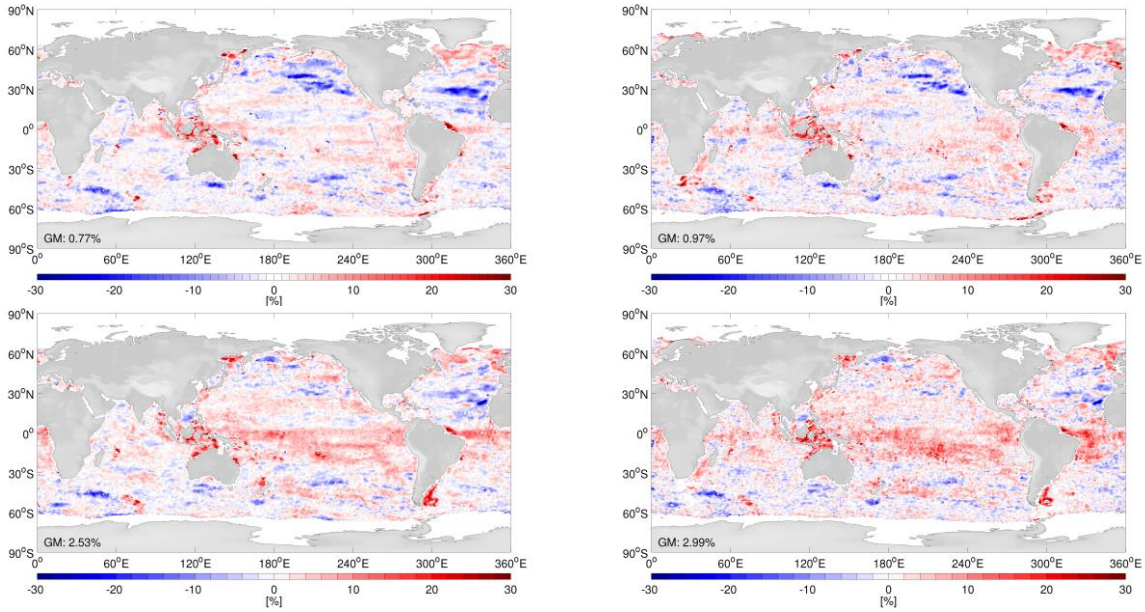

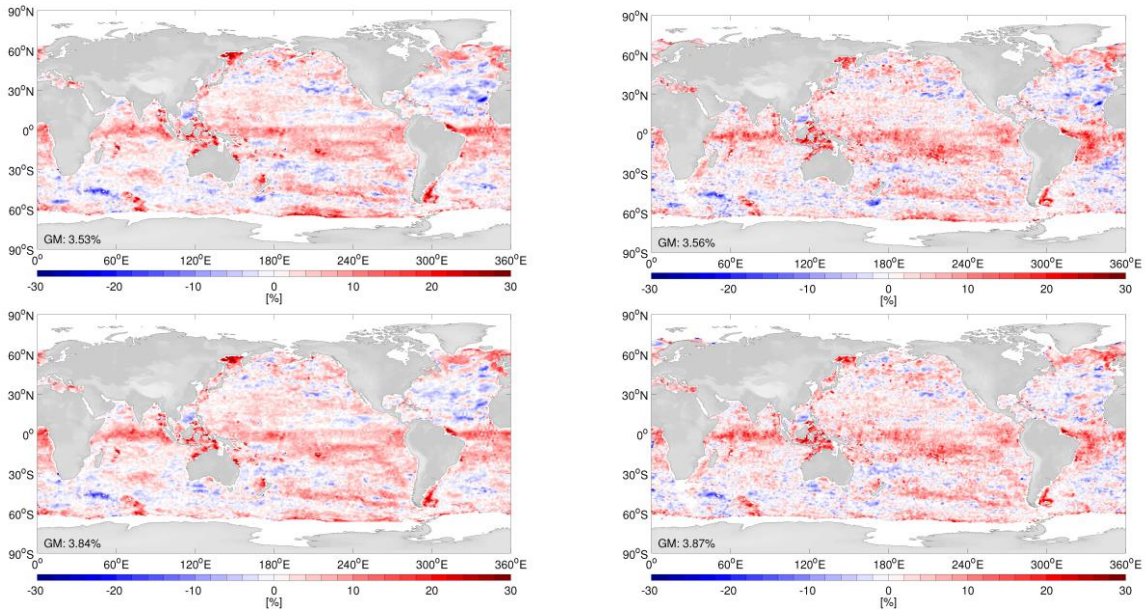

Figure 3: Ratio of normalized RMS differences, of *G0_SL0 / G0_SL1* (1st row), of *G0_SL0 / G0_SL1.1* (2nd row), of *G1.1_SL0 / G1.1_SL1.1* (3rd row), *and of G1.1sst_SL0 / G1.1sst_SL1.1* (4th row), between the GECCO2 synthesis and the satellite-time-series of TOPEX/POSEIDON, Jason-1 and Jason-2 (left) and of ERS-1, ERS-2 and ENVISAT (right). Compare to Figure 4, for the along-track analysis.

1.1.6. Sea level quality assessment

In the following we make use of the full resolution of the SL_ECV data-sets and compute any analysis for each satellite track-point individually. As we demonstrated at model resolution (Figure 3), that the updated version of the ESA SL_cci data set *SL1.1* (2nd row) has more skill as compared to SL1 (1st row), in the following only *SL1.1* will be discussed. For each of the six comparisons (see Table 3) we therefore generated four data-sets for each satellite series (TP and ERS) in the form, that each satellite track-point was a time series of sea level anomalies at that position. The six data-sets are *SL0*, *SL1.1/SL2.0* (the satellite data sets) and *G0* and *G1.1/G1.1sst* (the model data interpolated on the along-track points). The daily model output was interpolated onto the satellite tracks that matched the respective days for the respective along-track positions. We performed the same analysis of normalized RMS differences as for the assessment on the model grid.

In Figure 4 (1st row) the normalized RMS differences are now shown for the along-track products *G0_SL0 / G0_SL1.1*. The panels are comparable to Figure 3 (2nd row), at model resolution. A close agreement between both figures can be seen in the distribution of the improved regions, however, the magnitude of improvement is smaller at along-track resolution due to the different filter length scales of the model and the along-track products. This issue is addressed further in section 1.1.7.

Figure 4 (2nd and 3rd row) show the same normalized RMS differences *G0_SL0 / G0_SL2.0* but for SL version *SL2.0*. For the 3rd row an additional filter with a filter length scale of f5 is used, to be comparable to the filter length scales of *SL0*, *SL1* and *SL1.1* (see Table 3) equatorward of 40°. The ratios of *G0_SL0 / G0_SL1.1* and *G0_SL0 / G0_SL2.0* in Figure 4 are again given as percentages of improvement of *SL1.1* or *SL2.0* as compared to *SL0*, while red indicates an improvement, whereas blue indicates a degradation.

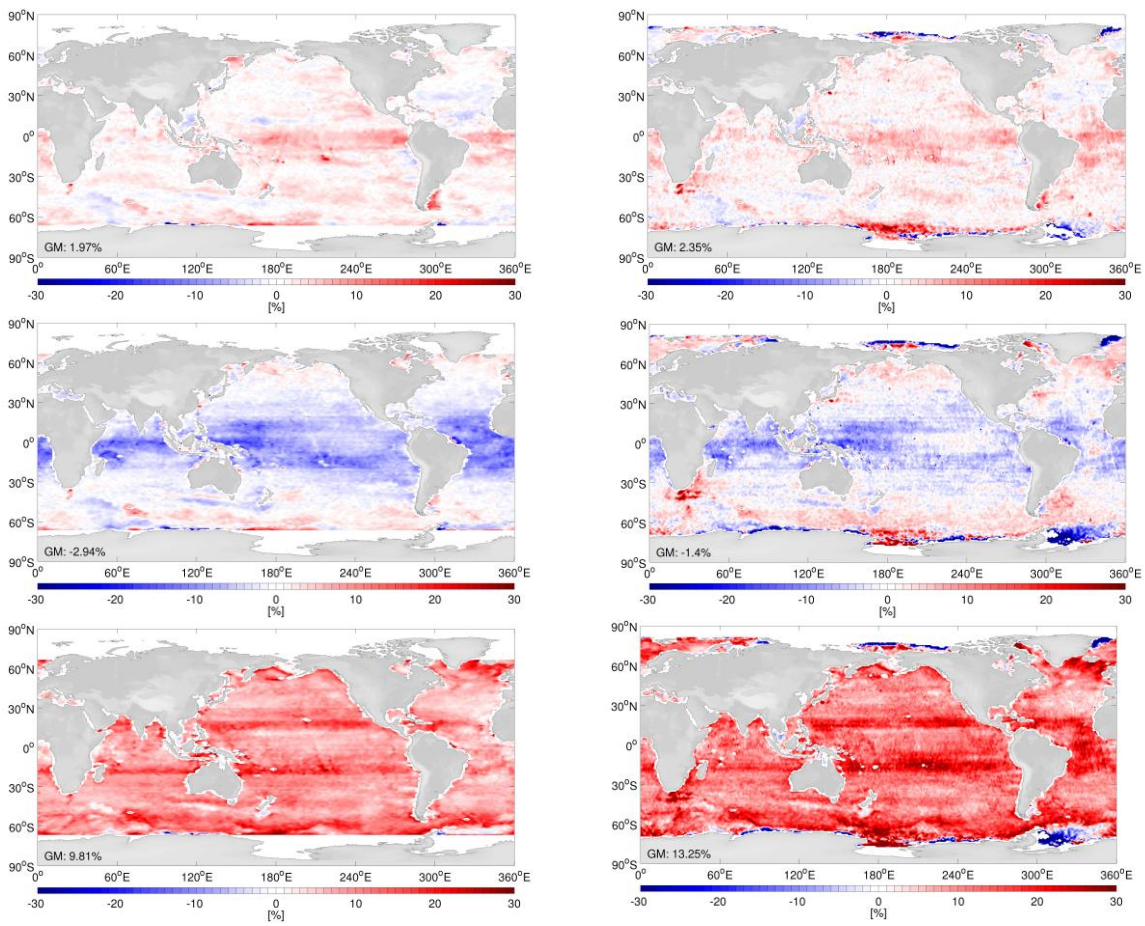

Figure 4: Ratio of normalized RMS differences, *G0_SL0 / G0_SL1.1* (1st row) and *G0_SL0 / G0_SL2.0* (2nd row), between the satellite-time-series of TOPEX/POSEIDON, Jason-1 and Jason-2 (left) and of ERS-1, ERS-2 and ENVISAT (right) and the GECCO2 model. Compare to 2nd row in Figure 3, for the analysis at model resolution. The 3rd row is the same ratio as in the 2nd row of *G0_SL0 / G0_SL2.0*, but with an additional filter (f5)

Ratio *G0_SL0 / G0_SL1.1* (Figure 4, 1st row) illustrates the improvements of *SL1.1* as compared to *SL0* of up to 30 %, as can be seen in all equatorial regions, on the Argentine shelf and in parts of the ACC. In most other parts of the ocean, improvements of up to 10 % are evident. A few regions also show a degradation of up to 10 %. In these regions *G0* shows little skill when compared to *SL1.1* despite the fact that the STD (Figure 1) in these regions are small, implying that the assumption of model serves as truth breaks down. Therefore, the model might have adapted to the uncorrected *SL0* and thus shows less skill when compared to the improved *SL1.1* data-set. Due to the different filter length scales of the SL products *SL1.1* and *SL2.0* (see Table 3 column 2), the ratios *G0_SL0 / G0_SL1.1* (1st row) and *G0_SL0 / G0_SL2.0* (2nd row) differ from each other equatorward of 40° at along-track resolution. To get comparable results, a filter (f5) has been applied for *G0_SL0 / G0_SL2.0* (3rd row). The filter (f5) is in the order of magnitude of the SL_cci filter length scales.

The global mean (GM) percentages of improvement between latitudes of 66°S and 66°N are in the order of 1.97/9.81 % (TP) and 2.35/13.25 % (ERS) for *SL1.1* and *SL2.0* respectively, and are given in the lower left corner of the panels in Figure 4. The improvements of *SL1.1* and *SL2.0* are remarkable despite the GECCO2 synthesis was adjusted to minimize the difference to the assimilated *SL0* data-set, and therefore, should be in best agreement with *SL0*. However, since many other climate data sets have been assimilated as well, the final state may reject the assimilated SSH data partly if it is inconsistent with other data. Therefore, the GECCO2 ocean synthesis may filter data errors even though large biases to the data remain in GECCO2 and the

GECCO2 model cannot be regarded as the best product with the smallest error. Since GECCO2 reveals a closer agreement to *SL1.1* and *SL2.0,* it is hypothesized that *SL1.1* and *SL2.0* are in better agreement with the other data than it was the case for *SL0*.

Overall, the improvements of the satellite time series of T/P and ERS are in close agreement with each other. However, since both satellite times series have been improved individually (Ablain et al., 2015), resulting improvements show different spatial characteristics; they also differ due to the different spatial resolutions and the different temporal sampling of 9.91 days for the TP-time series and of 35 days for the ERS-time series. Furthermore, the T/P tracks have a wider track spacing making it necessary to display the results at a 2°x 1° grid, whereas the ERS tracks have a smaller track spacing that allows for a display at a 1°x 1° grid. The differences between the ratios of RMS differences of *SL1.1* and *SL2.0* again result from the different filtering and along track resolution of both products.

1.1.7. Influence of assimilation of improved sea level

The significant improvement of *SL1, SL1.1 and SL2.0,* within the ESA SL_cci project (Ablain et al., 2015), as compared to *SL0* has been demonstrated in the previous section by comparing the SL data-sets to the GECCO2 ocean synthesis. This section will now investigate the impact on the GECCO2 model by assimilating the improved *SL1.1* data-set. For that purpose, *SL1.1* has been assimilated in the GECCO2 synthesis for iterations 23 to 28, replacing *SL0* In the assimilation process. The GECCO2 synthesis results from this assimilation run are therefore referred to as *G1.1*. As in the previous chapter, the ratios of both normalized RMS differences can be calculated for *G1.1* as *G1.1_SL0 / G1.1_SL1.1*. It is expected, that the assimilation of *SL1.1* in the GECCO2 synthesis leads to even smaller RMS differences for *G1.1_SL1.1,* because in *G1.1* the differences to *SL1.1* are minimized. Further, since the constraint of GECCO2 to be close to *SL0* does no longer exist it should deviate more from the SL data set *SL0*.

The 1st row of Figure 5 shows the ratios of *G1.1_SL0 / G1.1_SL1.1*, the 2nd row *G1.1sst_SL0 / G1.1sst_SL1.1*, and the 3rd row *G1.1_SL0 / G1.1_SL2.0*, as percentages of improvement for *SL1.1* and *SL2.0* as compared to *SL0*. Red indicates an improvement, whereas blue indicates a degradation compared to *SL0*.

The ratio *G1.1_SL0 / G1.1_SL1.1* (1st row) indicates the improvement of the GECCO2 model itself, due to the assimilation of the *SL1.1* product. The resulting GECCO2_V1.1 (*G1.1*) solution has adapted closer to the assimilated *SL1.1* data. The comparison indicates further improvements in the ACC and in many tropical regions as well as in the north Atlantic.

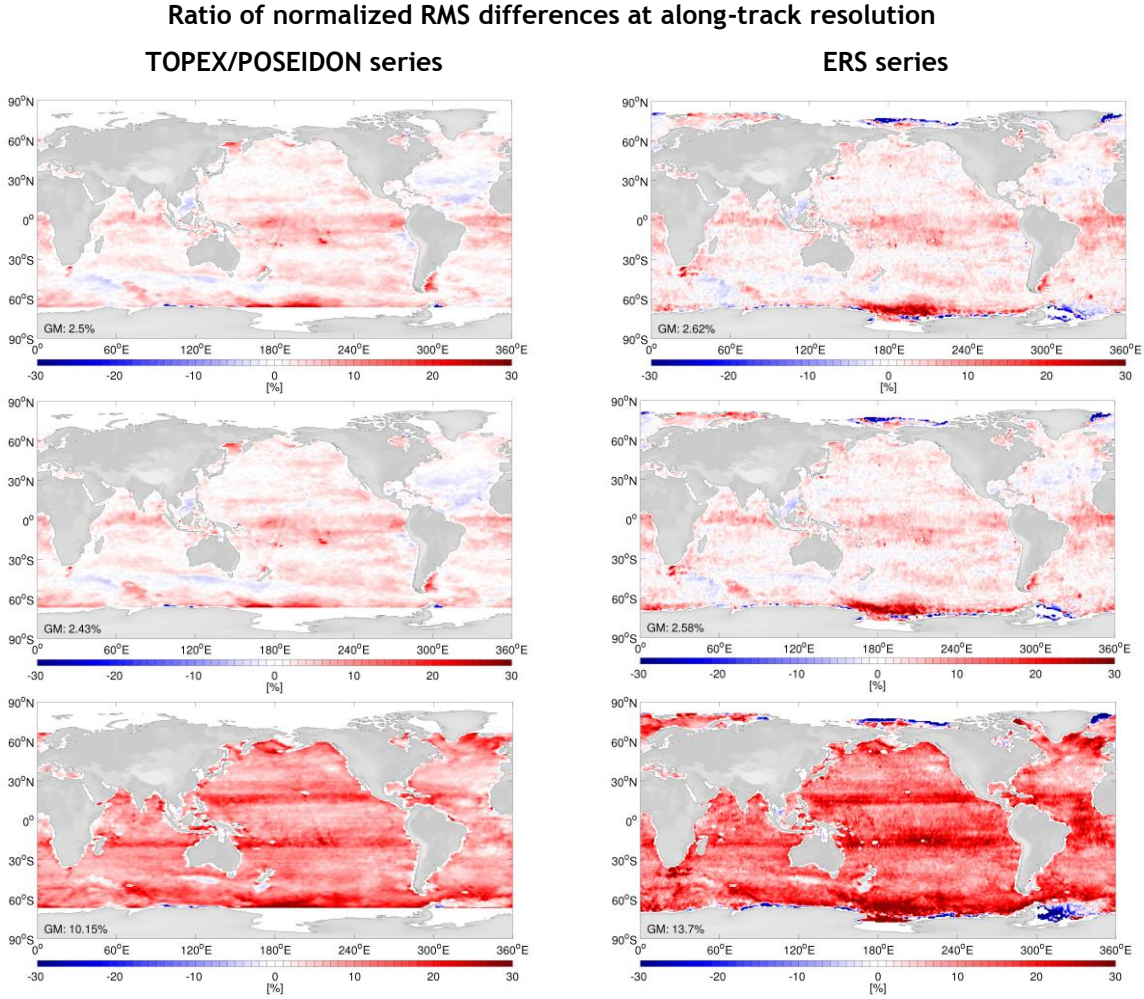

Figure 5: Ratio of normalized RMS differences of (1st row) *G1.1_SL0 / G1.1_SL1.1*, (2nd row) *G1.1sst_SL0 / G1.1sst_SL1.1*, and (3rd row) *G1.1_SL0 / G1.1_SL2.0* (f5), between the GECCO2 model and the satellite-time-series of TOPEX/POSEIDON, Jason-1 and Jason-2 (left) and of ERS-1, ERS-2 and ENVISAT (right). Compare to 3rd and 4th row in Figure 3, for the analysis at model resolution.

The ratio *G1.1sst_SL0 / G1.1sst_SL1.1* (2nd row) shows the improvement of the GECCO2 model itself due to the assimilation of the *SL1.1* product and the additional assimilation of the updated SST information from the ESA SST_cci. The resulting GECCO2 solution (*G1.1sst*) does not show an improvement or a degradation as compared to *G1.1* (1st row), and as it does not add new information, *G1.1sst* will not be included in the following discussions.

The results for *SL2.0* are given in the 3rd row as ratios *G1.1_SL0 / G1.1_SL2.0*. Here the GECCO2_SL1.1 solution (*G1.1*) is compared to the previous *SL0* and the latest *SL2.0* products. Even though, the resulting *G1.1* solution tried to adapt to the assimilated *SL1.1* data, it can be seen that the GECCO2 solution is in even closer agreement to the *SL2.0* data.

In order to give an overview and to allow for an inter-comparison of the various ratios of normalized RMS differences, global mean ratios of normalized RMS differences are presented in Table 5. The global mean ratios of normalized RMS differences from Table 5 are also indicated in the lower left corner of each plot.

RMS ratios	TP - data set					ERS - data set				
	M	SL0 SL1 SL1.1		SL2.0		M	SL0 SL1 SL1.1		SL2.0	
		AT 65 250 [km]	f9 213.8 599.6 [km]	f5 (AT) 133.4 233.8 [km]	f11 245.0 496.0 [km]		AT 65 250 [km]	f9 222.6 621.2 [km]	f5 (AT) 144.8 251.6 [km]	f11 263.0 530.0 [km]
$\frac{G0SL0}{G0SL1.1\ (SL2.0)}$	2.53	1.97	2.97	9.81	5.56	2.99	2.35	3.30	13.25	8.18
$\frac{G1.1SL0}{G1.1SL1.1\ (SL2.0)}$	3.53	2.50	3.77	10.5	5.88	3.56	2.62	3.76	13.7	8.6
$\frac{G1.1sstSL0}{G1.1sstSL1.1}$	3.84	2.43	3.59			3.87	2.58	3.67		
$\frac{G0SL0}{G1.1SL1.1\ (SL2.0)}$	3.80	3.25	4.75	10.97	6.88	4.07	3.32	4.74	14.48	9.6
$\frac{G0SL1.1}{G1.1SL1.1\ (SL2.0)}$	1.37	1.26	1.73	8.87	3.9	1.14	0.95	1.39	11.86	6.14

Table 5: Global mean ratios of normalized RMS differences for TP and ERS data sets as percentages of improvement, computed on the model grid (M), at the along-track (AT) points as well as at the AT points using a running filter of 9 (f9) and 11 (f11) points, with their respective smallest and longest along track resolution [km], for latitudes between 66°S and 66°N. The same comparison as for *SL1.1* has been carried out for *SL2.0* as e.g. *G0SL2.0* with a running filter of 5 (f5), corresponding to the AT resolution of *SL1.1*, and 11 (f11) points. The upper 3 rows illustrate the normalized RMS differences of the individual assimilation runs *G0*, *G1.1* and *G1.1sst*. The lower rows give the cross comparison of *G0* compared to *SL0* and *G1.1* as compared to *SL1.1* or *SL2.0*. Further, the bottom row illustrates the improvement of the GECCO2 model due to the improved assimilated ECV *SL1.1*.

In Figure 4, the analysis at the AT positions has been shown for *G0_SL0* / *G0_SL1.1*. As can be seen from Table 5, the global mean ratio of normalized RMS differences deviates between the analysis at AT resolution (1.97 % for TP and 2.35 % for ERS time series) and at model resolution (2.53 % for TP and 2.99 % for ERS time series). The disparity is expected, as the model was adjusted to the data on the model grid. The model resolution of about 1° allows for structures in the order of 400 km to be resolved, and bringing the model on the tracks by interpolation will lead to even smoother results. To identify the length scales the GECCO2 model is able to resolve and for which a meaningful inter-comparison between model and data is possible, zonal wavenumber spectra have been calculated in the Pacific, as this region is not affected by continental boundaries. The regions are marked in Figure 1 (right). A zonal wavenumber spectra gives the power spectral density (PSD) that is given at each spatial wavelength.

At each latitude and for each daily time step (1992-2012) a zonal wavenumber spectrum has been calculated in the longitude range of 160°E-260°E using a hamming window over the whole longitude range, while interpolating missing values linearly in between and zero-padding missing values at the ends. The spatial and temporal mean zonal wavenumber spectra are shown in Figure 6 combined for the northern and southern latitude ranges of 10°S-10°N, 10°-20°N/S, 20°-30°N/S and 30°-40°N/S.

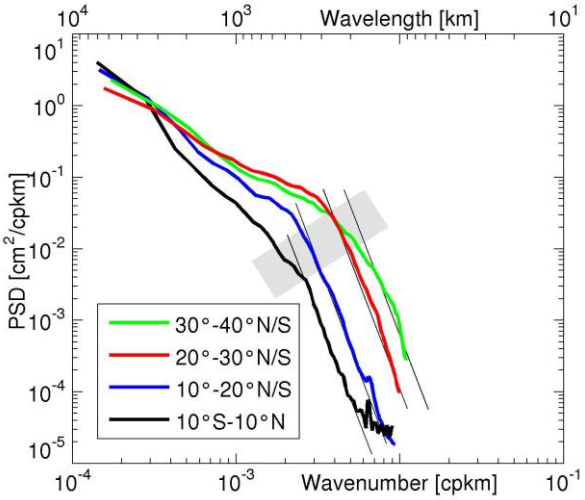

Figure 6: Meridional GECCO2 wavenumber spectra in the Pacific for the 20 year period, for the latitude bands 10°S-10°N, 10°-20°NS, 20°-30°NS and 30°-40°NS. The regions are marked in Figure 1 (right) and the northern and southern latitude bands are combined. The indicated slope is k^{-6}.

The model cut off length scale is mainly a function of the model resolution. However, the full grid resolution cannot be utilized because for reasons of numerical stability additional viscosity and diffusivity have to be prescribed, which ultimately determines the resolved scales (although implicit viscosity and diffusivity also play a role) by imposing an exponential decay on the spectrum. For the chosen harmonic viscosity acting on velocity, the exponent would be k^{-2} for the velocity spectrum and k^{-4} for the kinetic energy spectrum. Since sea level is associated to the near surface velocity via the geostrophic relation a slope of k^{-6} is expected for the SL. Slopes of k^{-6} are added to Figure 6 and are thus utilized to determine the cut off. Since a smooth transition into the k^{-6} slope regime exist the determination of the cut off bears some vagueness indicated by the grey box, which ultimately causes some arbitrariness in the determination of the scales.

From Figure 6 it appears that the GECCO2 model cut off is found to be latitudinal dependent and in the order of 400 km (5°), 360 km (15°), 250 km (25°) and 170 km (35°). As can be seen in Table 5, these model cut off length scales correspond to the AT running mean filter length scales for *SL1.1* that takes 9 AT-values (f9) into account. As *SL2.0* has a different initial filter length scale (see Table 3), the filter length scale that takes 11 AT values (f11) into account better represents the GECCO2 model cut off for *SL2.0*.

In order to generate the AT ratios of normalized RMS differences, that are comparable for AT and M resolution, the ratios of normalized RMS differences are shown in the following for the f9-filter (*SL1.1*) and f11-filter (*SL2.0*), as these filter length scales are closest to the cut off seen in the zonal wavenumber spectra of about 200 to 400 km, that the model is actually able to resolve. Therefore, the ratios of normalized RMS differences from Figure 4 are shown again in Figure 7, but this time low pass filtered with f9 for *SL1.1* (1st row) and f11 for *SL2.0* (2nd row), to illustrate the rate of improvement of the resolved features. For the TOPEX/POSEIDON time series the global mean improvement sums up to 2.97% for *SL1.1* and a of 5.56% for *SL2.0*. The GM improvement of the ERS time series is slightly larger: 3.3% for *SL1.1* and 8.18% for *SL2.0*.

The global mean ratios of normalized RMS differences for the different assimilation runs *G0*, *G1.1* and *G1.1sst*, as displayed in Table 5 (first 3 rows), clarify the improvement of *SL1.1*/*SL2.0* over *SL0*, as all the ratios are positive indicating the smaller RMS difference between each GECCO2 synthesis and *SL1.1* or *SL2.0* as compared to *SL0*. The global mean ratios of normalized RMS differences increase further, when assimilating the updated *SL1.1* in the GECCO2 synthesis (*G1.1_SL0* / *G1.1_SL1.1*). When additionally to *SL1.1*, assimilating an updated version of SST from the ESA SST_cci (Merchant et al., 2014), the global mean ratios of normalized RMS differences (*G1.1sst_SL0* / *G1.1sst_SL1.1*) are comparable to those of the assimilation run with the previous SST estimates

G1.1. The changed SST product therefore does not alter the GECCO2 synthesis significantly with respect to SL.

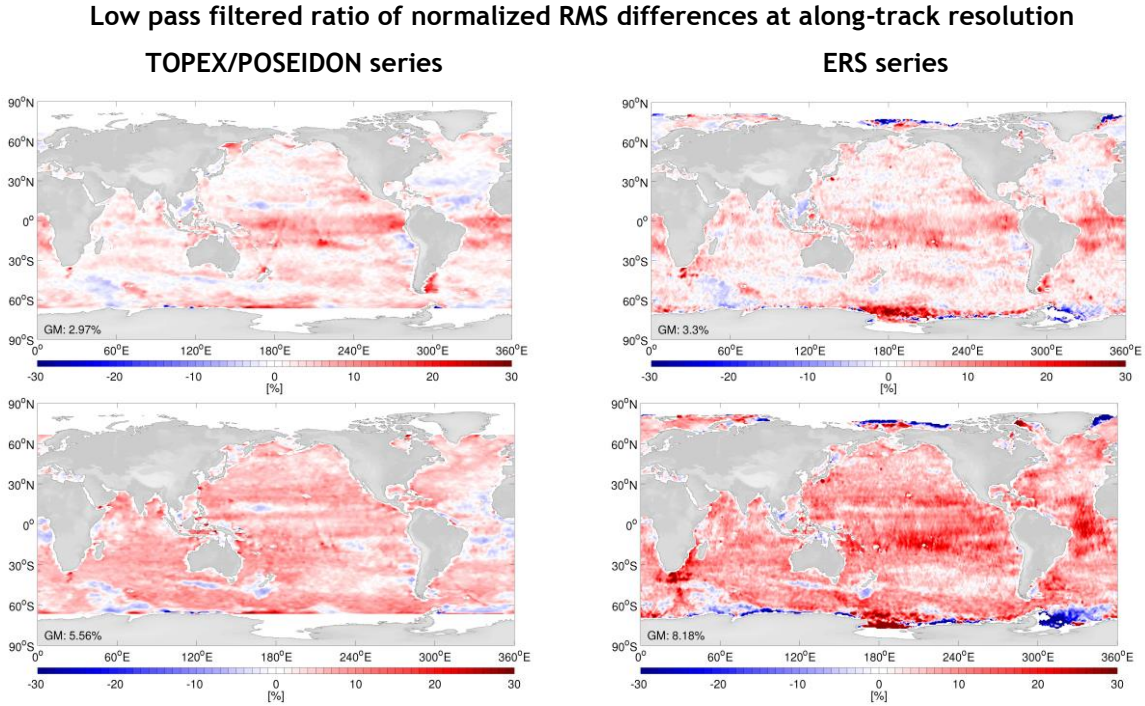

Figure 7: Low pass filtered ratio of normalized RMS differences *G0_SL0 / G0_SL1.1* with filter length scale f9 (1st row) and *G0_SL0 / G0_SL2.0* with filter length scale f11 (2nd row), between the GECCO2 model and the satellite-time-series of TOPEX/POSEIDON, Jason-1 and Jason-2 (left) and of ERS-1, ERS-2 and ENVISAT (right). Compare to Figure 3 (2nd row), for the analysis at model resolution.

The total improvement due to the updated satellite data *SL1.1* and its assimilation into the GECCO2 synthesis can be revealed by the ratio of the differences of *G0* and *SL0* by using only the previous data set *SL0*, and the differences of *G1.1* and *SL1.1* by using the updated SL data-set only. This ratio *G0_SL0 / G1.1_SL1.1*, as shown in Figure 8 (top), highlights the reduction of the normalized RMS differences in most regions of the world oceans and leads to an improvement of more than 30 % in many regions. As for the ratio *G0_SL0 / G0_SL1.1* (Figure 7), degradations of *SL1.1* exist in isolated regions, where the GECCO2 synthesis *G1.1* adapts less well to the assimilated *SL1.1* product than *G0* to the assimilated *SL0* product. The global mean improvement sums up to 4.75 % and 4.74 % for the TP- and ERS-data sets respectively. As *SL2.0* has not been assimilated into the GECCO2 model, a total improvement to either the *SL0* or the *SL1.1* data sets cannot be estimated. Nevertheless, the ratio *G0_SL0 / G1.1_SL2.0*, is shown in Figure 8 (bottom) to illustrate the achieved improvement due to the assimilation of *SL1.1* in the GECCO2 synthesis and the latest SL_cci data set *SL2.0*. Here the global mean improvement sums up to 6.88 % and 9.6 % for the TP- and ERS-data sets respectively.

While Figure 8 (top) gives the combined improvement due to the assimilation and the updated product (*SL1.1*), Figure 9 answers the question about the improvement of the GECCO2 synthesis, by changing the assimilated SL data-set only, from *SL0* (*G0*) to *SL1.1* (*G1.1*). Hence, the ratio *G0_SL1.1 / G1.1_SL1.1* compares the different assimilation runs *G0* and *G1.1,* while calculating the normalized RMS differences to the same updated *SL1.1* data-set. The GECCO2 synthesis takes most profit from the updated *SL1.1* data-set in the northern Indian Ocean, the ACC and the north Pacific. Degradations are evident in the north Atlantic, in the eastern north Pacific as well as in scattered regions around the globe. However, the overall global mean improvement of the GECCO2 synthesis of 1.73 % and 1.39 % as seen from the TP and ERS satellite time series indicates, that the model physics better accepted the assimilated *SL1.1* than the assimilated *SL0*, and therefore, adapted

closer to the *SL1.1* data-set. Although degradations seem surprising, given that the synthesis was constrained to the data, the problem is far too complex to expect a convergence to a minimum within only a few iterations. Not all changes can thus be expected to causally relate to the change of data.

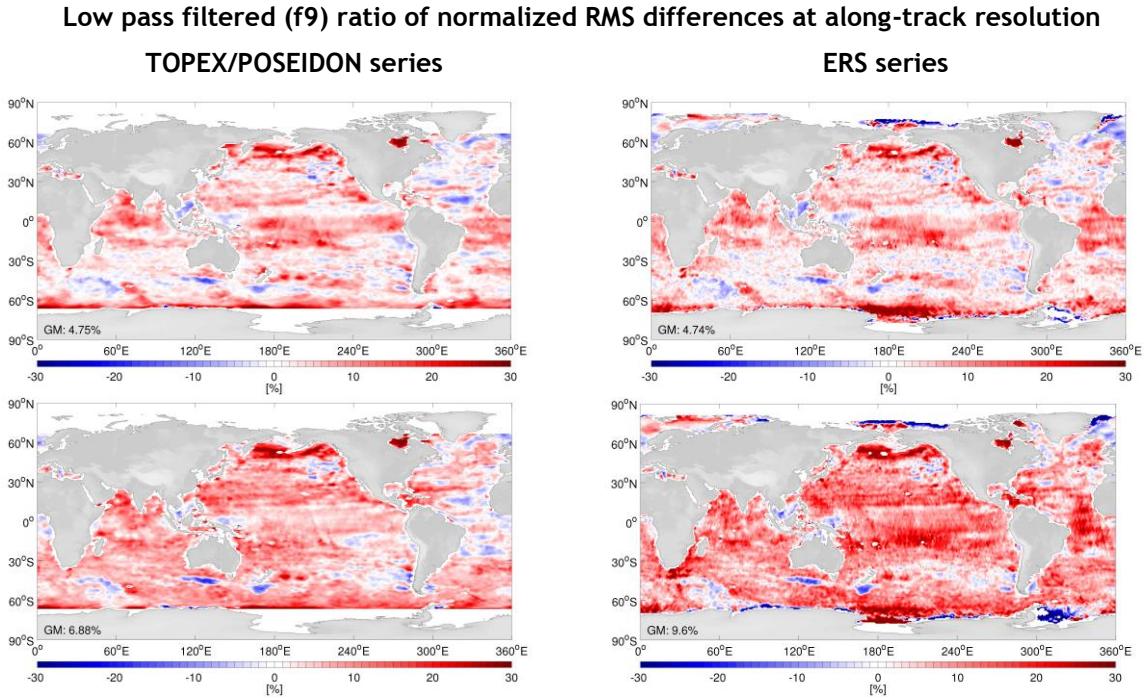

Figure 8: Low pass (f9) filtered ratio of normalized RMS differences *G0_SL0 / G1.1_SL1.1* (top) and *G0_SL0 / G1.1_SL2.0* (bottom), between the GECCO model and the satellite-time-series of TOPEX/POSEIDON, Jason-1 and Jason-2 (left) and of ERS-1, ERS-2 and ENVISAT (right). Compare top panels to Figure 3 (2nd row), for the analysis at model resolution.

Nevertheless, the GECCO2 synthesis benefits from the updated *SL1.1* data-set at least with respect to SL. Consequently, the question arises to what degree the GECCO2 synthesis improves in general and in particular to those additionally assimilated data. To tackle this question Figure 10 displays the change of the weighted global mean RMS differences of the GECCO2 synthesis after assimilating *SL1.1* instead of *SL0*. The reduction of normalized RMS differences indicates an improvement of 2.4 % for SSH, in the order of 1 % for SST of AMSRE and EN3 and of about 2.5 % for EN3 salinities, while having only minor increase in the order of 0.2 % for other variables.

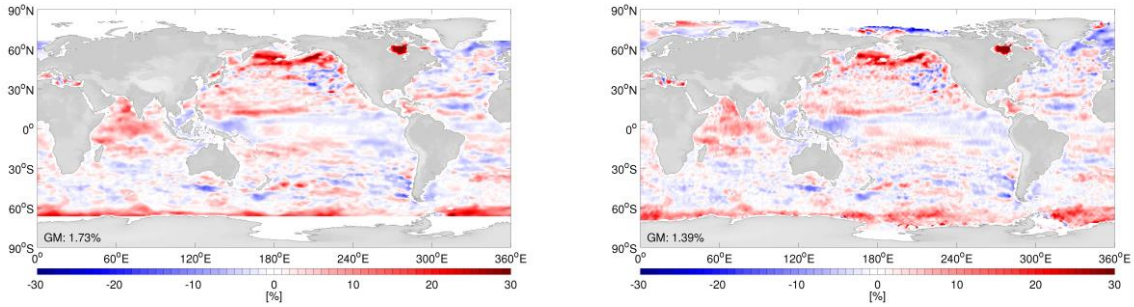

Figure 9: Low pass filtered (f9) ratio of normalized RMS differences *G0_SL1.1 / G1.1_SL1.1*, between the GECCO model and the satellite-time-series of TOPEX/POSEIDON, Jason-1 and Jason-2 (left) and of ERS-1, ERS-2 and ENVISAT (right). Compare to Figure 3, for the analysis at model resolution.

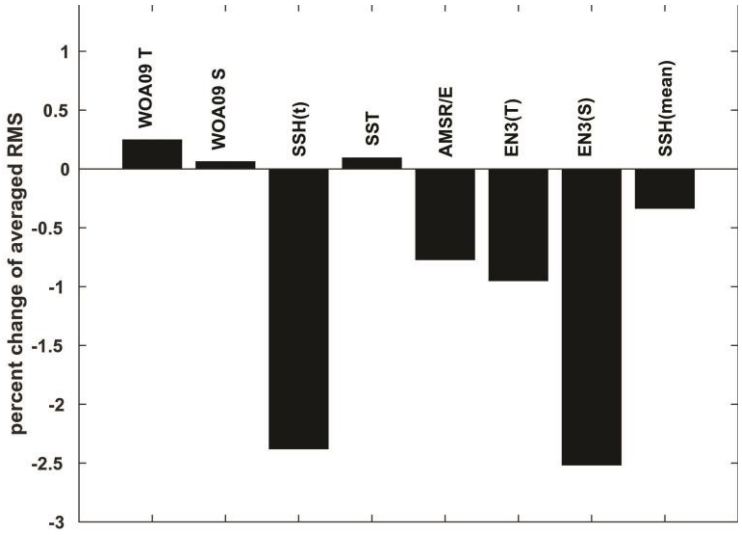

Figure 10: Global mean weighted RMS differences of GECCO2 for assimilated data sources after assimilation of *SL1.1* in percent. The weighting derives from the prior model – data errors that enter the cost function during the assimilation procedure. For absolute values see Figure 1 in Köhl (2015).

So far, the effect of applying the low pass filter (f9 and f11) to the AT *SL1.1* data has revealed larger improvements for larger filtering length scales (Figure 9 and Table 5). The main improvements seem to exist on length scales above several hundred km, and the question appears whether an effect on the smaller length scales exists, although for the smallest scales no significant effect can be expected due to the resolution of the GECCO2 model. The high pass filter is represented as difference between the individual SL data-set and its filtered (f9) product. The remaining ratios of normalized RMS differences for the high pass filtered data set are shown exemplarily for *G0_SL0 / G0_SL1.1* in Figure 11. For both satellite time series (TP and ERS) no clear influence can be seen at high frequencies.

A patchy structure is evident for both satellite time series. However, the ratios of normalized RMS differences of the high pass filtered data depict a different behavior for both satellite time series, indicating the different changes that were applied to improve the two different SL time series (Ablain et al., 2015). The global mean of -0.28 % (TP time series) and 0.16 % (ERS time series) cannot be assumed to be significant due to the patchy structure. As expected, the GECCO2 synthesis clearly shows no improvement on the small scales.

High pass filtered (HPf9) ratio of normalized RMS differences at along-track resolution

TOPEX/POSEIDON series **ERS series**

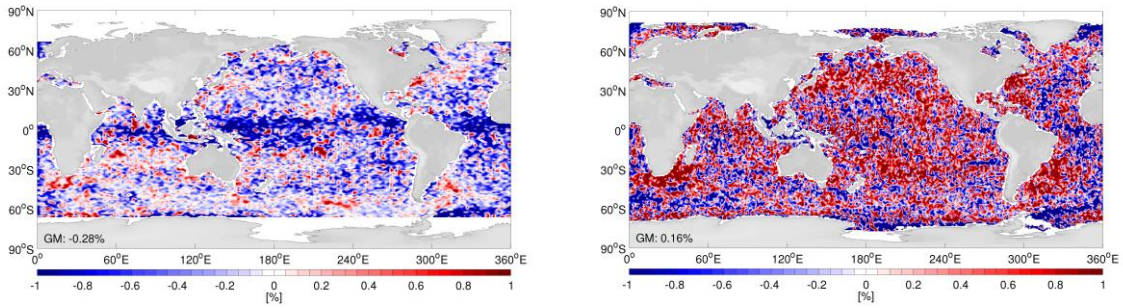

Figure 11: Ratio of normalized RMS differences of high pass filtered data for *G0_SL0* / *G0_SL1.1*, shown as percentages of improvement, for TP time series (left) and ERS time series (right). The figure is truncated at ±1 %. The global mean (GM) percentage of improvement is given for latitudes between 66°N and 66°S.

1.1.8. Regional sea level trends

The ratios of normalized RMS differences proved an advancement of the SL data set through the ESA SL_cci effort. The accuracy of the altimeter-based regional sea level trends Ablain et al. (2015) has been another aim of the ESA SL_cci effort. Therefore, the overall performance of the trends will be examined, to clarify the changes due to the update of the SL data sets *SL1.1* and *SL2.0*.

As the global mean sea level (GMSL) of the GECCO2 synthesis is zero at each time step and therefore, in order to treat the SL data-sets *SL0* and *SL1.1* in an analogous manner, the GMSL time series had to be subtracted from the SL data-sets accordingly, leaving the regional trends untouched. Thus, the GECCO2 synthesis can be used to assess the changes of the regional trend pattern of the SL data-sets.

The regional trends of *SL1.1* and *SL2.0* are shown in Figure 12 (1st and 2nd row) for the TP- and ERS-time series. Both indicate the strongest positive regional trends in the equatorial western Pacific and Indian Ocean. Further, positive regional trends are evident in the tropical Atlantic, western Pacific as well as in parts of the ACC. Regions of negative regional trends are the eastern Pacific, the northern Indian Ocean and parts of the subtropical Atlantic. Changes in the regional trends between *SL1.1* and *SL2.0* are evident, and show mostly a change in strength rather than a pattern change.

The corresponding regional trends of the GECCO2 synthesis for *G1.1*, sampled at the TP and ERS along-track positions and times are shown in the 3rd row of Figure 12, respectively. While the overall regional

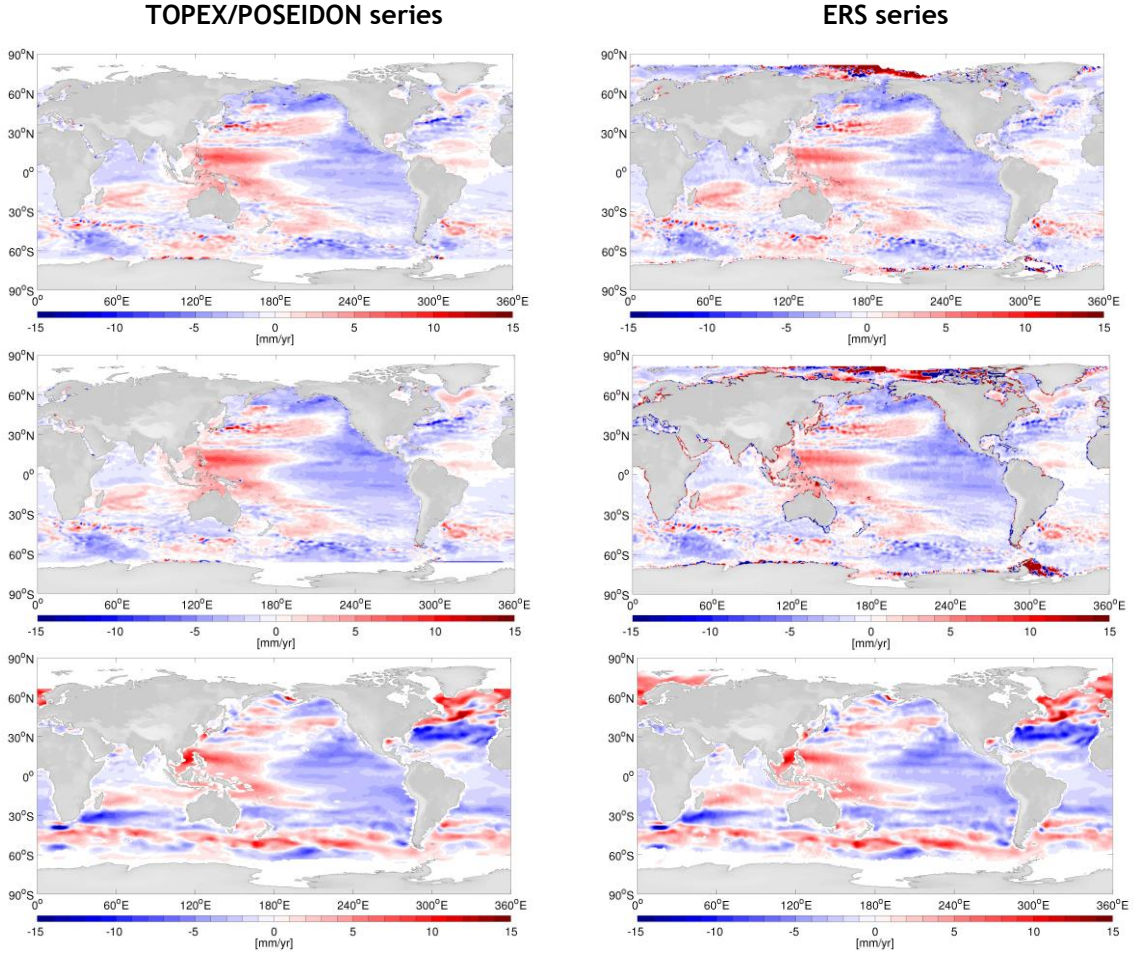

Figure 12: Regional trends of the SL data *SL1.1* (1st row), of *SL2.0* (2nd row) and of the GECCO2 synthesis *G1.1* (3rd row), for TP (left) and ERS time series (left).

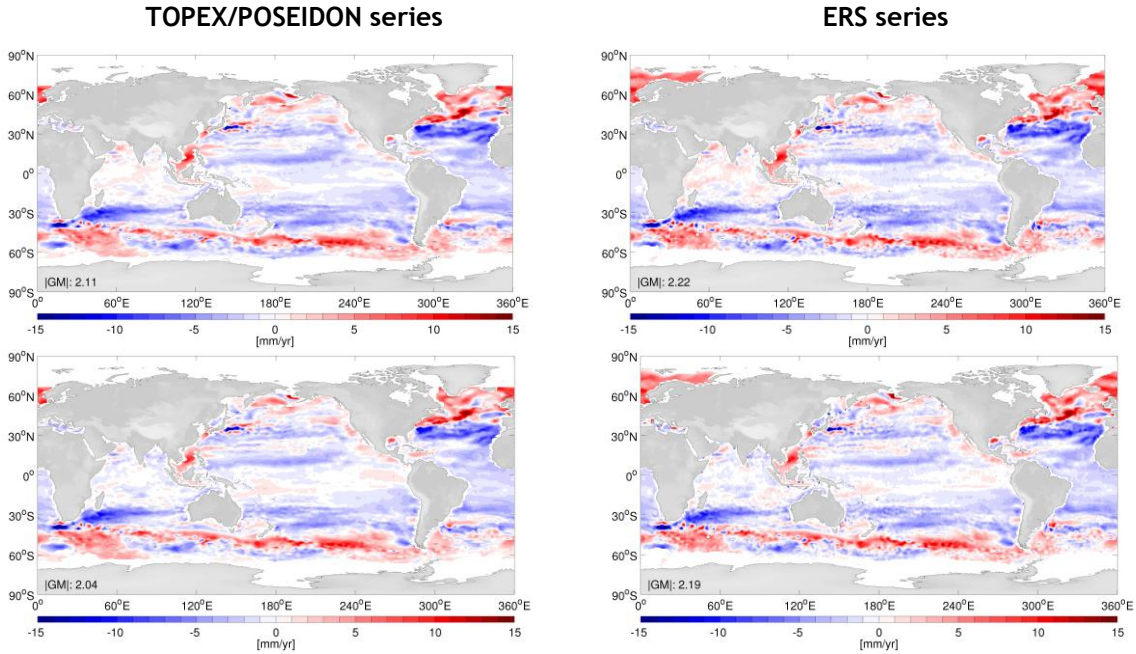

Figure 13: Regional trend differences *G1.1-SL1.1* (*D_G1.1SL1.1*, 1st row) and *G1.1-SL2.0* (*D_G1.1SL2.0*, 2nd row) for TP (left) and ERS time series (right). The absolute global mean (|GM|) percentage of the trend differences is given for latitudes between 66°S and 66°N.

trend pattern are depicted in *G1.1* as well, as the large trends of about 15 mm/yr in the western equatorial Pacific for *SL1.1* and *SL2.0*, *G1.1* has large positive trends in regions where the SL data sets do not, for example in parts of the ACC and in the north Atlantic. In order to accentuate the differences between the regional trends of data and model, Figure 13 shows the regional trend differences for *G1.1* - *SL1.1* (1st row) and *G1.1* - *SL2.0* (2nd row), hence, the closer to zero, the better the agreement between the regional trends of *G1.1* and the SL data set. Especially in the North Atlantic, the South China Sea and the ACC the regional trends disagree from each other, indicating, that the model physics of the GECCO2 synthesis provides a solution different from the SL data-sets. However, in most regions there is a close agreement.

The analysis has been conducted along the TP as well as along the ERS ground tracks, with their unequal temporal and spatial sampling pattern. When analyzing the regional trend differences in Figure 13, differences between the sampling patterns of TP (left) and ERS (right) can be seen. These differences of regional trend differences are shown in Figure 14 for the GECCO2 synthesis (left) and for the SL data-sets (right). Note that the GECCO2 synthesis has been sampled at the time and position of the respective SL data-sets. Therefore, the regional trend differences of TP-ERS time series in Figure 14 (2nd and 3rd row) are both for the *G1.1* synthesis, however, at the positions of *SL1.1* (2nd row) and *SL2.0* (3rd row).

The differences in Figure 14, resulting from sampling the GECCO2 synthesis results (left) as well as the SL data-sets (right) along the different satellite ground tracks from TP and ERS only, show a distinct pattern that is evident for the differences in the GECCO2 synthesis (left) as well as for the SL data-sets (right). The differences of regional trend differences between the TP and the ERS sampling are in the order of ±2 mm/yr, which is about an order of magnitude smaller than the actual signal. The differences do not change much between the *G0* and *SL0* (1st row), *G1.1* and *SL1.1* (2nd row), whereas the differences are smaller for *G1.1*(*SL2.0*) and *SL2.0* (3rd row).

To identify the changes among the data sets and the GECCO2 synthesis results the changes of regional trends between *SL0* and *SL1.1*/*SL2.0* as well as between *G0* and *G1.1* are addressed in Figure 15 in means of their respective differences. The large correlated structures of regional trend differences (Ablain et al., 2015) are here shown for the TP and ERS time series separately (Figure 15, 1st row),

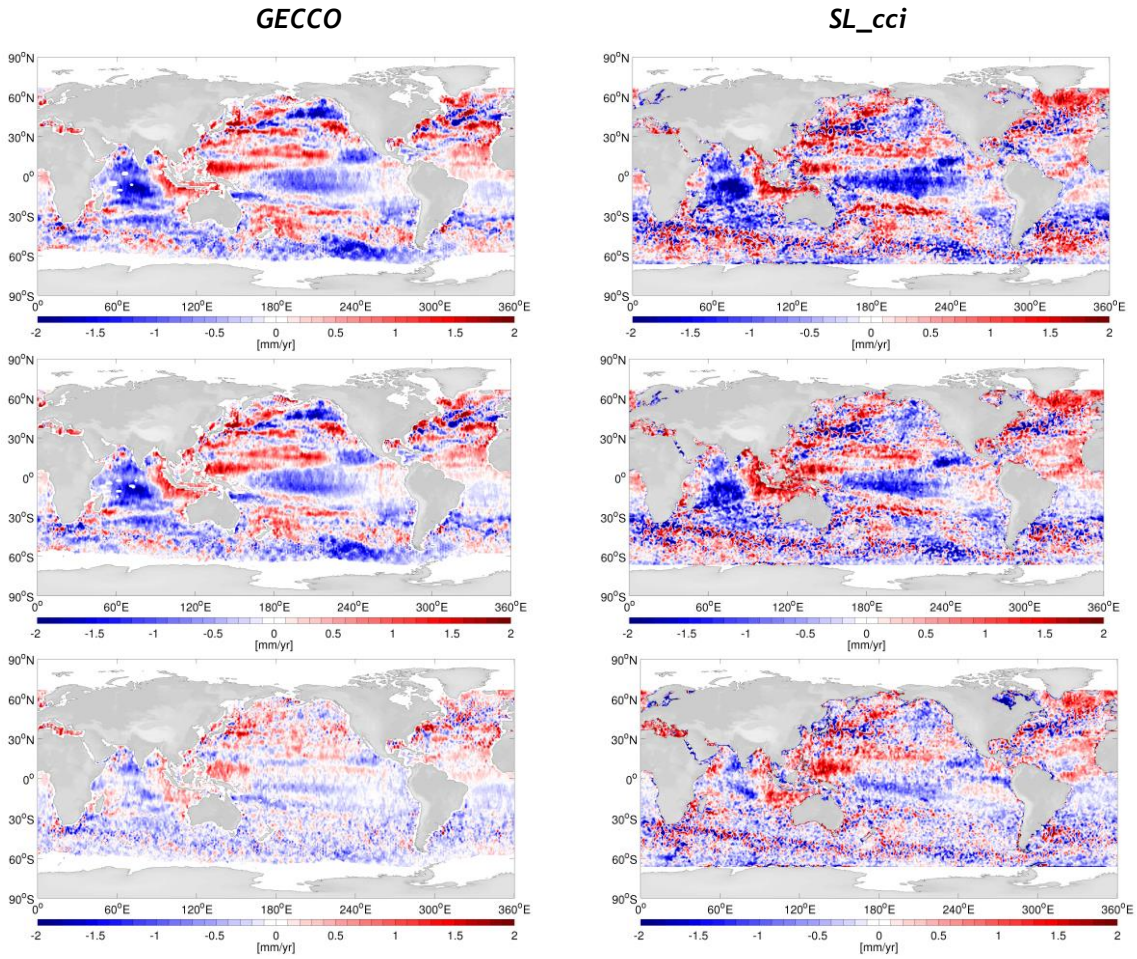

Figure 14: Regional trend differences of TP-ERS time series for the GECCO2 synthesis (RIGHT) and for SL data (LEFT), for *G0* and *SL0* (1st row), for *G1.1* and *SL1.1* (2nd row), and for *G1.1* and *SL2.0* (3rd row).

distinguishing again the different corrections applied for both SL satellite time series, as well as their sampling differences. For both satellite time series, the large scale pattern give a positive SL trend difference centered in the eastern equatorial Pacific and Gulf of Mexico, whereas a pattern of negative SL trend differences is centered in the ACC in the Indian Ocean. This pattern reflects to large parts the typical influence of the time variable gravity field of the earth in comparison to the static gravity field during orbit determination of the satellites. Next to the new orbit solutions the influence of other corrections and altimeter models is visible (compare figure 6 in Ablain et. al., 2015). The global mean of the absolute regional trend differences (|GM|) are given in the lower left corner of the plots and, additionally, are given in Table 5 for comparison. According to the global absolute mean values, the regional trends changed by as much as 1.11 and 1.52 mm/yr for the TP and ERS time series, respectively. The regional trend differences of *SL2.0-SL0* (2nd row) show the changed pattern in regional trend differences. The positive SL trend differences have two center, in the western north Pacific/northern Indian Ocean and the second around South America. The differences between TP- (0.87 mm/yr) and ERS-series (5.7 mm/yr) are the result of different corrections for the Orbit, Ionospheric, Sea State Bia (SSB), as can be seen in the tables 1 of Ablain et. al. (2015) and Quartly et. al. (2017).

While *G0* and *G1.1* tried to adapt to the assimilated data-sets *SL0* and *SL1.1*, respectively, the differences between the regional trends of *G0* and *G1.1* (Figure 15, 3rd row) is expected to provide a version of the trend differences between *SL0* and *SL1.1* filtered by the assimilation procedure for both satellite time series. Apparently, the regional trend differences of the GECCO2 synthesis

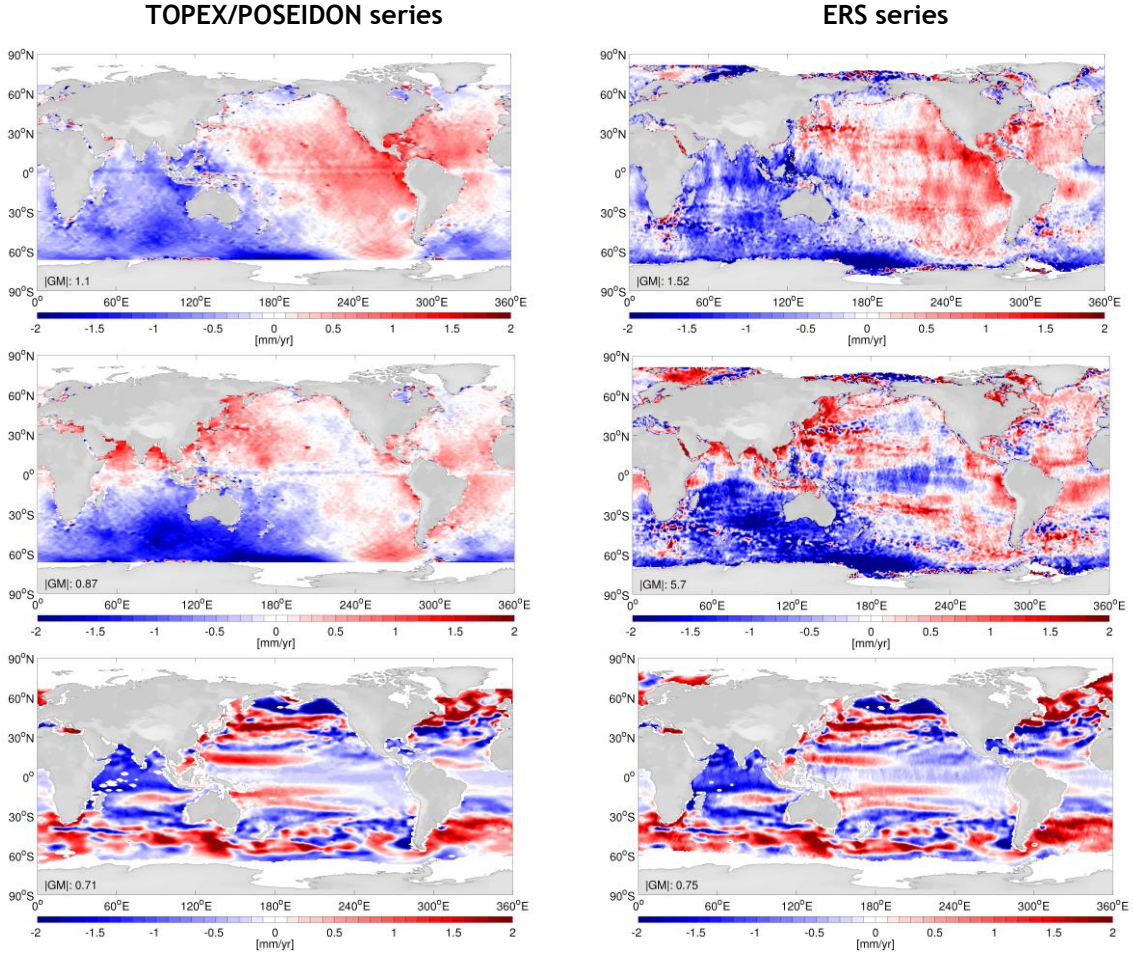

Figure 15: Regional trend differences of (1st row) the two data sets *SL1.1-SL0*, (2nd row) the two data sets *SL2.0-SL0* and (3rd row) the two GECCO2 assimilation runs *G1.1-G0*, for TP-series (left) and ERS-series (right). The absolute of global mean (|GM|) percentages of regional trend differences are given for latitudes between 66°S and 66°N.

G1.1 - G0 do not reflect the large scale pattern of regional trend changes as seen for the SL data-set (Figure 15, 1st and 2nd row). The reason can be the smallness of the trend differences itself. As indicated above the solution cannot be considered converged and some changes may be not causally connected to the changes of the input data.

Using *G0*, *G1.1* and *G1.1sst* as measure to evaluate the regional trends of *SL0*, *SL1.1* and *SL2.0*, the absolute global mean regional trend differences between all possible data-model combinations are shown in Table 6 as *GX - SLX*. The smaller absolute regional trend differences indicate a closer agreement of model and data in terms of their regional trends. For *G0* the global mean regional trend differences *G0-SL0* and *G0-SL1.1* are in the same order of magnitude, and only slightly larger for *SL1.1* and slightly smaller for *SL2.0*, indicating neither a clear improvement nor a degradation of the *SL1.1* and *SL2.0* data sets in terms of regional trends, as compared to the GECCO2 synthesis. The same holds true for the global mean trend differences of *G1.1*, as these global mean regional trend differences are nearly identical to the ones of *G0*. The additional assimilation of the updated SST (*G1.1sst*), however, leads to larger regional trend differences as compared to *G0* and *G1.1*, indicating a degradation of regional trend differences as compared to *G0* and *G1.1*. Therefore, no further assessment is undertaken for the GECCO2 synthesis *G1.1sst*.

To assess the changes of the regional trend differences between data and model directly, the absolute values of their differences (*D_GXSLX*) are subtracted respectively, as shown in the lower three rows of Table 6 for the global mean and in Figure 16 for the regional distribution. Using this measure, the

TREND differences [mm/yr]	TP - data set		ERS - data set	
	SL1.1	SL2.0	SL1.1	SL2.0
|*SLX.X - SL0*|	1.11	0.87	1.52	5.70
|*G1.1 - G0*|	0.71	0.70	0.75	0.83
|*G0 - SL0*|	2.02		2.15	
|*G0 - SLX.X*|	2.07	2.01	2.18	2.15
|*G1.1 - SL0*|	2.04	2.04	2.20	2.20
|*G1.1 - SLX.X*|	2.11	2.04	2.22	2.19
|*G1.1*sst - *SL0*|	2.28		2.47	
|*G1.1*sst - *SL1.1*|	2.35		2.48	
D_*G1.1SLX.X* - D_*G0SL0*	0.92	0.89	0.98	1.13
D_*G1.1SLX.X* - D_*G0SLX.X*	0.71	0.70	0.74	0.73
|D_*G1.1SLX.X*| - |D_*G1.1SL0*|	0.06	0.00	0.02	-0.02
|D_*G1.1SLX.X*| - |D_*G0SLX.X*|	0.03	0.03	0.04	0.04
|D_*G1.1SLX.X*| - |D_*G0SL0*|	0.08	0.02	0.07	0.03

Table 6: Global mean ratios of trend differences for TP and ERS data sets in mm/yr, computed at the along-track points. The upper two rows illustrate the trend differences between the SL products and between the different GECCO2 assimilation runs itself. The middle rows give the model-data differences, while the lower rows give the differences between the model-data differences and the respective differences of their absolute differences.

expected better data *SL1.1* and the expected better model synthesis *G1.1* are anticipated to have the smaller absolute global mean differences (|*D_G1.1SL1.1*|) in terms of regional trends (see Table 6). Therefore, negative values indicate a closer agreement between the first model and data, whereas positive values indicate a closer agreement between the second. However, for the comparison of |*D_G1.1SL1.1*|-|*D_G1.1SL0*|, the resulting positive differences (0.06 mm/yr for TP and 0.02 mm/yr for ERS) of the global mean differences of the regional trends indicate a closer agreement of *G1.1* to *SL0* as to *SL1.1*. When comparing regional trend differences of the GECCO2 synthesis *G0* and *G1.1* against *SL1.1* (|*D_G1.1SL1.1*|-|*D_G0SL1.1*|), *G0* seems to be in closer agreement to *SL1.1* than *G1.1*. Even more when comparing the differences *D_G1.1SL1.1-D_G0SL0*, the closer agreement is found for the *SL0* data-set and *G0*. The slightly smaller differences of regional trend differences between the *SL2.0* data and the model indicate that the trends of the *SL2.0* data set are in better agreement with the GECCO2 synthesis, although, the global mean changes from one comparison to the other are so small that they must be seen as not significant.

The regional distribution of trend distribution differences is given in Figure 16. The comparison of *SL0* and *SL1.1* (|*D_G1.1SL1.1*|-|*D_G1.1SL0*|, Figure 16, 1st row) shows an improvement (blue) of the *SL1.1* data-set in the north Atlantic. Yet, in the same region, the comparison of *G0* and *G1.1* (|*D_G1.1SL1.1*|-|*D_G0SL1.1*|, 2nd row, left) shows a degradation of *G1.1* (red). The combined effect can be seen in the 3rd row.

We note, however that, because the global mean differences of regional trend differences are very small, the comparisons of regional trends of the SL products to the GECCO2 synthesis results are not able to detect an improvement or degradation of the regional trend pattern. The different regional trends of the data sets and the GECCO2 synthesis are the reason for the inability to clearly identify the regional trend changes from *SL0* to *SL1.1*/*SL2.0* as improvement or degradation.

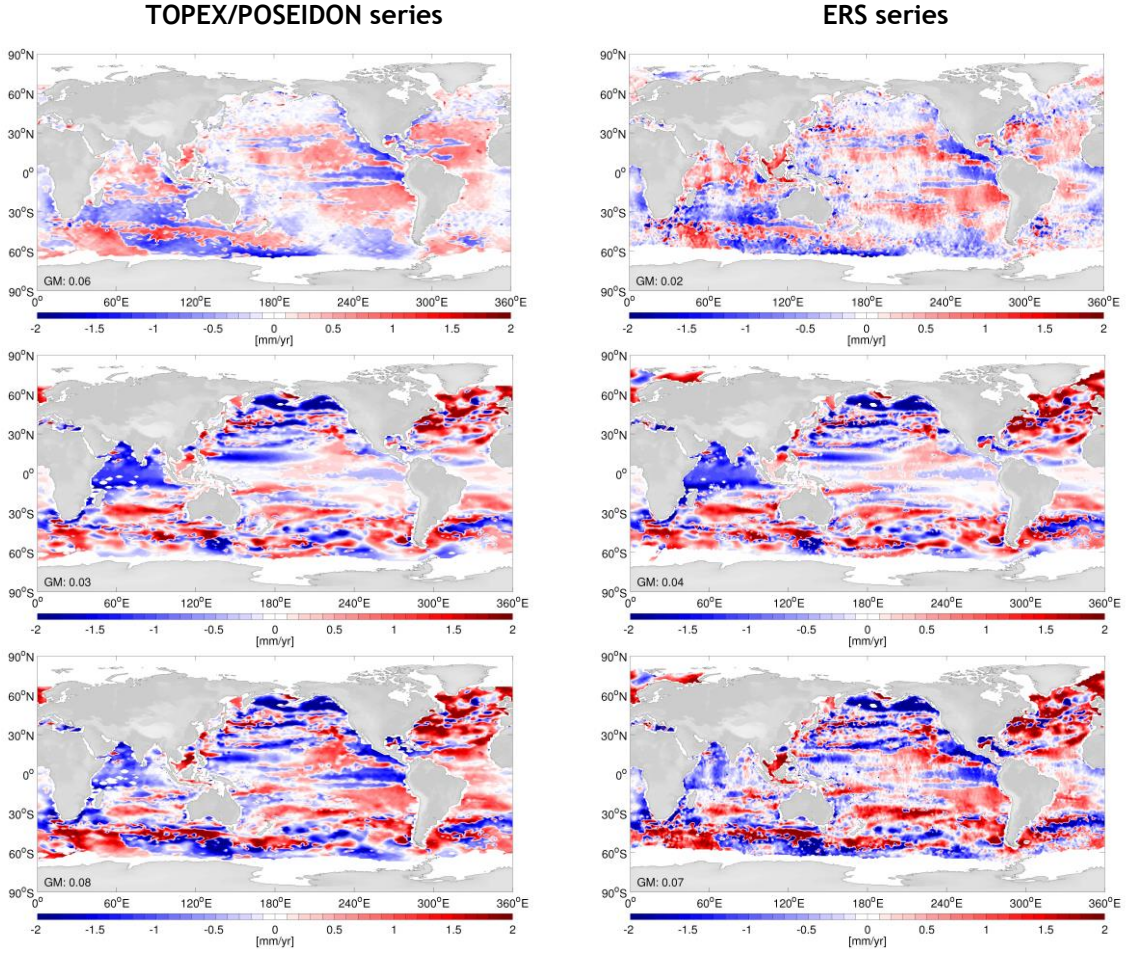

Figure 16: Differences of absolute regional trend differences of (1st row) |*D_G1.1SL1.1*|-|*D_G1.1SL0*|, of |*D_G1.1SL1.1*|-|*D_G0SL1.1*| (2nd row) and (3rd row) of |*D_G1.1SL1.1*|-|*D_G0SL0*|, for TP-series (left) and ERS-series (right). The global mean (GM) percentages of absolute regional trend differences are given for latitudes between 66°S and 66°N.

1.1.9. Annual sea level signal

Sea level has a significant annual signal which is an important component of the overall SL signal. In this section the influence of the changes on the annual signal from *SL0* to *SL1.1* and further to *SL2.0* is evaluated. For clarity the evaluation is shown for the TP data set only. The annual SL signal has been calculated as harmonic fit individually for each along track satellite position and is given as amplitude of the harmonic annual signal and its corresponding start date (phase). The annual SL signal has amplitudes of more than 150 mm in the equatorial Pacific and Indian Ocean as well as in the Kuroshio and Gulf Stream region, and is shown in Figure 17 (1st row, left) exemplarily for *SL1.1*. In most other parts of the world ocean the annual signal does not exceed 50 mm. The phase pattern (Figure 17, 1st row, right) show a clear difference between the northern and southern hemisphere reflecting in part the annual changes of incoming solar radiation. Solar radiation influences the thermal heating and leads to thermal expansion of the upper ocean. Therefore, the changing solar radiation has an influence on the annual steric SL signal. The corresponding annual SL pattern for the GECCO2 synthesis *G1.1* (Figure 17, 2nd row, left) shows similar structures as the SL data, for the amplitudes as well as for the phase. The amplitude and phase differences between *G1.1* and *SL1.1* are displayed in the 1st row of Figure 18. The largest differences in amplitude occur in the Gulf Stream region, the equatorial eastern Pacific and in parts of the ACC. The phase differences are

patchy and

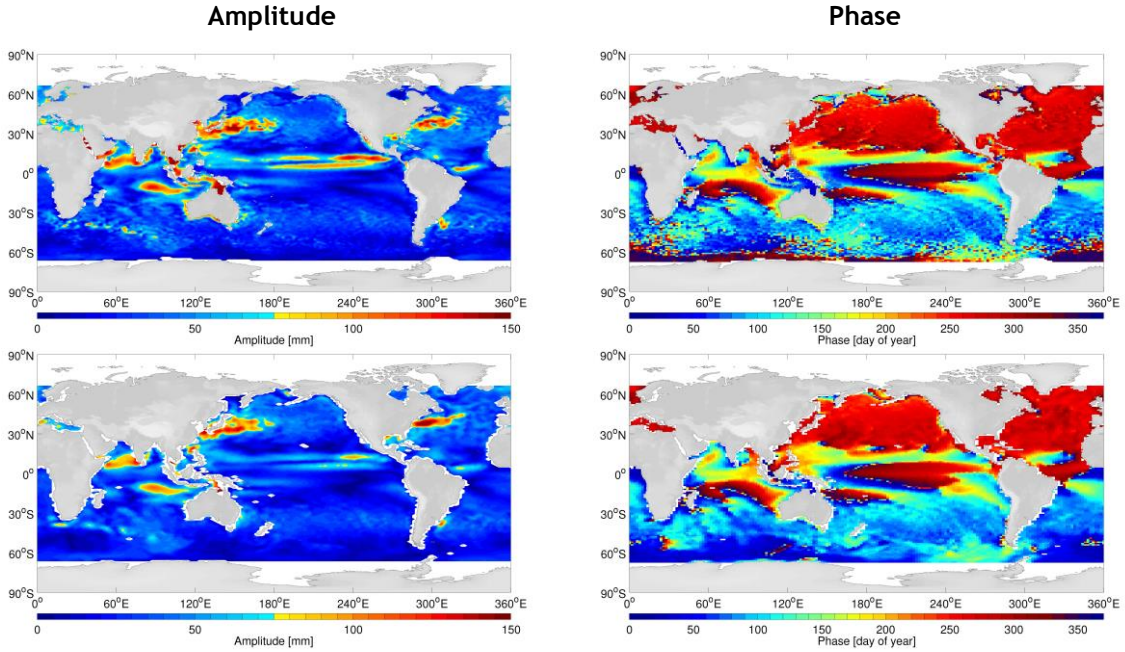

Figure 17: Annual amplitude (left) and phase (right) of *SL1.1* (1st row) and of *G1.1* (2nd row), for TP-series.

are in the range of ±50 days. The 2nd row of Figure 18 shows the amplitude and phase differences of *G1.1* and *SL2.0* as comparison. The regional changes from *SL1.1* to *SL2.0* are small and reflect changes in strength rather changes of pattern. The absolute values of the global mean amplitude and phase differences between the GECCO2 solution and the SL data sets, are given in the lower left corner of the plots. The amplitude differences demonstrate, that the *SL2.0* data set is in closer agreement to the GECCO2 solution (8.53 mm) as compared to *SL1.1* (8.57 mm). The same is true for the global mean phase differences. They reduce from 28.46 days to 27.06 days.

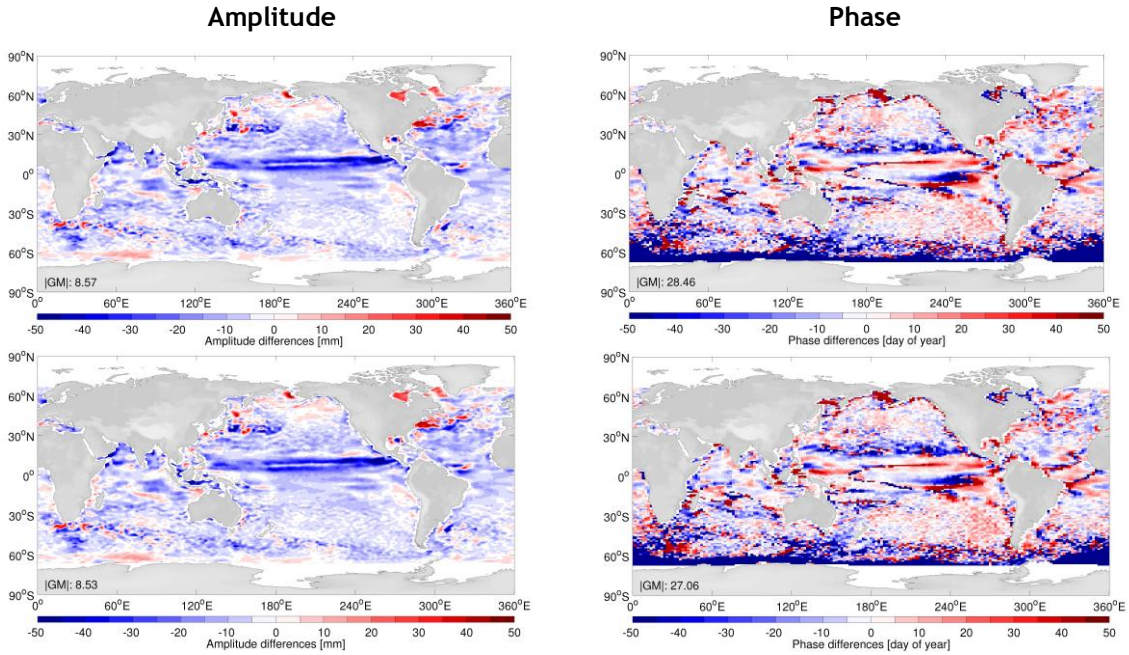

Figure 18: Annual amplitude and phase-differences as *G1.1-SL1.1* (1st row) and as *G1.1-SL2.0* (2nd row), for TP-series. The absolute global mean (|GM|) percentages of annual amplitude and phase-differences are given for latitudes between 66°S and 66°N.

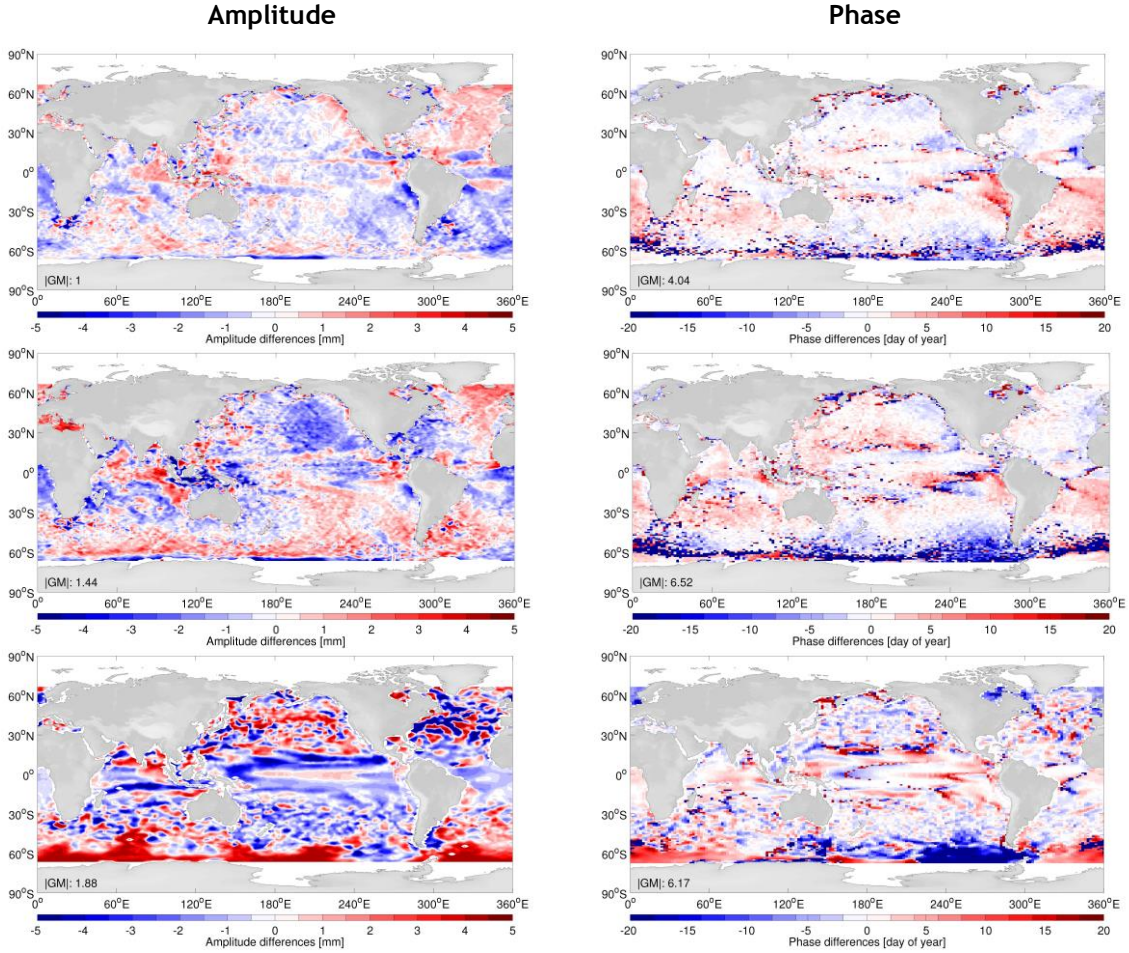

Figure 19: Annual amplitude-differences (left) and phase-differences (right) of the two data sets *SL1.1-SL0* (1st row), *SL2.0-SL0* (2nd row), and of the two GECCO2 assimilation runs *G1.1-G0* (3rd row). For TP-series only.

Next to the differences between *G1.1* and *SL1.1*, the changes between the data-sets *SL0* and *SL1.1* (Figure 19, 1st row) and *SL0* and *SL2.0* (2nd row), as well as between *G0* and *G1.1* (Figure 19, 3rd row) are equally important. Large scale pattern can be seen for the differences of the SL data-sets *SL1.1-SL0* (1st row), with amplitude differences of more than ±5 mm as well phase differences of more than ±20 days and a global mean of absolute amplitude differences of 1 mm. Therefore, the absolute phase and amplitude differences between *SL0* and *SL2.0* (2nd row) are larger (1.44 mm) as compared to *SL1.1* before (1 mm), indicating that the *SL2.0* data set is further away from *SL0* in terms of the annual amplitude and phase signal, and as could be seen from Figure 17, is now in closer agreement to *G1.1*. In contrast, the amplitude differences between the two GECCO2 synthesis results *G0* and *G1.1* (Figure 19, 3rd row, left) have a different structure, and are even larger as those between the SL data-sets. The phase pattern differences between *G0* and *G1.1* (Figure 19, 3rd row, right), show different pattern as well, but showing a smaller global mean phase difference of 6.17 days.

To evaluate, whether the updated *SL1.1* and *SL2.0* data-sets have an improved annual signal when compared to the GECCO2 synthesis, the 1st row of Figure 20 shows the differences between the absolute differences between the GECCO2 synthesis *G1.1* and the data sets *SL1.1* and *SL0* as *|D_G1.1SL1.1|-|D_G1.1SL0|*, while the 2nd row is the same but for *G1.1* and the data sets *SL2.0* and *SL0* as *|D_G1.1SL2.0|-|D_G1.1SL0|*. As in section 1.1.8 for the trends (Figure 16), blue indicates regions where the data-sets *SL1.1* and *SL2.0* are in closer agreement to *G1.1*, as *SL0* was to *G1.1*.

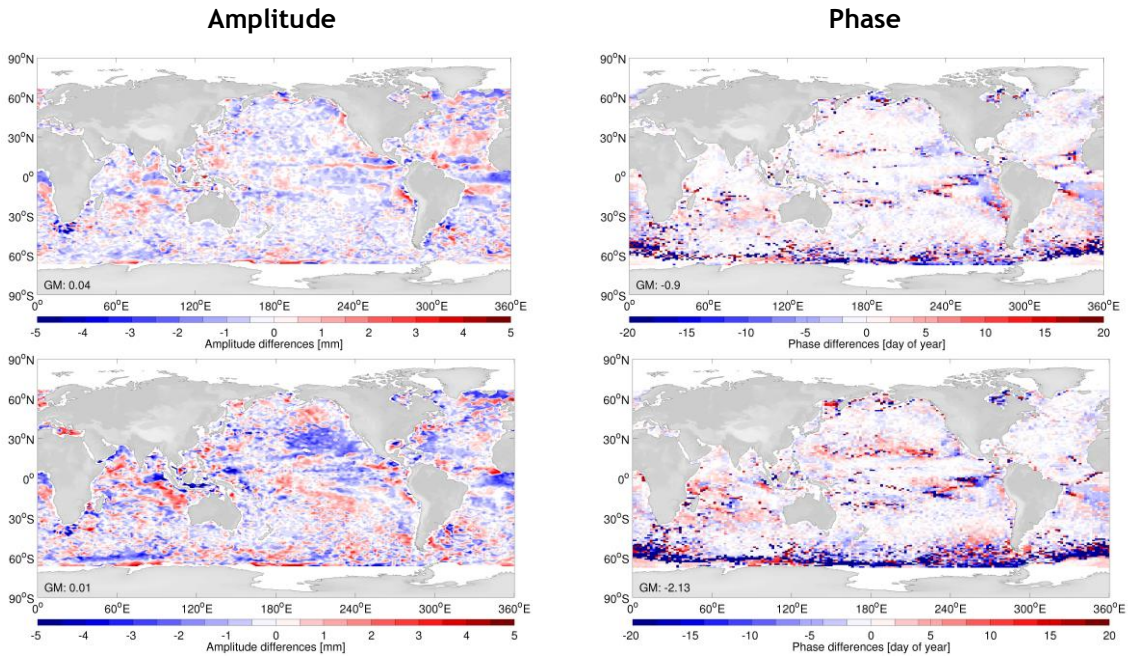

Figure 20: Absolute annual amplitude (left) and phase-changes (right) of absolute amplitude and phase-differences of (1st row) |*D_G1.1SL1.1*|-|*D_G1.1SL0*| and (2nd row) |*D_G1.1SL2.0*|-|*D_G1.1SL0*|, for TP-series.

A very patchy pattern is evident for *SL1.1* (1st row, left), that sums up to a GM amplitude difference of absolute differences of 0.04 mm/yr. The positive global mean value indicates a less good agreement of the amplitude differences of the updated *SL1.1* data set to *G1.1* as compared to *SL0*. The pattern gets more structured for *SL2.0* (2nd row, left) with a smaller GM amplitude difference of absolute differences of 0.01 mm/yr. The reduction indicates a better agreement for the comparison with *SL2.0*. On the other hand, the phase differences of absolute differences between

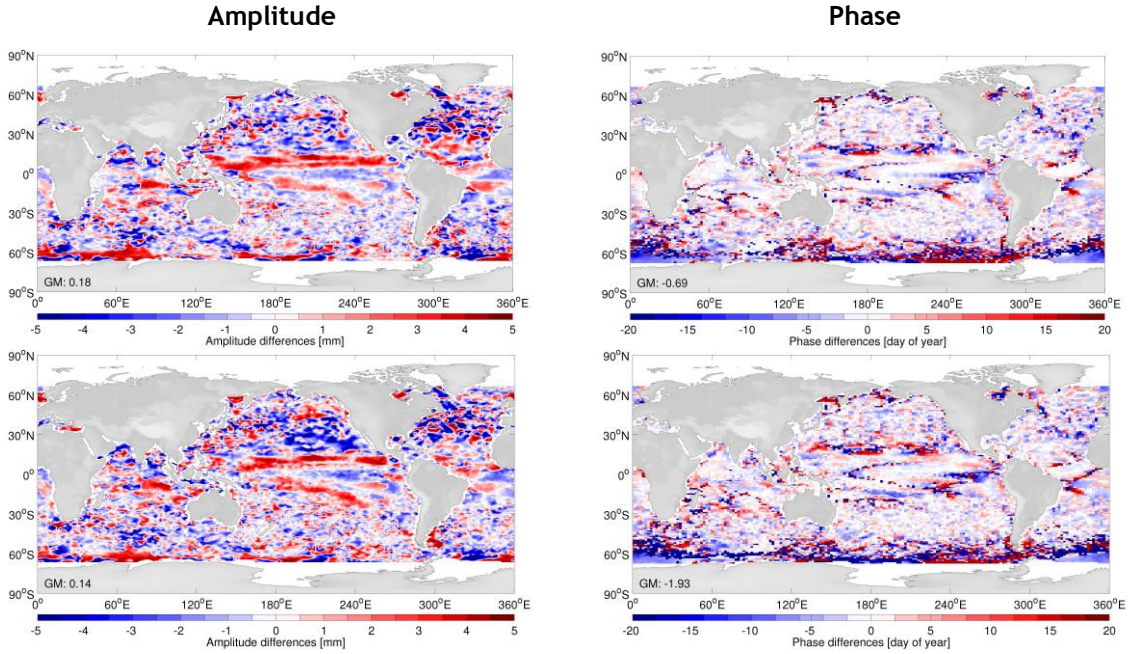

Figure 21: Absolute annual amplitude (left) and phase-changes (right) of absolute amplitude and phase-differences of (1st row) |*D_G1.1SL1.1*|-|*D_G0SL0*| and (2nd row) |*D_G1.1SL2.0*|-|*D_G0SL0*|, for TP-series.

G1.1 and the data sets (Figure 20, right) both show equivalent pattern for the differences with *SL1.1* (1st row, right) and *SL2.0* (2nd row, right). The global mean differences in the phase shift between model and data are negative for *SL1.1* and for *SL2.0*, indicating the improvement in the phasing of the annual signal of both SL_cci data sets, while *SL2.0*, as before for the amplitude differences, is improved as compared to *SL1.1*.

When further not only taking the improvement of the SL_cci data-sets into account, but additionally the influence of the assimilation of the *SL1.1* data set into the GECCO2 synthesis, even larger changes get evident as seen in Figure 21 for |*D_G1.1SL1.1*|-|*D_G0SL0*| in the 1st row and in the 2nd row for |*D_G1.1SL2.0*|-|*D_G0SL0*|. The global mean differences of absolute model data differences are positive, and further, are even larger as compared to Figure 20, it indicates that the annual signal of *SL0* is in better agreement with the annual signal of *G0* as compared to the difference between the SL_cci data sets and *G1.1*. As before, in Figure 20, the differences with the *SL2.0* data set have a smaller global mean absolute difference, indicating an improvement over *SL1.1*. As before for the absolute differences using only the *G1.1* synthesis (Figure 20,right), the annual phase is in better agreement between the SL_cci data sets and *G1.1*, as compared to SL0 and G0 (Figure 21, right), as indicated by the negative global mean differences. The *SL2.0* has again a smaller global mean difference of absolute differences (GM -1.93 days), indicating the further improvement as compared to the improvement of *SL1.1* (GM -0.69 days).

However, the overall influence of the updated data-sets *SL1.1* and *SL2.0* on the annual signal is very small when compared to the GECCO2 synthesis results.

1.1.10. Conclusions

In this study we were able to demonstrate that the new SL_cci data sets *SL1.1* and *SL2.0*, generated by the ESA SL_cci project, are in better agreement with the GECCO2 synthesis and the various global oceanographic data sets assimilated therein (Köhl, 2015), than this was the case with earlier versions of the same data set (*SL1* and *SL0*). The improvement can be shown to exist separately for both the TOPEX/POSEIDON, Jason-1 and Jason-2 time series as well as for the ERS-1, ERS-2 and ENVISAT data set. The study reveals, that especially in regions characterized by small SSH variability and thereby small signal-to-noise ratio in the SSH data, improvements can be on the order of 30% of previously existing model-data residuals. Geographically, those improvements are especially obvious in all equatorial regions, on the Argentine shelf as well as in large parts of the ACC.

However, we note that in some regions we can find degradations, i.e., the residuals do become larger upon comparing to the *SL1.1* data set, particularly in regions where the previous GECCO2 synthesis has little skill in representing the altimeter data. In those regions, for instance in parts of the North Atlantic and the Southern Ocean, changes are therefore likely to be insignificant. The *SL2.0* data set has been further improved, compared to *SL1.1*. Therefore, many regions that did not show an improvement in *SL1.1* can now be shown to have smaller residuals and are thus closer to the GECCO2 model. As can be expected from this, the GECCO2 synthesis was further improved upon the assimilation of the new *SL1.1* data-set. However, this does not hold for all regions suggesting incompatibility of the model physics with the information content of SSH data in those regions. The model-data differences are much larger than the anticipated data uncertainties and the solution cannot be regarded as fully converged and independent of the starting point. The synthesis has therefore a somewhat stochastic component, where the changes of results may not be directly related to changes of the input data, particularly true in those regions where the model is not able to represent the dynamics, therefore, issues with the data cannot be ruled out.

Nevertheless, we are able to show that through the assimilation of the *SL1.1* data other model-data residuals are also reduced such as differences to in situ T and S profiles, indicating that the *SL1.1* data set is in better agreement with the model dynamics and with the information content of other ocean data sets. However, these changes are naturally small and over large parts of the world ocean statistically insignificant, since the overall improvement in agreement between GECCO2 and the SL products is only a few percent. In contrast, the impact on sea level trends, its seasonal amplitude and phase remain inconsistent with no clear connection to the pattern of the changes

between *SL0* and the SL_cci data sets *SL1.1* and *SL2.0*. The additionally assimilation of the ESA SST_cci (*G1.1sst*) did not had a strong influence.

Our work suggests that using gridded altimeter products, shows smaller residuals relative to the along track data. We were able to show that this apparent difference results simply from the more heavily smoothed gridded products. Smoothing the AT data in a similar manner does lead to smaller residuals. We nevertheless belief, that the use of AT data over gridded fields has the strong advantage of constraining the barotropic fast movements in the model. Respective signals are being filtered out in gridded fields. Nevertheless our study also suggests that in future GECCO approaches we should either use a more sophisticated error covariance allowing to more effectively down-weight eddy signal in the data, thereby constraining more the large-scale signal of the models. Alternatively the along-track data can be filtered to remove the eddy component. In that case the data error information used during the assimilation can substantially be decreased allowing to more effectively feel the large-scale altimetry. Both approaches need to be tested in future assimilation runs. They will likely lead to assimilation results that are better constrained by altimeter data sets. An assimilation of *SL2.0* into future GECCO assimilation runs would be preferred depending on its timely availability.

1.1.11. References

Ablain, M., A. Cazenave, G. Larnicol, M. Balmaseda, P. Cipollini, Y. Faugère, M. J. Fernandes, O. Henry, J. A. Johannessen, P. Knudsen, O. Andersen, J. Legeais, B. Meyssignac, N. Picot, M. Roca, S. Rudenko, M. G. Scharffenberg, D. Stammer, G. Timms, and J. Benveniste, (2014) Improved sea level record over the satellite altimetry era (1993–2010) from the Climate Change Initiative project. Ocean Sci., 11: 67--82, doi:10.5194/os-11-67-2015, 2015

Cazenave, A., G. Larnicol, J.-F. Legeais, M. Ablain, Y. Faugère, S. Mbajon Njiche, G. Timms, B. Meyssignac, M. Balmaseda, H. Zuo, J. Johannessen, M. G. Scharffenberg, D. Stammer, O. Andersen, P. Knudsen, L. Zawadzki, P. Thibaut, J.-C. Poisson, B. Picard, L. Carrère, F. Mertz, O. Lauret, S. Rudenko, C. Farquhar, Ed. Pechorro, M. Roca, P. Nilo, P. Cipollini, F. Calafat, J. Fernandes, C. Lazaro, G. Quartly, A. Kurekin, F. Nencioli, L. Fenoglio-Marc, J. Benveniste, B. Lucas, S. Dinardo, and A. Ambrózio, (2014), ESA Sea Level Climate Change Initiative (ESA SL_cci): SEA LEVEL ESSENTIAL CLIMATE VARIABLE PRODUCTS, Version 1.1., December 2014. DOI: 10.5270/esa-sea_level_cci-1993_2013-v_1.1-201412

Köhl A. and D. Stammer (2008a), Variability of the Meridional Overturning in the North Atlantic from the 50 years GECCO State Estimation, J. Phys. Oceanogr., 38, 1913-1930, doi:10.1175/2008JPO3775.1

Köhl A. and D. Stammer (2008b), Decadal Sea Level Changes in the 50-Year GECCO Ocean Synthesis. J. Climate., 38, 1876-1890, doi:10.1175/2007JCLI2081.1

Köhl A. (2015), Evaluation of the GECCO2 ocean synthesis: transports of volume, heat and freshwater in the Atlantic. Q.J.R. Meteorol. Soc., 141: 166-181, doi:10.1002/qj2347

Menemenlis, D., I. Fukumori, and T. Lee (2005). Using Green's functions to calibrate an ocean general circulation model. Mon. Weather Rev., 133, 1224–1240

Merchant, C. J., O. Embury, J. Roberts-Jones, E. Fiedler, C. E. Bulgin, G. K. Corlett, S. Good, A. McLaren, N. Rayner, S. Morak-Bozzo, and C. Donlon, (2014), Sea surface temperature datasets for climate applications from Phase 1 of the European Space Agency Climate Change Initiative (SST CCI). Geosci. Data J., 1: 179--191, doi: 10.1002/gdj3.20

Quartly, G. D., J.-F. Legeais, M. Ablain, L. Zawadzki, M. J. Fernandes, S. Rudenko, L. Carrere, P. N. Garcia, P. Cipollini, O. B. Andersen, J.-C. Poisson, S. M. Njiche, A. Cazenave, J. Benveniste, (2017), A new phase in the production of quality-controlled sea level data, Earth Syst. Sci. Data, 9, 557-572, doi:10.5194/essd-9-557-2017.

Scharffenberg M. G., A. Köhl, D. Stammer, (2017), Testing the Quality of Sea-Level Data Using the GECCO Adjoint Assimilation Approach. Surv. Geophys., 38: 349-383, doi:10.1007/s10712-016-9401-3

Stammer D., K. Ueyoshi, A. Köhl, W. G. Large, S. A. Josey and C. Wunsch, (2004). Estimating air-sea fluxes of heat, freshwater and momentum through global ocean data assimilation, J. Geophys. Res., 109, C05023,_doi: 10.1029/2003JC002082.

Stammer D., A. Köhl, C. Wunsch, (2007), Impact of accurate geoid fields on estimates of the ocean circulation. J. Atmos. Oceanic Technol., 24 (8): 1464--1478, doi: 10.1175/JTECH2044.1

Stammer D., M. Balmaseda, P. Heimbach, A. Köhl, A. Weaver, (2016), Ocean Data Assimilation in Support of Climate Applications: Status and Perspectives. Ann. Rev. Mar. Sci., 8: 491--518, doi: 10.1146/annurev-marine-122414-03411

1.2. WP5120: Assessment of climate signals via multi-model approach (ECMWF)

1.2.1. Introduction

The ESA Sea Level Climate Change Initiative (hereafter, SL_cci) Project provide long-term satellite-based Sea Level products (along-track and mapped) for climate application. The Sea Level Essential Climate Variable version 1.1 (ECV1.1 in what follows) has been released in 2015 as the outcome of the Phase II of SL_cci. It is an update of Version 1.0 (Ablain, et al., 2015) with the coverage extended to the end of 2014. In 2016, the latest reprocessed Sea Level ECV2.0 product was released that spans the period of 1993-2015. Sea Level ECV2.0 has been produced with new altimeter standards, including but not only, new orbit solution, atmospheric correction, wet troposphere corrections, mean sea surface and ocean tide model (see Sea Level CCI newsletter Issue 10 for more details).

Assessment of these two new ECV products have been carried out via multi-model approach, by comparing with ocean-only reanalyses from ECMWF, as well as with other reference SL data set (AVISO and SL_cci version 1). Ocean Reanalyses (ORAs in what follows) are historical reconstructions of the ocean states, obtained by using an ocean model driven by atmospheric forcing fluxes, and constrained by ocean observations (surface and subsurface) via data assimilation methods. ORAs are commonly used for studying climate signals, which is sensitive to temporal variations of the observing system, to the errors of the ocean model, atmospheric fluxes and assimilation method. The uncertainty of climate signals as represented by ORAs can be estimated through inter-comparison between different ORAs products via multi-reanalysis ensemble approach (See Balmaseda et al. 2015), or through comparison between different ORAs configurations, e.g. reduced analysis resolution, with/without assimilation of some observation types. The ECMWF's ORAP5 ocean reanalysis has been used for assessment of climate signals derived from ECV1.1 sea level product (Zuo et al., 2015), with a series of sensitivity experiments. A recent updated version of ECMWF ORA System 5 (ORAS5 hereafter) with a generic perturbation scheme (Zuo et al., 2017) is used here as the reference for verification of sea level signal as derived from SL_cci products. A few other ORAs from ECMWF with slightly different configurations from ORAS5 (See table 6) were also used here in order to estimate climate signal uncertainties. Assessments of climate signal and its attribution to physical processes from SL_cci ECVs have been carried out, with the focus on temporal evolution of Global Mean Sea Level (GMSL) and regional MSL changes.

1.2.2. Evaluation Methods and data

SL_cci ECV1.1 and ECV2.0 are monthly averaged sea level anomalies (MSLA) maps provided in Cartesian grids at a spatial resolution of quarter of degree. The data has been downloaded and included in the ECMWF data structure from 1993 to 2015. A multi-model approach is used here for the assessment of the climate signals from these ECVs, using a selection of sea level product and ECMWF ORAs (See Table 7). The MSLA maps from all products as listed in Table 6 were interpolated into the same resolution with an optimised land-sea-mask to facilitate inter-comparison between different products. Target resolutions that were used for interpolation include the NEMO ORCA025 and ORCA1 grids (see Barnier et al. 2006) as well as the regular 1x1 degree grid.

The external reference sea level product used here for SL_cci verification is the AVISO DUACS2014 (see Pujol, et al., 2016). This gridded sea level data were produced using Ssalto/Duacs system by processing data from all altimeter missions (SARAL, CryoSat-2, HY-2A, Jason-1&2, T/P, Envisat, GFO, ERS-1 & 2 and Geosat). The reference ocean reanalysis product from ECMWF is the new ORAS5, which is closely related to the ORAP5 system (see Zuo et al., 2014 and Tietsche et al., 2015). ORAS5 is produced using NEMO Ocean Model coupled to LIM2 sea ice model. A series of observation types were assimilated in ORAS5 using NEMOVAR Ocean data assimilation system in its 3DVar FGAT approach. Observations assimilated in ORAS5 include EN4 in-situ profiles, SLA from AVISO DUACS2014, SST from HadSST2 and Sea Ice Concentration from OSTIA. It is worth noting that radar altimetry SLAs were not assimilated in ORAS5 outside of -50°S to 50°N domain, or in any costal region with bathymetry less than 500m. Altimeter-derived GMSL variations were also

assimilated for the satellite era using freshwater constraining in ORAS5 (See Zuo et al. 2015). The operational ORAS5 provides ocean and sea-ice initial conditions for the ECMWF's coupled forecasting system and seasonal forecasting system. Other ECMWF ORAs with slightly altered configurations are ORAS5 without assimilation of SLA (ORAS5-NoAlti) and ORAS5 equivalent low resolution reanalysis (ORAS5-LW) in 1°x1°. Each of these three ORAs also includes 5 ensemble members, generated by a generic perturbation scheme that accounts for representativeness errors from observation, and structure and analysis errors from surface forcing fluxes (Zuo et al., 2017).

Table 7: Summary of MSLA products and ORAs used at ECMWF for evaluation of ECV1.1 and ECV2.0.

Description	Resolution	Assimilation	Period
AVISO		-	1993-2015
ECV1.0		-	1993-2010
ECV1.1	0.25°x0.25°	-	1993-2014
ECV2.0	0.25°x0.25°	-	1993-2015
ORAS5	0.25°x0.25°	SST, SIC, T, S, SLA	1993-2015
ORAS5-NoAlti	0.25°x0.25°	SST, SIC, T, S	1975-2015
ORAS5-LW	1°x1°	SST, SIC, T, S, SLA	1975-2015
CNTL	0.25°x0.25°	-	1975-2015

ECV1.0 is a previous gridded product from ESA SL_CCI; AVISO is the latest DUACS14 MSLA (Mertz et al., 2014). ORAS5 (Zuo et al., 2017) and ORAS5-NoAlti are quarter degree resolution ocean-sea ice reanalyses; ORAS5-LW is the ORAS5 equivalent low resolution (1 degree) reanalysis. CNTL is the ORAS5 equivalent control run without any data assimilation.

1.2.3. Evaluation of Sea Level changes – temporal variations

We computed the time series of GMSL anomaly variations for all products as listed in Table 6. In order to compute the temporal evolution of domain averaged signals, all MSLA maps were firstly interpolated into the same 0.25° by 0.25° grids with an optimized land-sea-mask, then averaged between 60°S and 60°N after removal of the seasonal cycle signal. The trend of GMSL and its inter-annual variations after removing the trend from 2 SL_cci ECVs and 4 other products are shown in Figure 22. The GMSL trends for the total altimetry period are consistent as derived from all 6 products (Figure 22-(top)), with a mean value of 3.0±0.05 mm/yr. The same sea level trend of 2.9 mm/yr were estimated from both ECV1.1 and ECV2.0 (Table 7) during the 1993-2014 period. It is 0.1 mm/yr lower than that as derived from AVISO and ORAS5. When considering the first (1993-2003) and second (2004-2014) altimetry decades, however, GMSL trends from ECV2.0 show -0.3 and +0.4 mm/yr changes relative to ECV1.1, respectively. It is mainly due to the use of new GPD+ wet troposphere correction (Fernades et al., 2016). The mean MSLA trends as estimated from other products (AVISO and three ORAs) is 3.2±0.1 mm/yr and 3.1±0.1 mm/yr, for the first and second altimetry decades, respectively. Verification against AVISO and three ECMWF ORAs suggests that ECV1.1 has under-estimated the GMSL trend for the second altimetry period, by approximately 0.4 mm/yr. Thanks to the new altimeter standards and inclusion of CryoSat-2 and SARAL/AltiKa data, ECV2.0 is much improved during this period.

Inter-annual variations of de-trended GMSLs from these products are shown in Fig. 17-(bottom). Both SL_cci products (ECV1.1 and ECV2.0) are in general consistent with AVISO and three ORAs. For example the dramatic sea level drop during 2011 La Nina event is well represented in all 6 products with similar amplitude. The same for the 1997-1998 El Nino event and sea level rise. However regarding to all other products, a positive offset is apparent from ECV1.1 between 2001 and 2010, a period when uncertainties of SL climate signals are generally high. Close inspection on different sub-domains suggests this offset predominantly comes from Tropical Pacific Ocean and North Atlantic Ocean (not shown). Whether it is due to the different merging algorithms and resolutions of L2 data, or correction schemes, it remains to be seen. Compared to ECV1.1, ECV2.0 shows improved correlation with AVISO and ORAs products. E.g. temporal correlation of de-trended GMSL between SL_cci products and AVISO increases from 0.88 to 0.94 for the 1993-2014 period, for ECV1.1 and ECV2.0, respectively. Improved correlation was also found between ECV2.0 and ensemble mean of the three ORAs, when compared to ECV1.1. Departure between ECV1.1 and AVISO after 2012 could be due to the missing of CryoSat-2 and Saral/AltiKa data when creating L4 gridded product. Consistency between AVISO and three ORAs SL signals suggests that the strong inter-annual variability in the recent years could be underestimated in the current versions of SL CCI product for both ECV1.1 and ECV2.0.

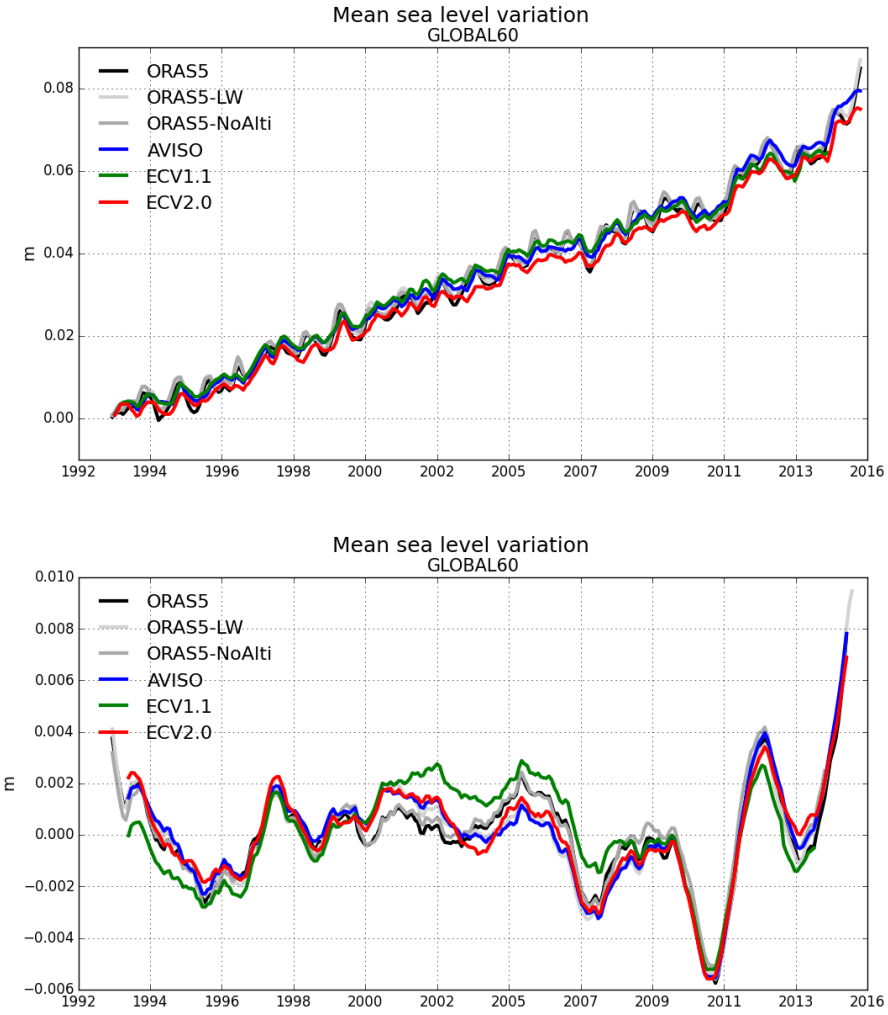

Figure 22: Time series of global (between 60°S and 60°N) mean sea level (top) trend (in m) and (bottom) variance after removing trend. Values are computed using monthly mean data from ocean reanalyses and gridded sea level products, with 3-month (12-month for de-trended) running mean and value from 1993 Jan removed. Glacial isostatic adjustment is not applied here.

Table 8: Global mean sea level trends as estimated from SL_cci ECVs, AVISO and ORAs products

Description	1993-2003	2004-2014	1993-2014
AVISO-DUACS2014	3.3	3.2	3.0
ECV1.0	3.3	-	-
ECV1.1	3.4	2.7	2.9±0.2*
ECV2.0	3.1	3.1	2.9±0.2*
ORAS5	3.1±0.05	3.0±0.01	3.0±0.02**
ORAS5-NoAlti	3.2±0.03	3.0±0.03	3.0±0.01**
ORAS5-LW	3.2±0.02	3.1±0.03	3.0±0.01**
CNTL	2.3±0.16	2.7±0.04	2.4±0.1**

*The uncertainties of ECV1.1 and ECV2.0 GMSL trends were taken from climate indicator data as provided by SL_cci.

**The uncertainties of ECMWF's ORAs were estimated using 5 ensemble members from each ORAs.

Here global domain is defined as between 60°S and 60°N. GIA adjustment (+0.3 mm/yr) was not added in SL_cci ECVs.

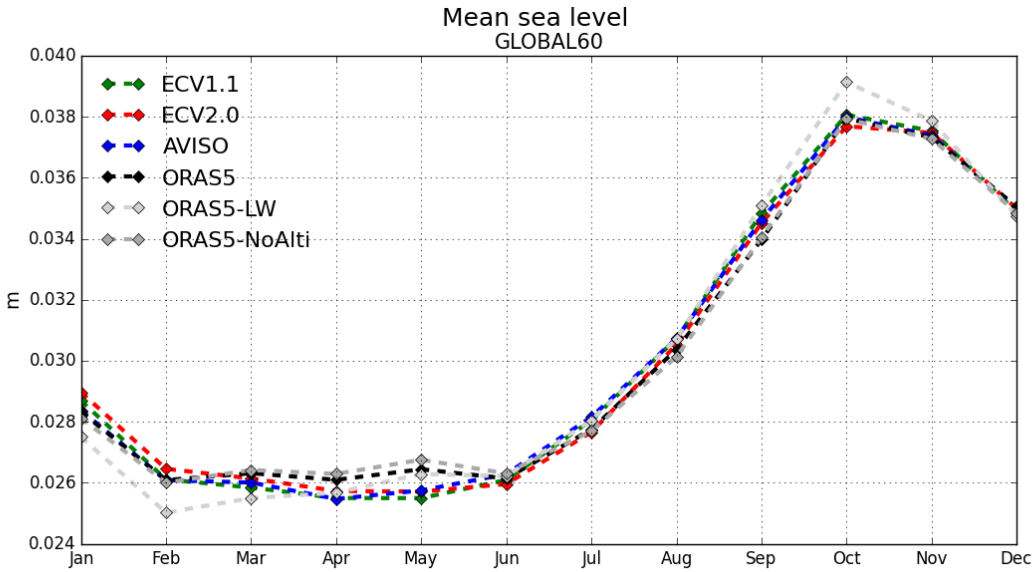

Figure 23: Seasonal cycle (m) of the global (averaged between 60°S and 60°N) MSLAs computed from SL_cci ECVs, AVISO and ORAs during 1993-2014. Mean differences between different products have been removed to facilitate inter-comparisons of seasonal cycle signals.

The seasonal cycles of the global MSLAs were computed for SL_cci ECVs, AVISO and ECMWF ORAs, with the results shown in Figure 23. Amplitudes of two SL_cci ECVs (ECV1.1 and ECV2.0) are very

similar to each other, both with a seasonal low of 2.6 cm at Apr-May, and a seasonal high of 3.8 cm in Oct. The amplitude and phase of seasonal cycle from these two SL_cci ECVs are consistent with AVISO, and fall within the range of uncertainties (except for Jan and May) as estimated by the three ECMWF ORAs. It is also worth noting that the L4 mapped ECV1.1 product suffers from its imperfect land-sea mask, which has been fixed in ECV2.0. This imperfect land-sea-mask is proved to be non-trivial when calculating global MSLA and seasonal cycle signals, and probably accounts for the difference between results shown in Figure 23 here and those in Fig. 5 from the SL_cci Newsletter issue 10.

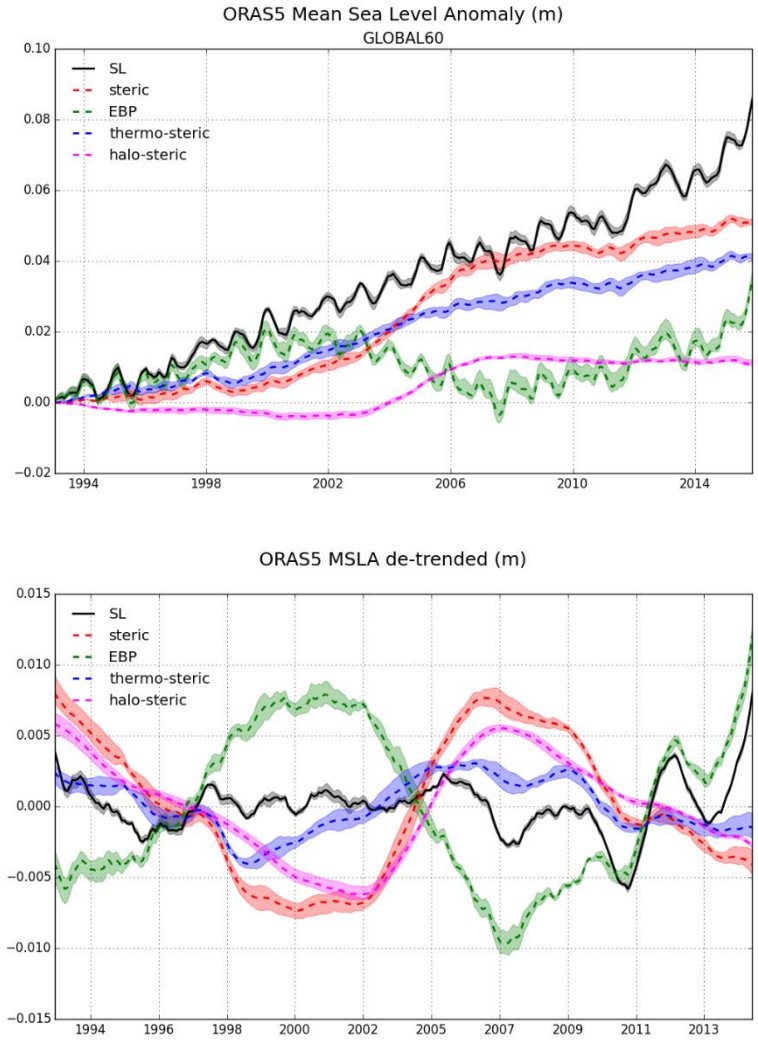

Figure 24: (top) Time series of global (between 60°S and 60°N) mean sea-level trend (m) (solid black line) and its components (dashed lines) for ORAS5 ocean reanalysis; (bottom) same GMSL anomalies with trend removed and calculated using 12-month running mean. Here solid and dashed lines represent ensemble mean while shaded areas encompass the spread of the 5 ensemble members from ORAS5 reanalysis.

Attributions of GMSL variation can be estimated using ocean reanalysis product as ORAS5, following the same decompositions as defined in Zuo et al. (2015). Variation of GMSL anomalies as averaged between 60°S and 60°N and its attributions from ORAS5 are shown in Figure 24 (here EBP=Equivalent Bottom Pressure which account for mass variations in the ocean). The GMSL rising trends in ORAS5 is 3.01±0.02 mm/yr from 1993 to 2014. Figure 24-(top) shows that the ORAS5 GMSL trends is dominated by the thermos-steric changes. The rises of halo-steric changes after 2003 in

ORAS5 are probably due to changes in the observing system after introducing Argo floats. The inter-annual variability of sea level changes from ORAS5 reanalysis (Figure 24-(bottom)) suggests that the GMSL drop in 2007-2008 La Nina event is dominated by the EBP mass changes, while the 2011 prominent GMSL drop is related with both steric height changes and ocean mass variation. Similar results were obtained using ORAS5-NoAlti data (not shown), suggesting that the attributions of GMSL variation as estimated from ORAS5 is not subject to the assimilation of SLA observations.

1.2.4. Evaluation of Sea Level changes – geographic distributions

Here we evaluate the regional MSL changes from SL_cci ECVs. Gridded maps from SL_cci and other reference products were all interpolated into a regular 1°x1° grids before inter-comparison could be carried out. Results of regional MSL trend, variance and its inter-annual variability are discussed as below.

1.2.4.1. Regional MSL differences between ECV1.1 and ECV1.0

Differences in sea level trends (1993-2010) between ECV1.1 and ECV1 are shown in Figure 25. Comparing with ECV1, ECV1.1 shows slightly reduced positive trend in the Indian Ocean and increased positive trend in the tropical eastern Pacific and Gulf of Mexico. Temporal correlation of sea level inter-annual anomalies between ECV1.1 and ECV1 are calculated based on monthly mean sea level data after removal of the seasonal cycle, with the results shown in Figure 26. Correlation between ECV1.1 and ECV1 are very high (>0.98) in most areas except for both polar regions when near the sea-ice edge, and at the equatorial Indian Ocean. The SLA variance between ECV1.1 and ECV1 are very similar, with only small differences at high northern latitudes (Figure 27). Seasonal differences in sea level between ECV1.1 and ECV1 are shown in Figure 28. In general differences between ECV1 and ECV1.1 are small and within range of ±1 mm, with reversed differences pattern between boreal winter (DJF) and summer (JJA). The largest differences can be found by the sea-ice edge regions, probably due to the different coverage of altimetric missions used between these two products. It is also worth noting that the seasonal differences between ECV1.1 and ECV1 are much smaller than that between ECV1 and ECV0 (not shown).

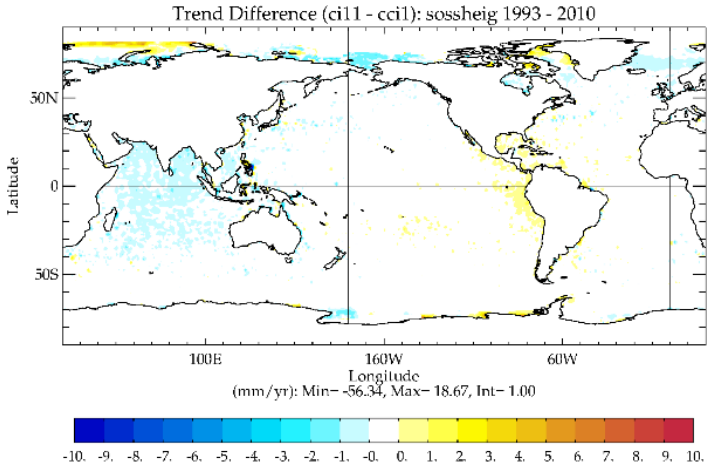

Figure 25: Differences in regional sea level trends (mm/yr) between ECV1.1 and ECV1 during 1993-2010.

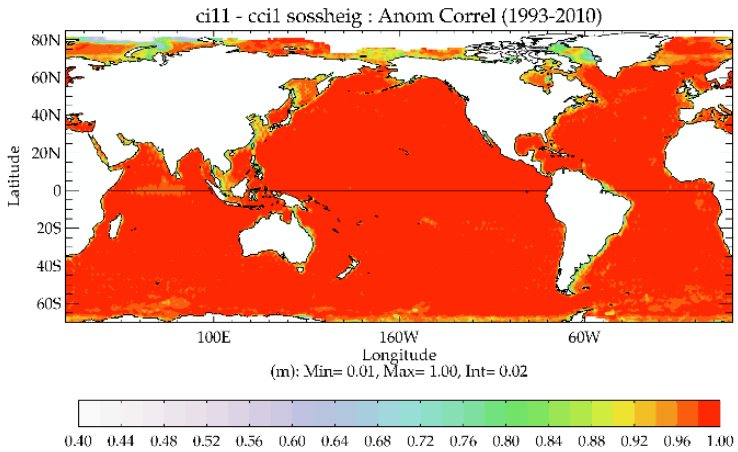

Figure 26: Temporal correlation of regional SLAs between ECV1.1 and ECV1. Statistics are computed after removal of the seasonal signals and for the period 1993-2010. Only values above 0.4 are shown here.

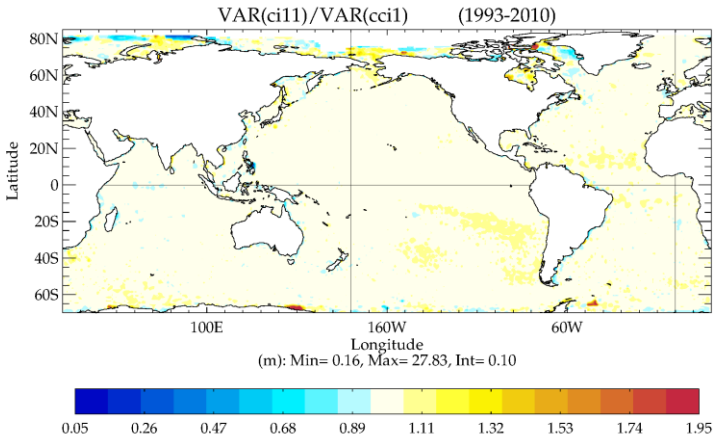

Figure 27: Ratio of variances of the regional SLAs between ECV1.1 and ECV1 during 1993-2010.

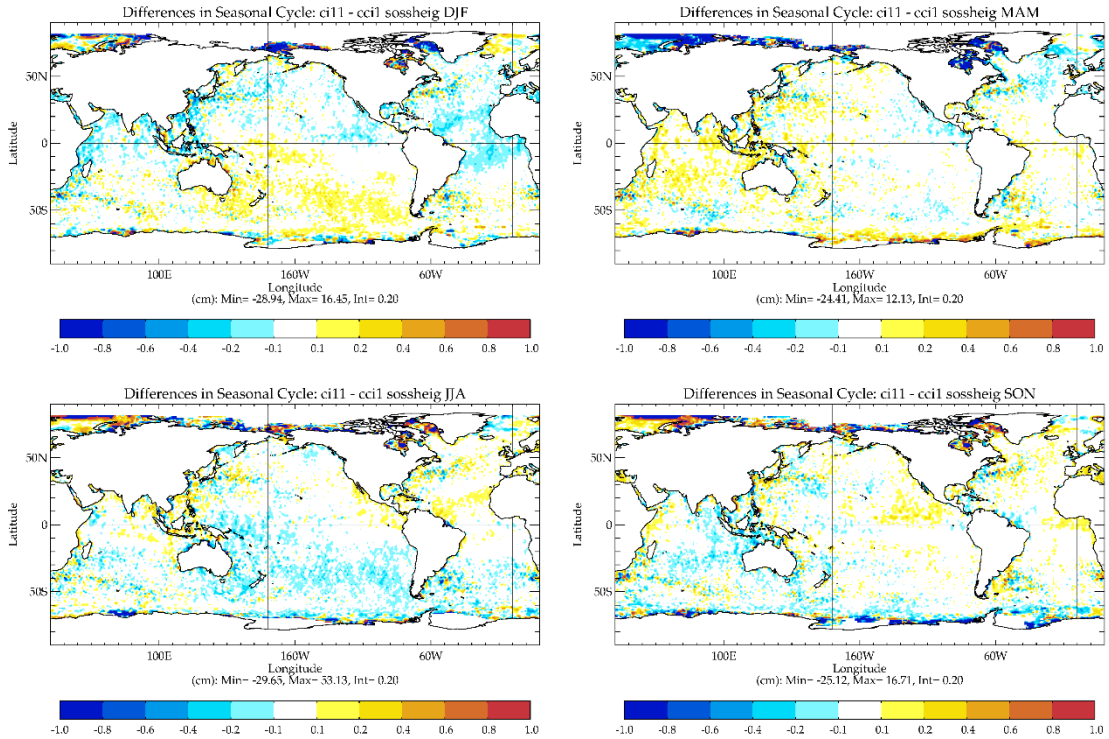

Figure 28: Seasonal differences in sea level between ECV1.1 and ECV1, averaged during 1993-2010. Boreal winter and summer are in the left panel (DJF and JJA, respectively). Boreal spring and autumn are in the right panel (MAM and SON, respectively).

1.2.4.2. Regional MSL differences between ECV2.0 and ECV1.1

Differences in regional MSL trend between the reprocessed ECV2.0 product and ECV1.1 are shown in Figure 29. MSL trend differences as ECV2.0-ECV1.1 range between +/- 1mm/yr, except when at high northern latitudes. The large-scale differences are associated with the new orbit solutions and polar tide correction used in ECV2.0. A general high temporal correlation (>0.95) between ECV2.0 and ECV1.1 (Figure 30) suggests a strong consistency in the inter-annual variability of sea-level. Regions with reduced correlation include Maritime Continental area, the southern Tropics of Atlantic Ocean and tropical Indian Ocean. Relative low correlation (<0.8) is also observed at the high-latitude areas, which is likely associated with the extra data from CryoSat-2 and SARAL/AltiKA in ECV2.0. The SLA variances from ECV2.0 is in general larger than that from ECV1.1 (Figure 31), especially in the Southern Atlantic Ocean. This difference can be explained by a series of update in ECV2.0, including updated sea state bias for Envisat mission; switch to FES2014 ocean tide model and GPD+ wet troposphere correction.

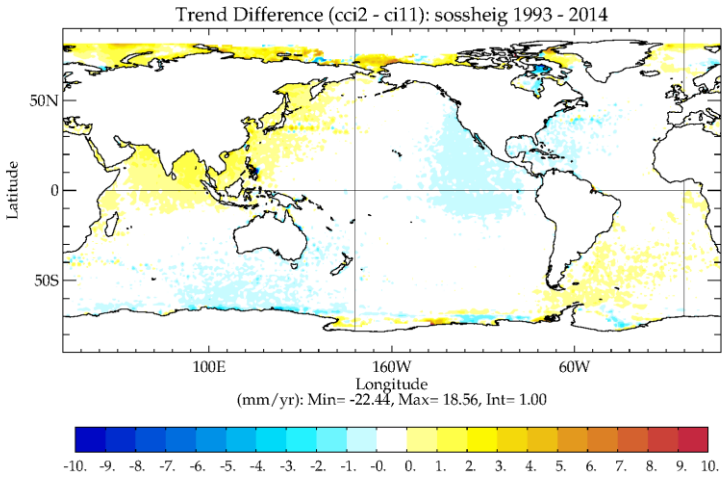

Figure 29: Differences in regional MSL trend (mm/yr) between ECV2.0 and ECV1.1 during 1993-2014.

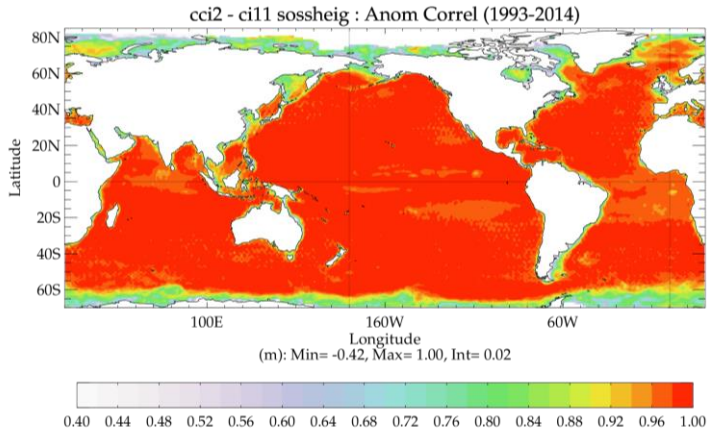

Figure 30: Temporal correlation between ECV2.0 and ECV1.1 SLAs during 1993-2014. Season signals have been removed from SLAs to represent their inter-annual variability, and only value above 0.4 are shown.

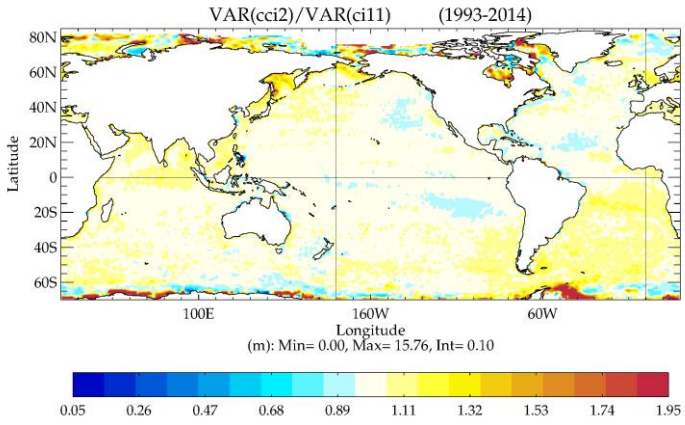

Figure 31: Ratio of variances of the regional SLAs between ECV2.0 and ECV1.1 during 1993-2014.

1.2.4.3. Evaluation regional MSL against AVISO and ECMWF Ocean Reanalyses

Regional MSL changes from SL_cci ECVs were evaluated against the AVISO and Ocean Reanalyses from ECMWF, with results shown in Figure 32. Compared to AVISO, a strong positive trends (~20 mm/yr during 2004-2014) in the Beaufort Sea of Arctic is not included in ECV1.1 due to lack of data coverage (No data behind 70°N after June 2012 in ECV1.1 merged MSLA). ECV2.0 shows improved data coverage in the Arctic regions and more pronounced positive trend in this area, which is consistent with ORAs and AVISO results. Attribution diagnostics from ORAS5 (Figure 33) suggest that this rise is dominated by halo-steric changes in this region due to a strong freshwater build up (Giles, et al., 2012). This positive trend is also visible both in ORAS5 and ORAS5-LW with relatively low uncertainty (±1.5 mm/yr), suggesting a robust climate signal of sea-level rises in the western of Arctic Ocean. Additional ocean reanalysis has been carried out in ECMWF without assimilation of SLA data (ORAS5-NoAlt), while still show similar positive signal in this region. Other large scale differences between ECV1.1 and AVISO exist in the Indian and South Oceans, where we saw ECV1.1 with reduced positive trend by up to 1 mm/year (Figure 32-(left)). Small scale differences at the sea ice edge in the Arctic are mostly likely due to different data coverage between ECV1.1 and AVISO product (Pujol, et al., 2016). Comparing with SL_cci ECVs, ORAS5 shows more pronounced SL trends in the Gulf Stream regions, in the Labrador Sea and at the fronts of the ACC currents. SL change signals in ORAS5-LW clearly lack the complexity in the Southern Ocean and in two Western Boundary Current regions.

Uncertainties of SL trends were computed using ensemble spread from 5 ensemble members of ORAS5 and ORAS5-LW, and were compared with the SL trend errors from SL_cci climate indicators (Figure 32-(right)). It is worth noting that the SL trend uncertainty at ECMWF ORAs is introduced by accounting observation representativeness errors and forcing analysis errors in the ECMWF ocean data assimilation system, while SL trend errors from SL_cci are mainly associated with satellite retrieval algorithms and data processing strategies, e.g. radiometer wet tropospheric correction, orbit error and altimeter parameterization instability (Ablain et al., 2015). It is very interesting to notice that the spatial patterns of large uncertainties are reasonably consistent between SL_cci ECVs and ORAS5, considering that these uncertainties were estimated following very different approaches. Areas with large errors are normally associated with strong meso-scale eddy activities. Moderate SL trend uncertainties (~1.2 mm/yr) were also observed in the Tropical Pacific and Southern Indian Ocean for ECV1.1 and ECV2.0. Compared to SL_cci ECVs, ORAS5 is over-confident on its MSLA changes at most tropical and subtropical regions, but less-confident in the Southern Ocean. It is also worth noting that even with the same ensemble member and configurations, ORAS5-LW underestimated SL trend uncertainties almost everywhere when compared to SL_cci ECVs, suggesting that an eddy-permitting model resolution is necessary if we want to generate a reasonably well ensemble spread of SL changes.

Attributions of SL trends were derived from ORAS5 following the same method as described in Balmaseda et al. (2013), with results shown in Figure 33. Here steric changes include both thermos-steric and halo-steric changes. It is clear that mean SL trends in ORAS5 is dominated by the steric term while the mass variations are only important when considering the coastal regions. One exception is at the Sea of Japan where a strong negative trend (up to 8 mm/yr) due to mass variation was balanced by positive trend from the steric changes. It could be related with our method of constraining the global MSL in ORAS5 (See Zuo et al 2015). The sharp front and reversing SL trends signals in the North Atlantic suggests that the pathway of Gulf Stream extensions maybe misrepresented in ORAS5, which is a common issue in ocean reanalysis. The mass induced positive trend along the east coast of Northern American could lead to excessive pressure gradient and ocean circulation in ORAS5. The strong positive trend in the Arctic Beaufort Sea is almost entirely due to halo-steric changes in ORAS5, which is consistent with the changes of Arctic circulation in the Beaufor Gyre found by NERSC and recent increase of freshwater build up in the Beaufort Gyre (Giles et al., 2012). Uncertainties of SL trends from different attributions as estimated from ORAS5 are shown in Figure 33-(right). By construction the total SL trend uncertainty is not a simple linear combination of attributions trend uncertainties. Nevertheless, information in these maps can still be used as indicator associated with sources of SL trends uncertainties. In general SL trend uncertainties mostly come from uncertainties in temperature variations (Figure 33-right: thermos-steric) except for the Arctic regions, where it comes from uncertainties in salinity variations (Figure 33-right:halo-steric). Salinity also plays an important role in determining SL trend uncertainties in

the North Atlantic Ocean following the extension of Gulf Stream and outflow of the Mediterranean water.

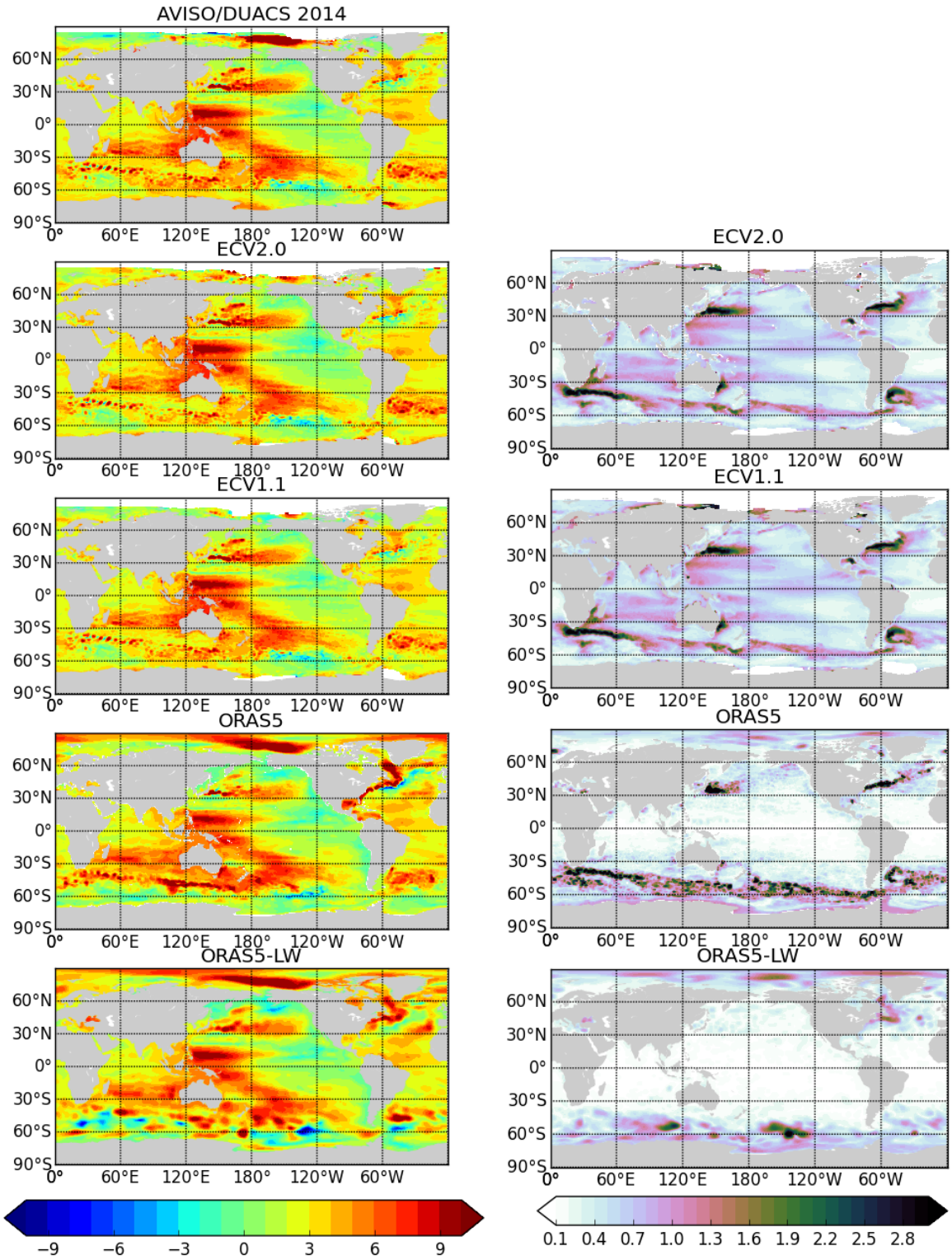

Figure 32: (left) Mean sea-level trends (in mm/yr) and (right) uncertainties from 1993 to 2014 as derived from AVISO/DUACS 2014, ECV2.0, ECV1.1, ORAS5 and ORAS5-LW. MSL trends are calculated using ensemble mean of monthly mean sea level data from ORAS5 and ORAS5-LW. MSL trend uncertainties were calculated as

ensemble spread of MSL trends from ECMWF ORAs, and were provided as climate indicator from SL_cci products.

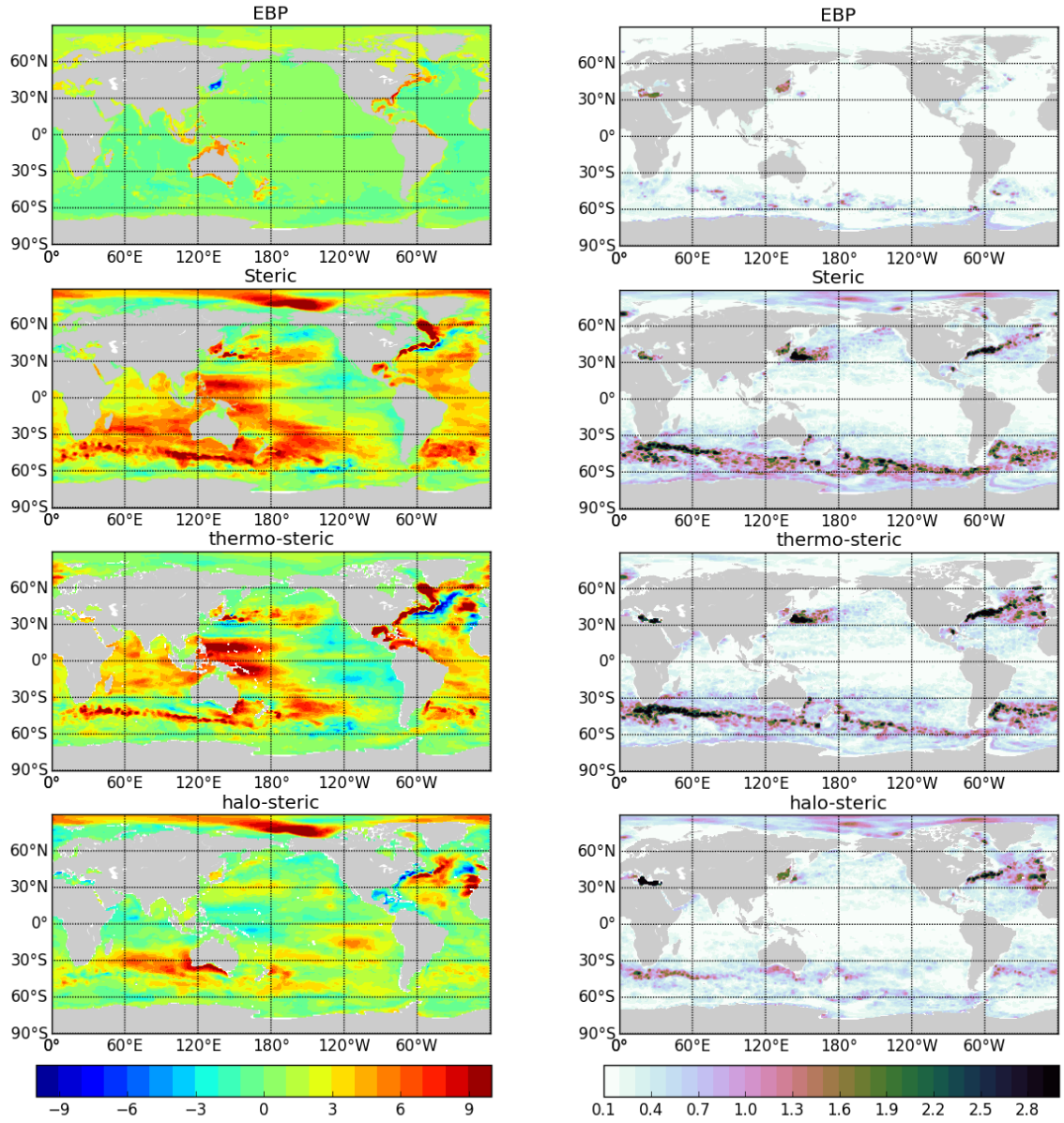

Figure 33: (left) Attributions of mean sea level trends (in mm/yr) and (right) trend uncertainties from 1993 to 2014 as derived from ORAS5 ocean reanalysis. From top to bottom attributions are: EBP mass variations, steric changes, steric changes due to temperature variations, steric changes due to salinity variations. Uncertainties of MSLA trend components are computed as ensemble spread from 5 ensemble members of ORAS5.

Temporal correlation maps between SL_cci ECVs and other dataset (AVISO and ORAs) were computed using monthly mean maps after removal of the seasonal cycle signals, in order to assess the inter-annual variability of the regional MSL changes from SL_cci ECVs. Correlation maps of ECV1.1 and ECV2.0 are shown as the left and right panels in Figure 34, respectively. For ECV1.1, The correlation patterns with AVISO are very similar to that as from ECV0-AVISO correlations (not shown), with minimum value identified along the North Equatorial Counter Current in the Pacific, and at the sea ice edge. The satellite orbits can be identified in the correlation map between

ECV1.1 and AVISO, which is likely associated with different infilling/smoothing methodologies as used in AVISO. Compared to ECV1.1, correlation map between ECV2.0 and AVISO is smoother and without orbit tracks, with slightly reduced correlation in subtropical South Pacific. The same global mean correlation (0.94) with AVISO is obtained from both ECVs. The inter-annual variability of regional MSL changes in ECV2.0 were improved in the north high-latitudes, e.g. at Norwegian Sea and Barents Sea when compared to ECV1.1, verified against both AVISO and three ORAs products (ORAS5, ORAS5-LW and ORAS5-NoAlti). All three ORAs show reduced temporal correlation with SL_cci ECVs, especially for the extra-tropic regions. Areas with low correlation can also be found in the tropic regions, i.e. along the equatorial Tropical Instability Wave (TIW) regions in the Pacific and along the paths of South Equatorial Currents in the Indian Ocean. The lowest correlation has been found between ORAS5-NoAlti and two ECVs. It is expected as SLA data is not assimilated in ORAS5-NoAlti.

We computed the SLA variance during 1993-2014 for ECVs, AVISO and ORAs. Verification of ECVs has been carried out using global mean SLA variance (see Table 9) and ratios of regional variances (see Figure 35) against AVISO and ORAs. Compared to AVISO, the global mean SLA variances increased in ECV1.1 and ECV2.0, by 4% and 10%, respectively. Areas with prominent increased regional SLA variance in ECV1.1 are along the equatorial TIW regions in the Pacific, in the Caribbean Sea and at high-latitudes. Regional SLA variances in ECV2.0 increased further compared to ECV1.1, particularly at the north and south high-latitudes due to additional SARAL/AltiKa data after 2012. In the other hand, all three ORAs show reduced global mean SLA variances compared to AVISO or ECVs. ORAS5 underestimated SLA variance and show a 25% reduction compared to AVISO. Maps of variance ratio with respect to ECVs suggest that ORAS5 have underestimated sea level variances in the subtropics and regions with strong currents. There are areas in ORAS5 with larger sea level variances though, e.g. in the Baffin Bay, Hudson Bay, and most areas in the Southern Ocean. It is also worth noting that high-resolution reanalysis alleviate this problem of underestimation, compared to ORAS5-LW.

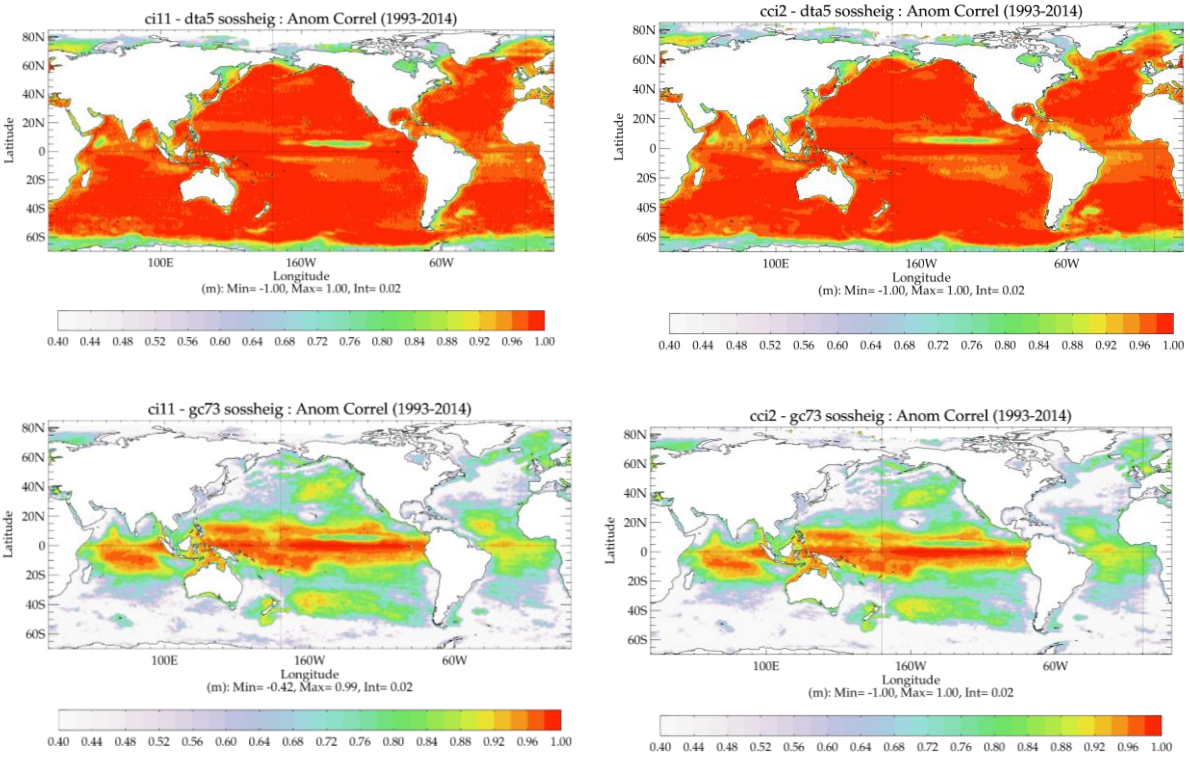

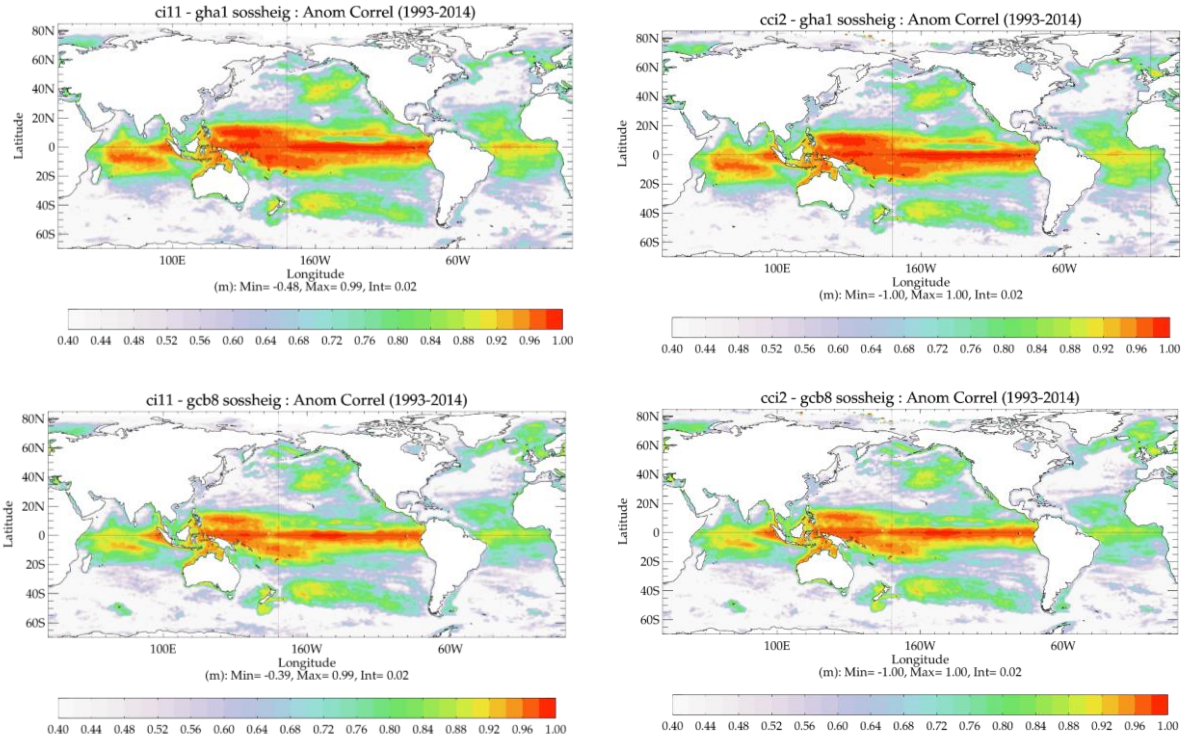

Figure 34: Temporal correlation of (left) ECV1.1 and (right) ECV2.0 with other reference SL products, from top to bottom: AVISO/DUACS 2014, ORAS5 and ORAS5-LW. Statistics are computed with anomalies of monthly mean sea level after removal of the seasonal signals and for the period 1993-2014.

Table 9: Variance of global SLAs from SL_cci ECVs, AVISO and ORAs during 1993-2014.

Products	Mean variance (cm^2)	Changes (ref to AVISO)
AVISO	59.7	-
ECV1.1	61.8	4%
ECV2.0	65.5	10%
ORAS5	45.7	-25%
ORAS5-LW	31.4	-48%
ORAS5-NoAlti	43.9	-27%

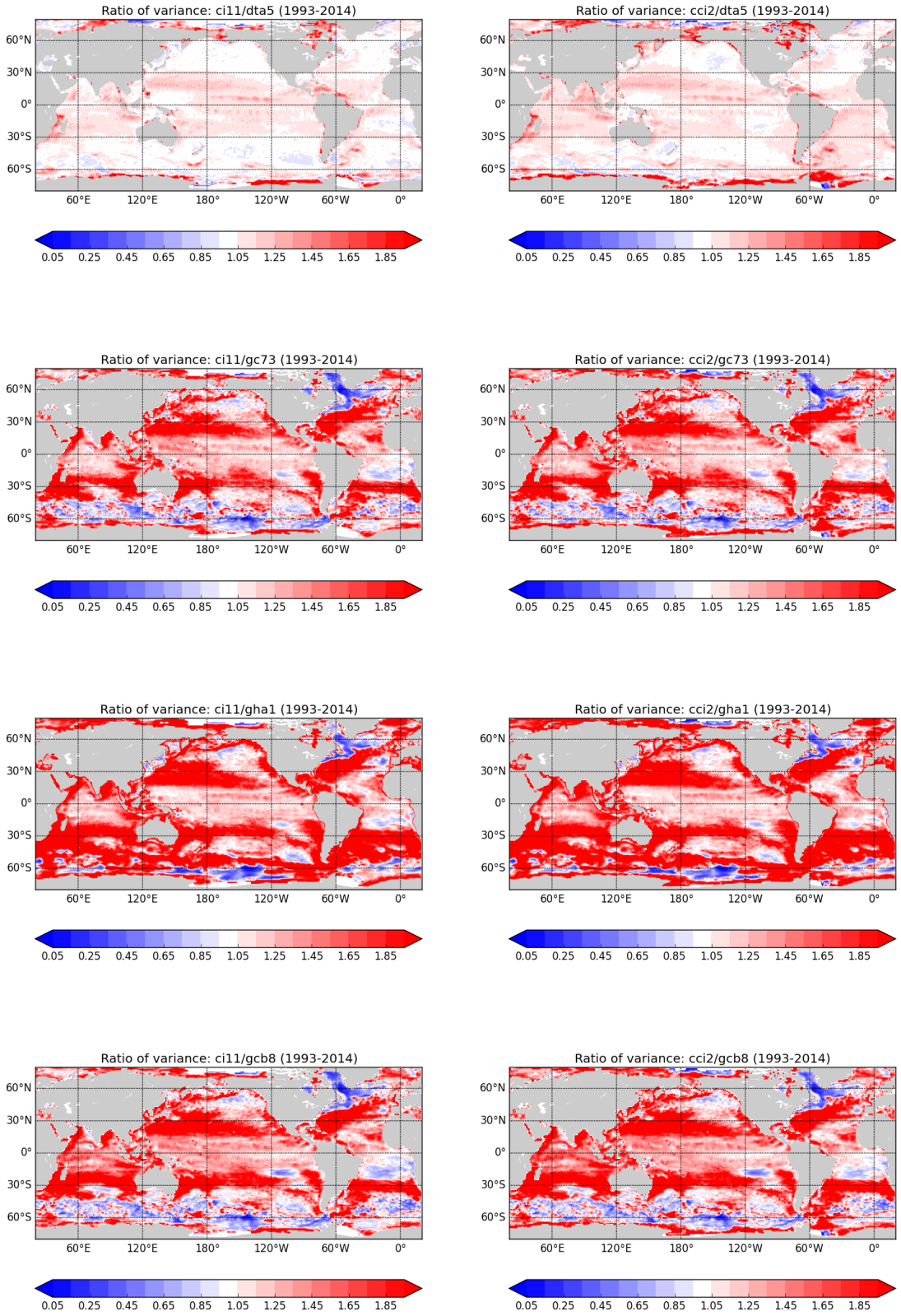

Figure 35: Ratios of regional SLA variance between (left) ECV1.1 and (right) ECV2.0 with other products, from top to bottom: AVISO, ORAS5, ORAS5-LW and ORAS5-NoAlti.

1.2.5. Climate signals as EOF pattern and PC analysis

Empirical Orthogonal Functions (EOF) analysis is a common way to identify major factors and their spatial structures that can account for temporal variability of any climate signals. An EOF analysis has been carried out for MSLAs in the global ocean and Northern Atlantic Ocean for different products as listed in Table 6 (excluding ECV2.0). Discussions of EOF patterns among ECV1.1 and previous SL CCI products (ECV0 and ECV1) as well as ORAP5 reanalysis can be found in the last version of CAR report (SL_CCI-CAR-061). Here we will focus on comparisons of EOF modes for the 1993-2014 period between ECV1.1, AVISO/DUACS 2014, ORAS5 and ORAS5-LW products. This period is chosen because it is common to all the products including ECV1.1.

The first 2 leading global EOF modes as derived from ECV1.1 and other products are shown in Figure 36 as EOF patterns. The first leading SL EOF modes (EOF-1) are very much consistent among all 4 sea level products, which explain ~8 percent of the inter-annual variabilities for both ECV1.1 and AVISO/DUACS 2014. A strong negative-positive sea level pattern can be observed across the Tropical Pacific from west to east, very much resemble the sea level pattern when an ENSO event is present (i.e. El Niño with sea levels dropping in the west and rising in the central and eastern tropical Pacific). EOF-2 in Figure 36 explains ~3 percent of the inter-annual variabilities for both ECV1.1 and AVISO. It corresponds to the reversed sea level pattern during the transition from El Nino to La Nina event and are well represented in all four products (accounts for 6 percent of variance in ORAS5). However it is worth noting that AVISO/DUACS 2014 shows a slightly under-developed positive SL pattern in the west-central tropical Pacific, while ORAS5 shows a positive pattern in the Arctic regions. Other EOF modes have also been investigated (not shown) and it is also worth noting that explained variances from EOF-2 to 4 are not significantly different in ECV1.1 or AVISO products.

Figure 37 shows the time series of Principal Components (PCs) for the first 2 leading EOF modes. The temporal variability of sea level PCs are very robust as shown in these 4 estimations. PC-1 reaches its maximum value in winter 1997, corresponding to the strong 1997 El Niño event. It is followed by the reverse of the tropical Pacific zonal SL gradients during the decay of El Nino and beginning of La Nina (EOF-2, PC-2). A very sharp signal can be identified at PC-3 time series (not shown) between 1997 winter and early 1998, which is consistent with the vast amount of ocean heat released to the atmosphere during the peak phase of the warm event, as well as changes in the meridional distribution. It is interesting to find that among three SLA gridded products, ORAS5-LW shows the highest agreement with ECV1.1 even though AVISO SLA data have been assimilated in this product.

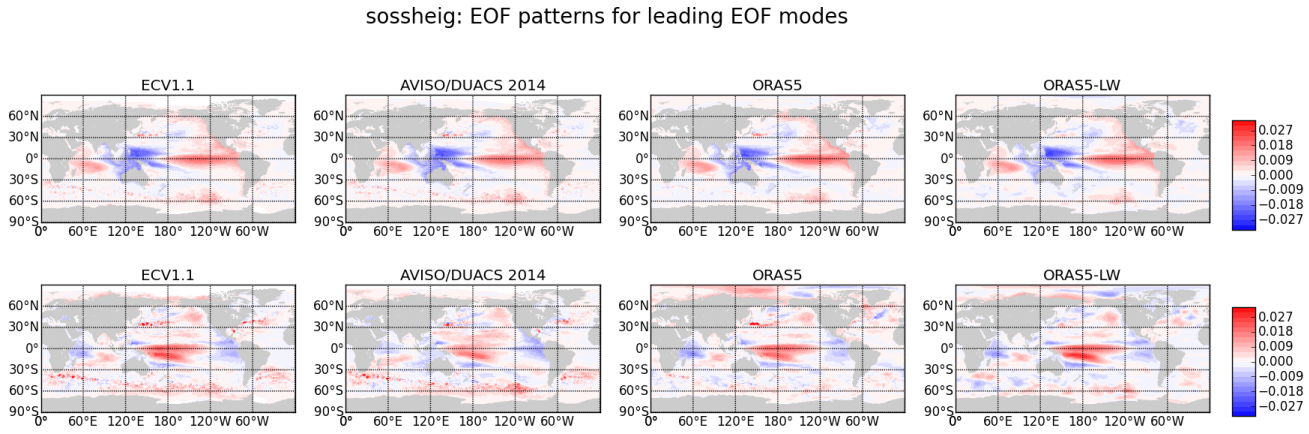

Figure 36: EOF patterns (in m) for the first two leading sea level EOF modes (from top to bottom: EOF-1 to EOF-2) as derived from different sea level products and ocean reanalyses (from left to right: ECV1.1, AVISO, ORAS5 and ORAS5-LW). EOF modes are computed using monthly MSLAs after removal of the seasonal cycle and inter-annual trend signals, and for the period 1993-2014. For ORAS5 and ORAS5-LW MSLAs are taken from ensemble mean.

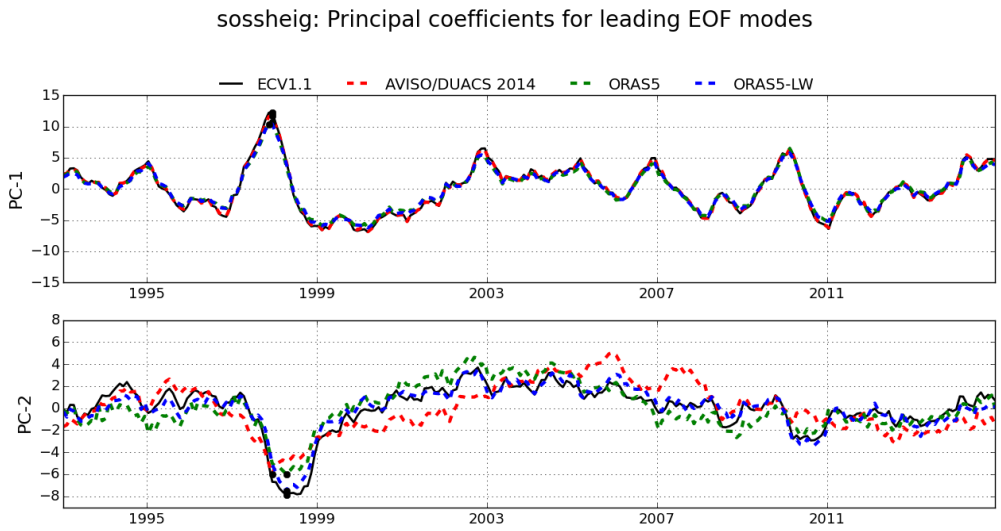

Figure 37: Principal components of the first two leading sea level EOF modes (from top to bottom: PC-1 to PC-2) as derived from 4 sea level products (solid black: ECV1.1, dashed red: AVISO/DUACS 2014, dashed green: ORAS5, dashed blue: ORAS5-LW).

EOF analysis has also been carried out for the above SL products at the North Atlantic Ocean (between -90°W to 40°E, 15°N to 80°N) with the first two leading EOF modes shown in Figure 38:. Here we notice some differences between satellite based products (ECV1.1 and AVISO) and ECMWF reanalyses (ORAS5 and ORAS5-LW). The leading EOF mode in ECV1.1 and AVISO show strong positive SL signals in the Baltic Sea and North Sea, which explain 9.4 and 10 percent of the inter-annual variabilities respectively. However EOF-1 in ORAS5 is dominated by strong positive values in the Labrador Sea and negative values in the north-central North Atlantic, which explains 21.5 percent of the variances. This EOF mode does not appear in ORAS5-LW or ECV1.1. Still the ORAS5 EOF-2 pattern highlights the strong signals in the Baltic Sea and North Sea, which explains 16 percent of the variances and is similar to EOF-1 in ECV1.1 and AVISO. It is therefore considered as a robust signal and is also supported by ORAS5-LW results. Further investigation suggests that this signals in the Baltic Sea and North Sea is associated with mass variations (EBP in Figure 39:) predominantly driven by the zonal wind stress pattern (not shown) in the North Atlantic sub-polar regions. SL EOF-1 in ORAS5 is determined by the steric changes as shown in Figure 39:-(top). And the strong positive value within the Labrador Sea is likely linked with both temperature and salinity variations. Whether it is due to misrepresentation of the mixed layer depth in the Labrador Sea or freshwater export from the Arctic basin, remains to be seen.

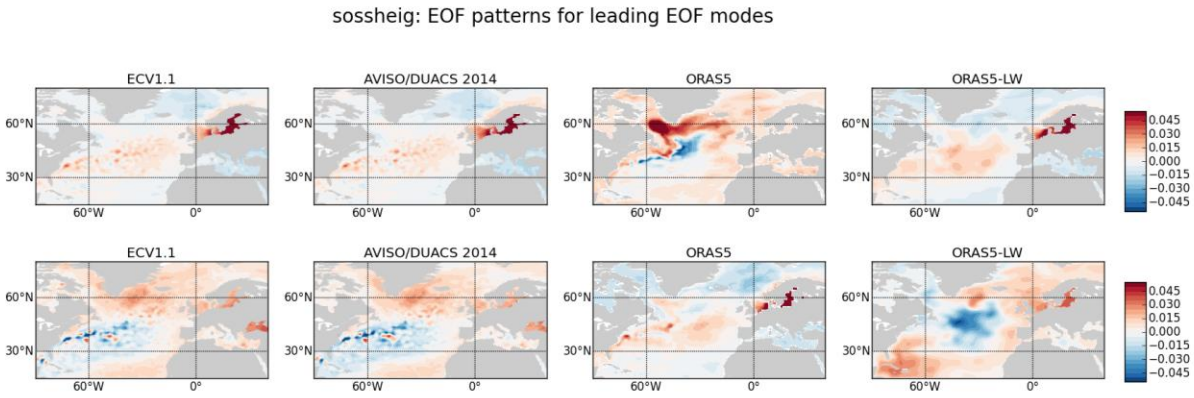

Figure 38: Same as Figure 13 but computed for the North Atlantic Ocean.

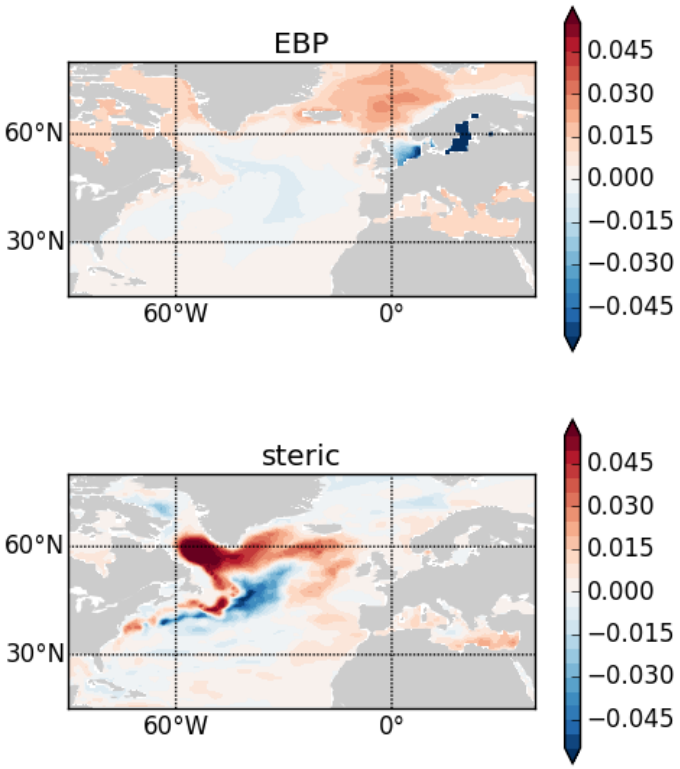

Figure 39: EOF-1 patterns (in m) as derived from ORAS5 SL changes attributions: (top) EBP due to mass variations and (bottom) steric changes due to temperature and salinity variations.

1.2.6. Conclusion and suggestions

The climate signals from the new SL_cci ECVs (ECV1.1 and ECV2.0) have been assessed against ECV1 and AVISO product for the altimetry era (1993-2014). Ocean ReAnalyses from ECMWF with different resolutions/configurations have also been used for evaluation of ECVs following a multi-model approach. Overall climate signals as derived from ECVs MSLA are consistent with AVISO and ECMWF ORAs. Due to reduced data coverage, ECV1.1 has underestimated the sea level rising trend in the Beaufort Gyre. Attribution study from ORAS5 reanalysis suggests that the Beaufort Gyre SL rising is associated with halo-steric contribution from freshwater build up. It has been much improved in ECV2.0 due to inclusive of two additional altimetry data (CryoSat-2 and SARAL/AltiKa). There is a strong agreement in the spatial pattern between the uncertainties of MSL trends in ECVs and ensemble spread of MSL trends in ECMWF ORAs, despite the fact that errors are estimated using very different approach in these two systems. The uncertainties information from SL_cci products provides valuable information of observation errors that could be used for future data assimilation. A robust SL signals in the Baltic Sea and North Sea as identified from the leading EOF pattern for the North Atlantic can be derived from both ECV1.1 and AVISO MSLAs, and is likely associated with the prevailing zonal wind patterns in the North Atlantic sub-polar regions. Temporal variations and geographic distributions of SL trends as derived from ECVs have also been validated against the above products, with additional information of attribution contributions estimated using ECMWF Ocean reanalyses.

Thanks to the new altimeter standards and inclusive of the Saral/AltiKa and CryoSat-2 data, as well as an improved land-sea-mask, the reprocessed ECV2.0 shows many improvements compared to the previous version (ECV1.1), when assessed using AVISO and ECMWF ORAs products.

- Improved GMSL trend, especially for the second altimetry decades (2004-2014).
- Reduced bias in GMSL internal-annual variabilities, particularly for 2000-2010 period.
- Reduced regional MSL trend bias in the northern high latitude regions (e.g. Arctic and subpolar gyres).
- Improved regional MSL internal-annual variabilities for Norwegian Sea and Barents Sea.

Some climate signals derived from ECVs may require further investigations

- GMSL trend derived from both ECVs (3.2 mm/yr) is larger than that from ORAs (3.0 mm/yr) during 1993-2014.
- Both ECV1.1 and 2.0 show enhanced SLA variances (compared to AVISO and all ECMWF ORAs), specially for the high latitudes.

Suggestions for future development and assessment work

1. Errors and Uncertainties
    - Model ensemble approach for assessment of errors and uncertainties in both global scale and regional scales. Model uncertainty was introduced through observation representativeness errors and analysis/structure errors from forcing fluxes.
    - Multi-models approach using both ocean reanalysis and coupled reanalysis products (e.g. CERA-SAT)
    - Exploit the errors and uncertainties from SL_cci+ in the Ocean Data Assimilation system (e.g. specification of OBE in SLA assimilation).
2. Sea-Level in Coastal and high-latitudes areas
    - Validate the SL improvement in the high latitude areas using Ocean Data Assimilation approach. E.g. the prominent regional SL trend signal in the western Arctic Beaufort Gyre.
    - Ocean DA approach for coastal improvements. E.g. ORAS5 currently excludes assimilation of SLA data in any regions with bathymetry less than 500m.
3. Improvement and assessment of altimeter corrections and algorithms at global scale
    - Assessment of the mean state of SLAs against model derived geostrophic circulations
4. Expend SL_cci products
    - Consider to include HY-2A and Sentinel-3 data in the SL_cci product.
    - High temporal resolution (i.e. daily) MSLA fields will be useful for evaluating high frequency signals important for climate, such as the Tropical Instability Waves.

In addition, To assimilate SLA along-track data in Ocean General Circulation Model (OGCM) requires pre-calculation of a model-consistent MDT file every time. This is necessary in order to avoid spurious system drifts when altimetric observations are first introduced into the assimilation system, and could be very expensive when used with high resolution OGCM or a coupled data assimilation system. It would be much more practical to eliminate this step. For instance, it could be interesting to investigate the possibility of using SSH+geoid instead of SLA+MDT. Extension of the

current product to Near Real Time or at least end of 2016 would be useful. It will facilitate the SL_CCI product being used for monitoring and production of the operational ocean reanalyses, and is valuable for evaluation of the latest strong ENSO events.

1.2.7. References

Ablain, M., Cazenave, A., Larnicol, G., Balmaseda, M., Cipollini, P., Faugère, Y., Benveniste, J., 2015. Improved sea level record over the satellite altimetry era (1993–2010) from the Climate Change Initiative project. Ocean Science, 11(1), 67–82. http://doi.org/10.5194/os-11-67-2015

Balmaseda, M. A., Mogensen, K., Weaver A. T., 2013. Evaluation of the ECMWF ocean reanalysis system ORAS4. Q J R Meterol Soc 139(674): 1132-1161

Balmaseda MA, Hernandez F, Storto A, Palmer MD, Alves O, Shi L, Smith GC, Toyoda T, Valdivieso M, Barnier B et al (2015) The Ocean Reanalyses Intercomparison Project (ORA-IP). In: Pro- ceedings of the Institute of Marine Engineering, Science, and Technology, Journal of Operational Oceanography

B. Barnier, G. Madec, T. Penduff, J.-M. Molines, A.-M. Treguier, J. Le Sommer, A. Beckmann, A. Bias- toch, C. B¨oning, J. Dengg, et al. 2006. Impact of partial steps and momentum advection schemes in a global ocean circulation model at eddy-permitting resolution. Ocean Dynamics, 56(5-6):543–567.

Fernandes, M. J. and Lázaro, C., 2016. GPD+wet tropospheric corrections for CryoSat-2 and GFO altimetry missions. Remote Sensing, 8(10). http://doi.org/10.3390/rs8100851

Giles, K., Laxon, S., Ridout, A., Wingham, D., Bacon, S., 2012. Western Arctic Ocean freshwater storage increased by wind-driven spin-up of the Beaufort Gyre. Nature Geoscience, 5 (3) 194 - 197. (2012).

Mertz, F., Pujol, I., Faugere, Y., Maheu, C., 2014. SLTAC Technical Note for new version in April 2014. MyOcean Technical Note.

Mogensen K, Balmaseda MA, Weaver A (2012) The NEMOVAR ocean data assimilation system as implemented in the ECMWF ocean analysis for system 4. ECMWF Tech Memo (668)

Pujol, M.-I., Faugère, Y., Taburet, G., Dupuy, S., Pelloquin, C., Ablain, M., Picot, N. 2016. DUACS DT2014: the new multi-mission altimeter data set reprocessed over 20 years. Ocean Science, 12(5), 1067–1090. http://doi.org/10.5194/os-12-1067-2016

Tietsche, S., Balmaseda, M. A., Zuo, H. and Mogensen, K., 2015. Arctic sea ice in the global eddy-permitting ocean reanalysis ORAP5. Climate Dynamics. http://doi.org/10.1007/s00382-015-2673-3

Zuo, H., Balmaseda, M. A. and Mogensen, K., 2015a. The new eddy-permitting ORAP5 ocean reanalysis: description, evaluation and uncertainties in climate signals. Climate Dynamics, 10.1007/s00382-015-2675-1

Zuo, H., Balmaseda, M. A., and Mogensen, K., 2014. The ECMWF-MyOcean2 eddy-permitting ocean and sea-ice reanalysis ORAP5. Part 1: Implementation. ECMWF Tech Memo (736)

Zuo, H., Balmaseda, M. A. and Mogensen, K., 2015. The new eddy-permitting ORAP5 ocean reanalysis: description, evaluation and uncertainties in climate signals. Climate Dynamics, 10.1007/s00382-015-2675-1

Zuo, H., Balmaseda, M. A., Boisseson, E., Hirahara, S., 2017. A new ensemble generation scheme for ocean analysis. ECMWF Tech Memo (795)

1.3. WP5130: Assessment in the Arctic Ocean using a multi-ECV approach (NERSC)

1.3.1. Introduction

The ocean circulation in the high latitude seas and Arctic Ocean is depicted in Figure 40. In general, it can be characterized by four regional circulation regimes and cross-regional exchanges and volume transports, namely the Northeast Atlantic, the Labrador Sea and Canadian archipelago, the Nordic and Barents Seas and the Arctic Ocean. At scales of about 100 km and more the connection between these mean circulation regimes and the mean sea surface (MSS) height is determined by the mean dynamic topography (MDT) referenced to a geoid (G) (e.g. MDT = MSS - G). Under the assumption that the geoid is time invariant the changes in the sea level will thus be balanced by a change in the MDT. As such, the observed sea level changes which is presented and discussed in this Climate Assessment Report will also impact the large scale ocean circulation.

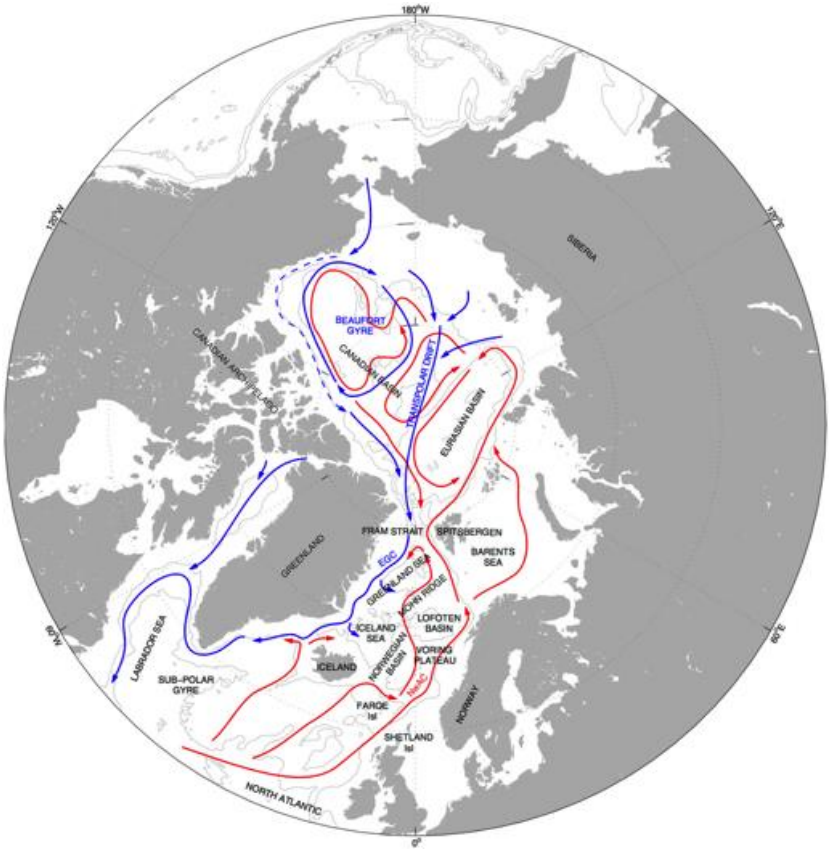

Figure 40: The general circulation of the Arctic Ocean, Nordic Seas, and North Atlantic. Bottom contours are 1000 and 3000 m outlining the shelves and basins. Red arrows represent Atlantic Waters, which reside in the surface in the Nordic Seas and submerged in the Arctic Ocean, while blue arrows represent fresh surface Polar Water (Johannessen et al., 2014).

The work builds on the findings and achievements provided in SLCC-CAR-061-1-3 (September 2016) that assessed the V1 sea level fields and involves the use of the simulation runs with the Norwegian Earth System Model (NorESM) that has been delivered to CMIP5. In addition, results from a coupled climate model assimilation experiment are reported. The TOPAZ re-analyses are also used for the inter-comparison and assessment. Emphasis is given to:

- inter-comparison of thermosteric and halosteric anomalies in the in-situ observations and in the NorESM simulation and TOPAZ4 reanalyses for the high latitude seas (e.g. Norwegian-Greenland-Iceland- Barents Seas) and assess their contribution to the sea surface height anomalies;
- inter-comparison of sea level change from observations, the coupled climate model NorESM and the operational model TOPAZ4 with assimilation;
- using the coupled global climate model NorCPM (Norwegian Climate Prediction Model) with assimilation of SST for assessing sea level change in the Sub-Polar gyre.

1.3.2. Used dataset

An overview of the available hydrography data and the model runs with and without assimilation is provided in Table 10 and specify the time period, the spatial resolution, the choice of ocean models and the forcing.

Data and Models	Time Period	Resolution	Ocean Model	w/wo assimilation	Forcing
ESA CCI_SL	1993-2015	~ 50 km			
CORA	1993-2014	Gridded to ~ 150 km			
NANSHY data	1950-2015	Gridded to 100 km and annual			
TOPAZ4	1993-2016	11-14 km	HYCOM	With SST, SSH, Argo, sea ice	ECMWF
NorESM	1993-2016	100 km	MICOM	without	NCEP
NorCPM	1950-2012	100 km	MICOM	With SST	NCEP

Table 10: Overview of data and model runs (with and without assimilation) used in the study.

The in-situ data (Figure 41) are from the NANSHY database (Nilsen, 2016) and the CORA climatology (Cabanes et al., 2013). The TOPAZ4 reanalyses fields assimilating these data are used together with the simulation runs from the Norwegian Earth System Model (NorESM) that delivered to CMIP5. In addition, the sea surface temperature has been assimilated in a NorESM reanalyses and prediction (NorCMP) experiment with particular focus on the Sub-Polar Gyre.

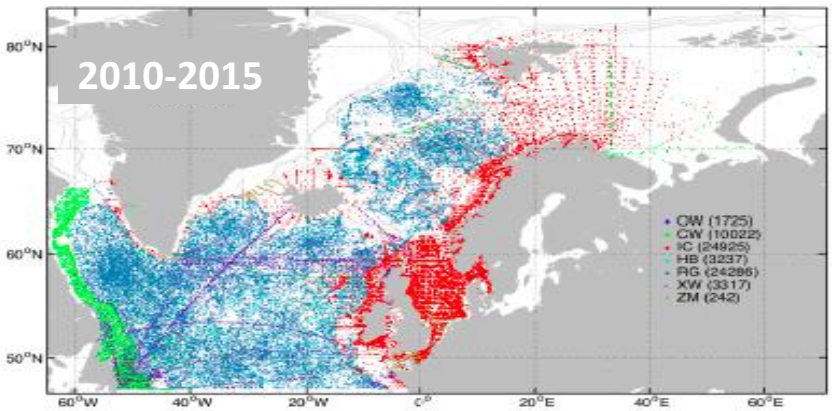

Figure 41: Spatial coverage of the in-situ data from 2010-2015. The dominance of the Argo profiling floats is represented by the blue colour.

The main results of the assessment of the altimeter derived sea level change (SL_ECV_V2) for the high latitude seas and Arctic Ocean are presented and discussed below using this combined in-situ hydrography and model simulation dataset.

1.3.3. Assessment of the total sea level trend

The trend in the altimeter-based sea level change (CCI_SL V2) for the high latitude seas and Arctic Ocean is shown in Figure 42. Distinct signals of a sea level rise of up to 7 mm/yr is found in the Beaufort Gyre and up to 4-5 mm/yr in the Sub-Polar Gyre, while the Lofoten Basin in the Norwegian Sea displays a rise of around 4 mm/yr. The northern wall of the Gulf Stream extension is moreover displaying regions of positive and negative sea level trends. There is also evidence of a weak sea level decline in the Northeast Atlantic south-southwest of Iceland, in the Labrador Sea, around Svalbard and spot-wise on the Siberian shelf. A large region of weak decline in sea level is also encountered in the Northeast Pacific. The latter region is not further addressed in this report.

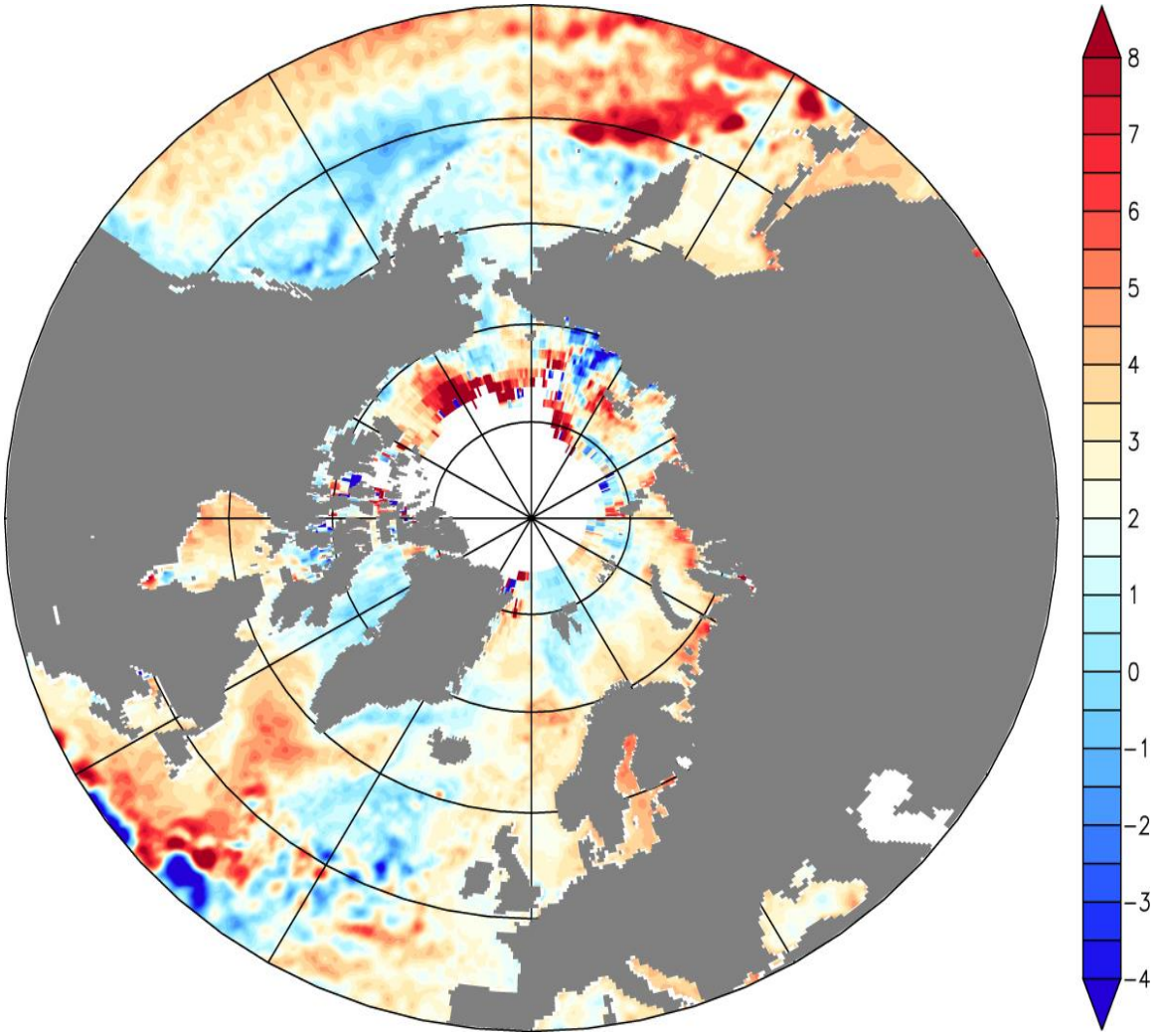

Figure 42: Sea level change in mm/yr for the period 1993-2015 for the ESA_CCI SL_ECV_V2. The lack of coverage (white area) in the Arctic Ocean north of 82° N is due to presence and influence of the sea ice field.

In comparison to the ESA CCI_SL V2 trends the TOPAZ4 sea surface height trends shown in Figure 43 display more distinct regional structures of sea level rise and decline, notably in the Amerasian basin of the Arctic Ocean and in the northern North Atlantic. A positive trend of about 6-7 mm/yr is

found in the Beaufort Gyre but appears to extend over a very large area towards the Siberian Shelf which is not evident in the ESA CCI_SL V2 dataset. The presence of a positive trend of about 5-6 mm/yr in the Sub-Polar Gyre is also found. However, the negative trend in the western part of the Sub-Polar Gyre is not in agreement with the CCI_SL V2 trend.

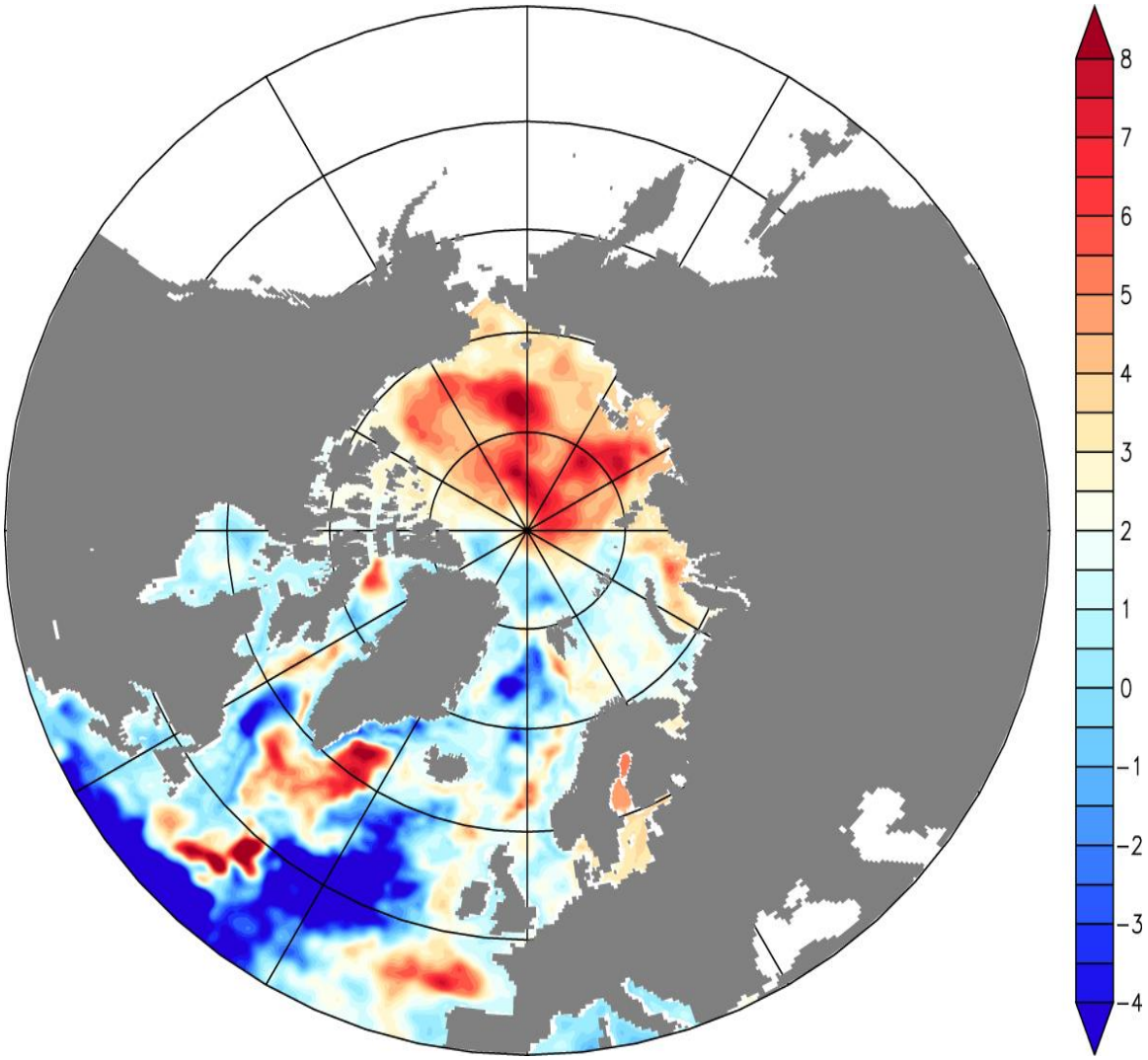

Figure 43: Sea level change in mm/yr for the period 1993-2016 from the TOPAZ4 re-analyses fields.

In the Nordic Seas and the Lofoten Basin, on the other hand, regions of both positive and negative trends stand out in contrast to the more gentle sea level rise expressed in the CCI_SL V2 dataset. Moreover, the large and distinct region of strong decline in the sea level of up to 3-4 mm/yr encountered in the North Atlantic is not found in the CCI_SL V2 dataset which only give a very weak decline of around 1 mm/yr.

In Figure 44 the sea level trend from the coupled climate model NorESM is shown for comparison to the observed (ESA CCI-SL V2) trend and the trend derived from the TOPAZ4 reanalyses. Differences are clearly present. Notably, there is no expression of the Beaufort Gyre, while the Sub-Polar Gyre shows a weak rise of 3-4 mm/yr bounded by a distinct positive (7 mm/yr) - negative (> 4 mm/yr) trend southwest of Iceland. Moreover, the trends in the Nordic Seas and the Lofoten Basin display fairly weak rise and decline around ± 1 mm/yr with spatial structures that are not found the in the CCI_SL V2 dataset and in the reanalyses with TOPAZ4. The latter has notably assimilated both altimetry data and hydrography data, while the NorESM simulation is the ensemble mean over several realization without assimilation.

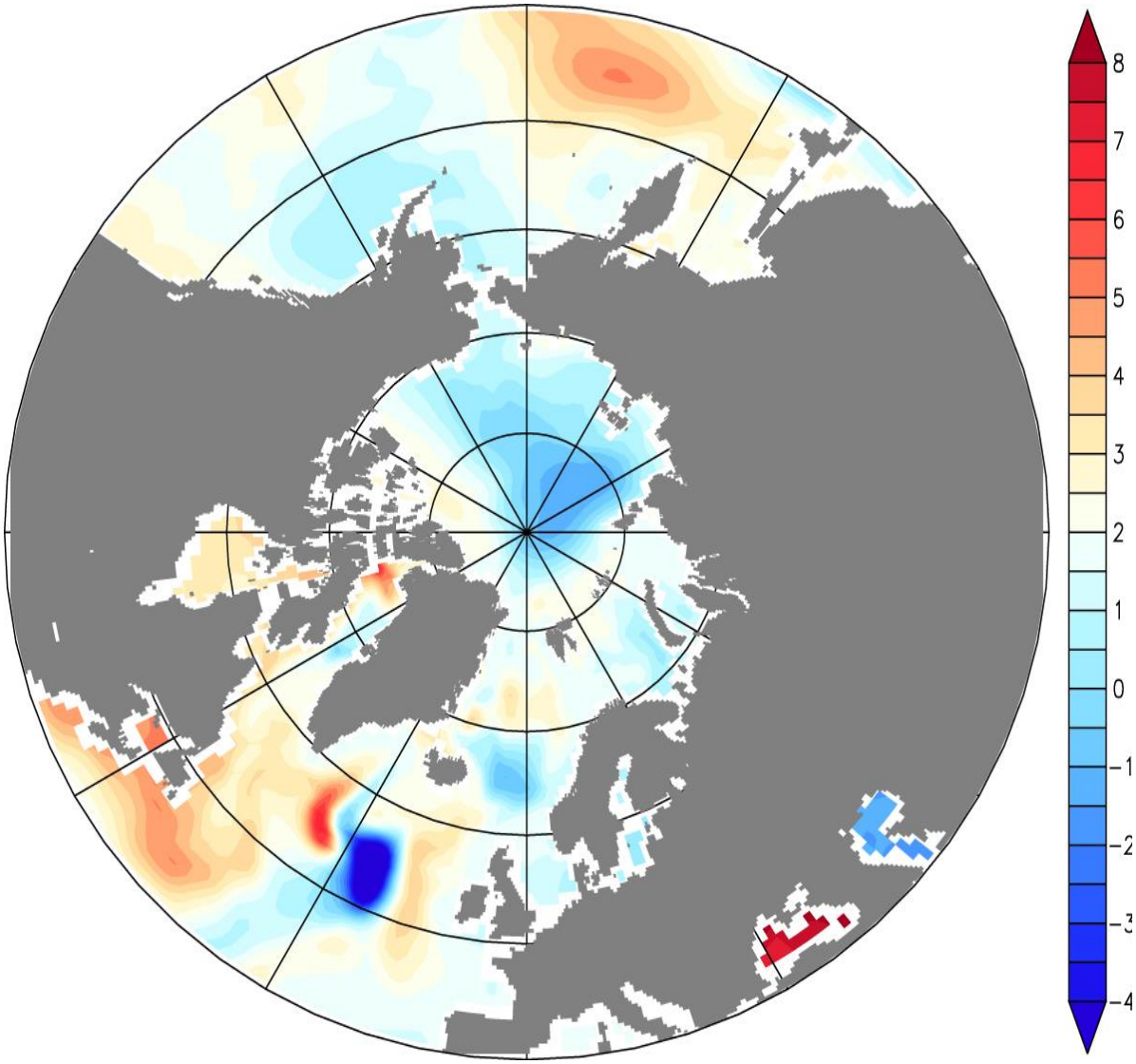

Figure 44: Sea level change in mm/yr for the period 1993-2016 from coupled climate model NorESM.

The sea level change respectively for the Arctic Ocean, the Sub-Polar Gyre and the Lofoten Basin are displayed in Figure 45. In Figure 45 (top) both the TOPAZ reanalyses and TOPAZ free run simulations are shown together with the data from the GLOBAL-REANALYSES-PHYS products derived from the MyOcean Global Monitoring and Forecasting Centre (Jiping et al., 2013). The seasonal signal has a low amplitude reaching up to about 10 cm in the observations and being slightly smaller around 5-7 cm in the reanalyses and simulations. There are seemingly no major improvements for the reanalyses. All the seasonal signals also display erratic variability. The overall trend in the sea level rise, both the observations and the model fields, is about 2 mm/year. The NorESM fields are not included in this comparison as the apparent trend disagreed entirely. Note also that these seasonal signals and their trends are related to the sizes of the areas selected for the estimations.

In the Sub-Polar Gyre (Figure 45, middle) the comparison shows smoother seasonal variability with comparable amplitudes between the model fields and the observations ranging from around 5-7 cm. Moreover, a comparable trend of just below 3 mm/yr is found for the observations and the NorESM simulation, while it is slightly less for the TOPAZ reanalyses. This probably results from the fact that the selected area covers the region of negative trend in the western domain of the Sub-Polar Gyre displayed in Figure 43. The comparison for the Lofton Basin (Figure 45, lower) shows that the seasonal signals are slightly larger (> 10 cm). The trend in the CCI_SL V2 observations is about 3

mm/yr while the model fields only give a trend of about 1.5-2 mm/yr. In comparison, the seasonal variability and trend in the altimeter observation-based DTU field are in fairly good agreement with the CCI_SL observations. Again the differences result from the spatial pattern of the trend in the sea level rise which is less extended in the model fields compared to the observations as noted in Figure 43 and Figure 44.

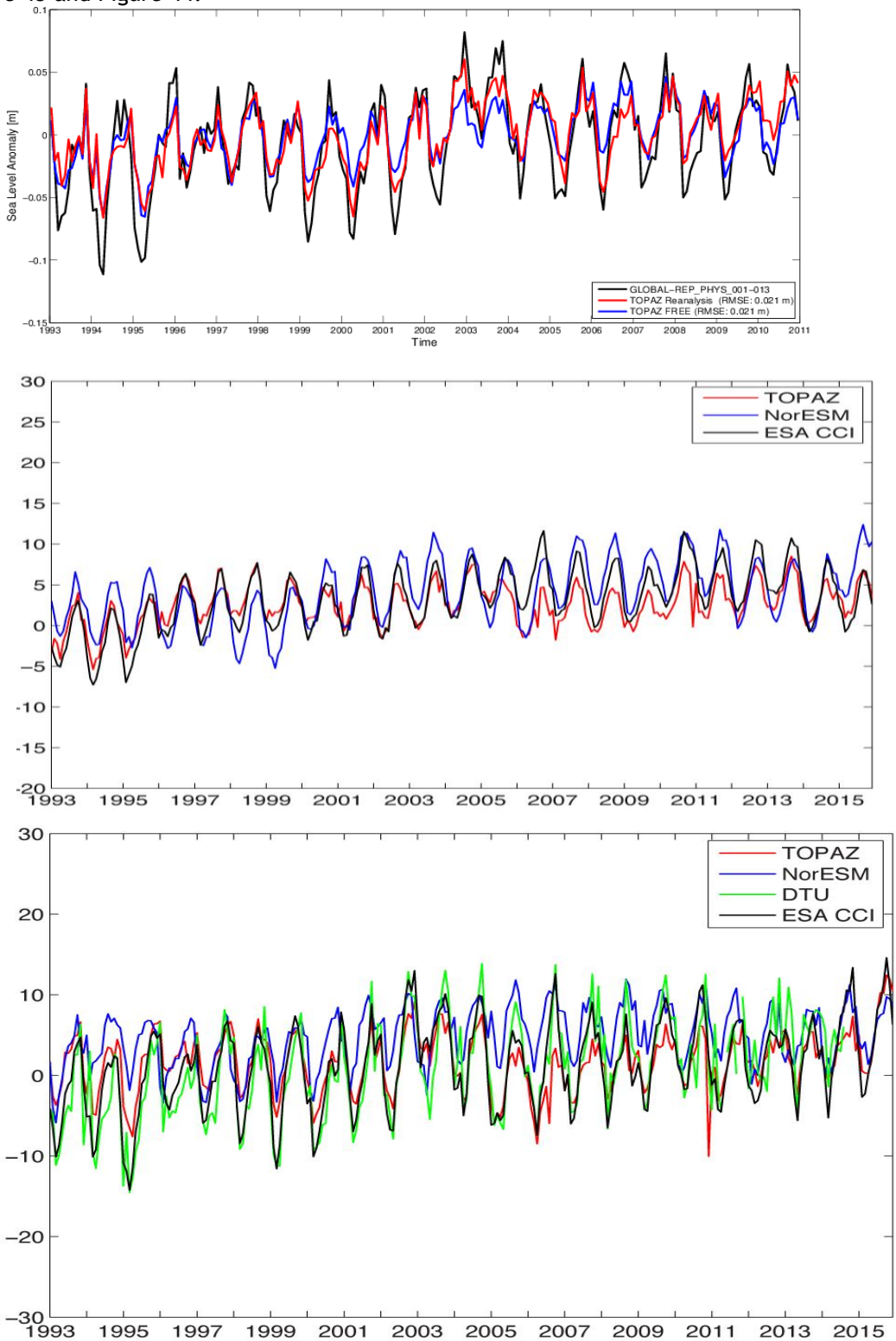

Figure 45: Seasonal to annual change in sea level in mm/yr for the period 1993-2016 for (top) the Arctic Ocean (only to 2011), (middle) the Sub-Polar Gyre, and (lower) the Lofoten Basin. Vertical axis is in m (top) and cm (middle and lower).

1.3.4. Assessment of the steric contribution

In order to examine the steric contribution to the sea level change and trends the hydrography derived from respectively the TOPAZ4 reanalyses and the coupled climate NorESM simulations are used. In Figure 46 the TOPAZ4 reanalyses fields are shown for the thermosteric and halosteric trends (upper) and the steric and total trends (lower). One immediately recognizes that the thermosteric trend has minor influence on the steric and total trends in the Beaufort gyre. In contrast the positive trend in the sea level rise appears to fully emerge from the halosteric trend except on the Siberian Shelf where the trend must be connected with the bottom pressure and hence related to water mass accumulation on the shelf. The apparent freshening of the Beaufort Gyre is consistent with findings reported by Morison et al. (2012) who proposed that this occurred as a result of persistent changes in the pathways of Arctic freshwater.

Looking at the Sub-Polar Gyre and the Lofoten Basin, on the other hand, one finds that the key contribution to the positive trends in steric and total signals emerge from the thermosteric trends. This is assumed to be related to an increased occupation by warm Atlantic water. This is further supported by the evidence of corresponding negative halosteric trends which would be expected provided the source is the warm and saline water emerging from the Gulf Stream.

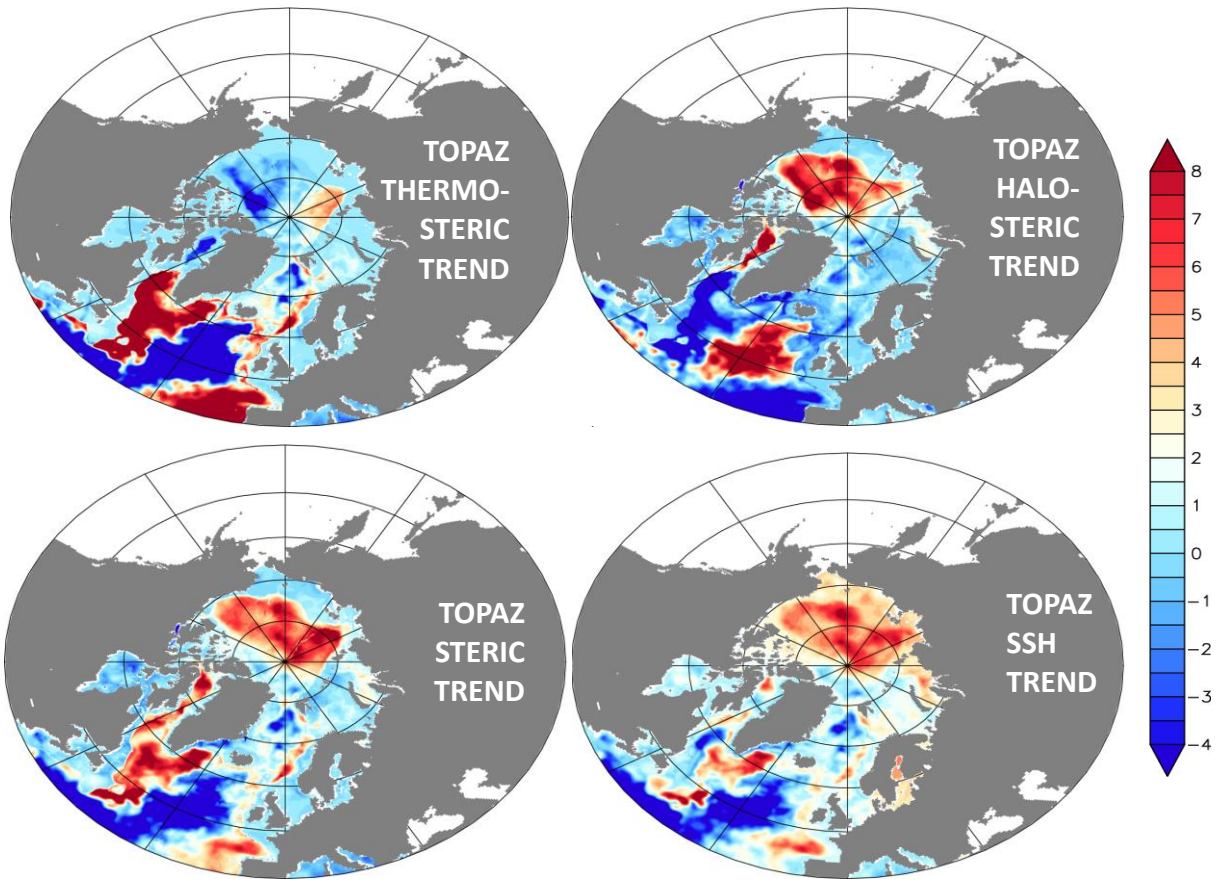

Figure 46: Contribution to the sea level trend (mm/yr) from TOPAS4 reanalyses for the period 1993-2016 for (top left) the thermosteric contribution, (top right) the halosteric contribution, (lower, left) the total steric trend, and (lower right) the total trend for the ESA CCI_SL V2 data.

In Figure 47 the corresponding results from the NorESM simulations of the thermosteric and halosteric trends (upper) are shown together with the total steric trend and total sea level trend (lower). The slight sea level rise along the Canadian shelves of the Beaufort Gyre originates from the halosteric trend. In the Sub-Polar Gyre the positive trend in sea level rise is partly from the thermosteric contribution and partly from the bottom pressure, hence barotropic source. Moreover the distinct positive-negative sea level trends along the eastern boundary of the gyre seem to arise from the thermosteric contribution to the trend. Finally, in the Lofoten Basin the moderate trend in sea level rise appears to arise from the thermosteric contribution perhaps associated with longer residence time of water Atlantic Water. The corresponding negative halosteric trend associated with higher salinity of this Atlantic Water support this assumption.

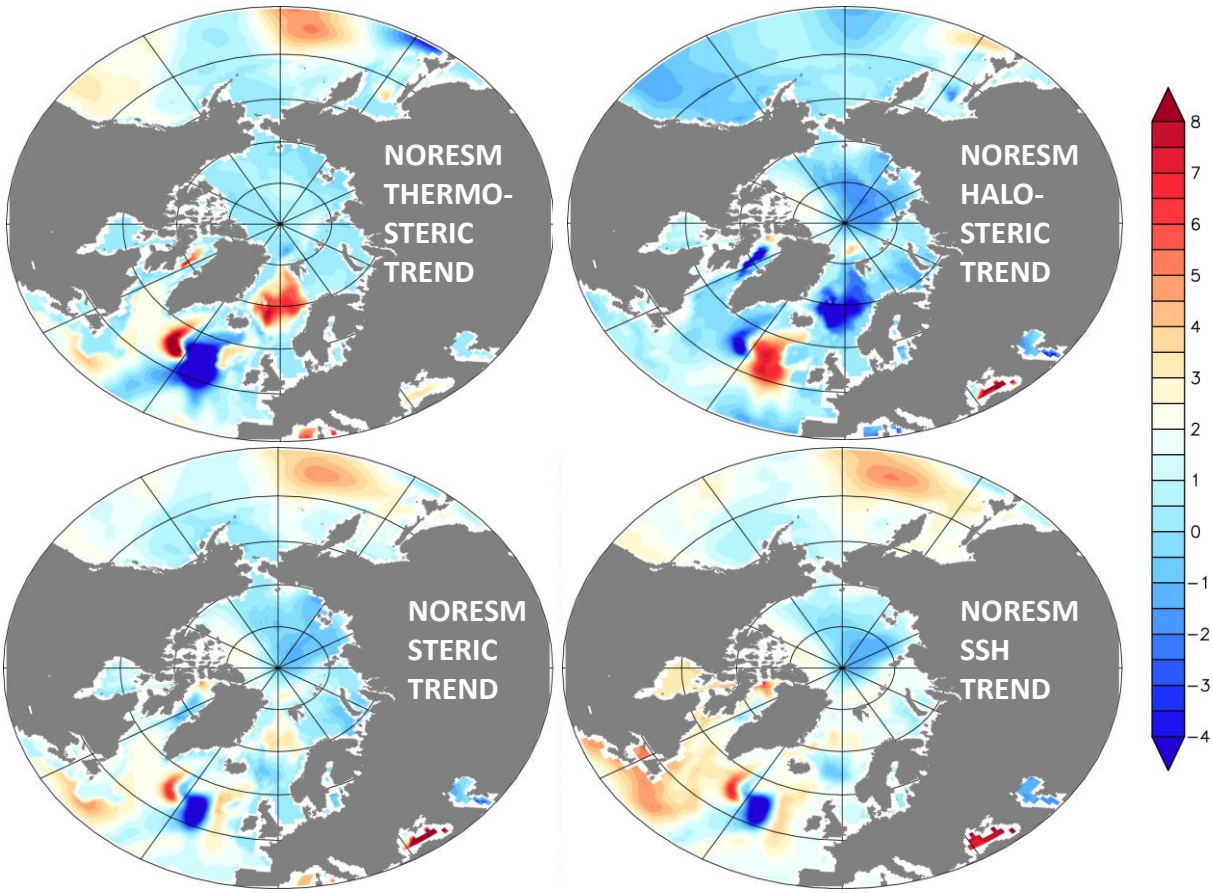

Figure 47: Contribution to the sea level trend (mm/yr) from NorESM simulations for the period 1993-2016 for (top left) the thermosteric contribution, (top right) the halosteric contribution, (lower, left) the total steric trend, and (lower right) the total trend for the ESA CCI_SL V2 data.

The steric (thermo-, halo-) trends observed in the sea level in the Sub-Polar Gyre have also been discussed by Hatun et al., (2005). They presumed that the variable dynamics of the Sub-Polar Gyre controlled the respective inflows of either cold/fresh sub-polar waters or warm/salty subtropical waters from the Gulf Stream and its extension into the North Atlantic Current (NAC). Using salinity criteria to identify the respective sources of the water masses, they showed opposing transport variability of both source waters. Evidently, this closely mimicked a strong SPG when the cold/fresh water transport is strong and vice versa a weak SPG circulation when the warm/saline water transports dominates the inflow to the gyre. In consistence with the findings presented here, it is therefore likely to conclude that a weakening of the anticlockwise circulation has occurred in the Sub-Polar Gyre during the last 20-25 years. In contrast the distinct sea level rise encountered in the

Beaufort Gyre during the same period has lead to an intensification of the clockwise circulation in the gyre that may stimulate more trapping of fresh and cold Arctic surface water.

In Figure 48 the corresponding thermosteric, halosteric and steric contributions to the sea level trends are shown based on the CORA hydroraphic data (Cabanes et al., 2013) for the time period 1993-2014. The positive steric trend in the Beaufort Gyre is clearly dominated by the halosteric trend in agreement with the TOPAZ4 reanalysis fields although the details in the spatial structure are somewhat different. In the Sub-Polar Gyre, moreover, the thermosteric contribution to the positive trend dominates as was also found in the TOPAZ4 fields while it was less clearly found in the NorESM simulations. For the Lofoten Basin the in-situ observations again suggest that the thermosteric trend dominates the steric trend in agreement with the the reanalysis and the model simulations.

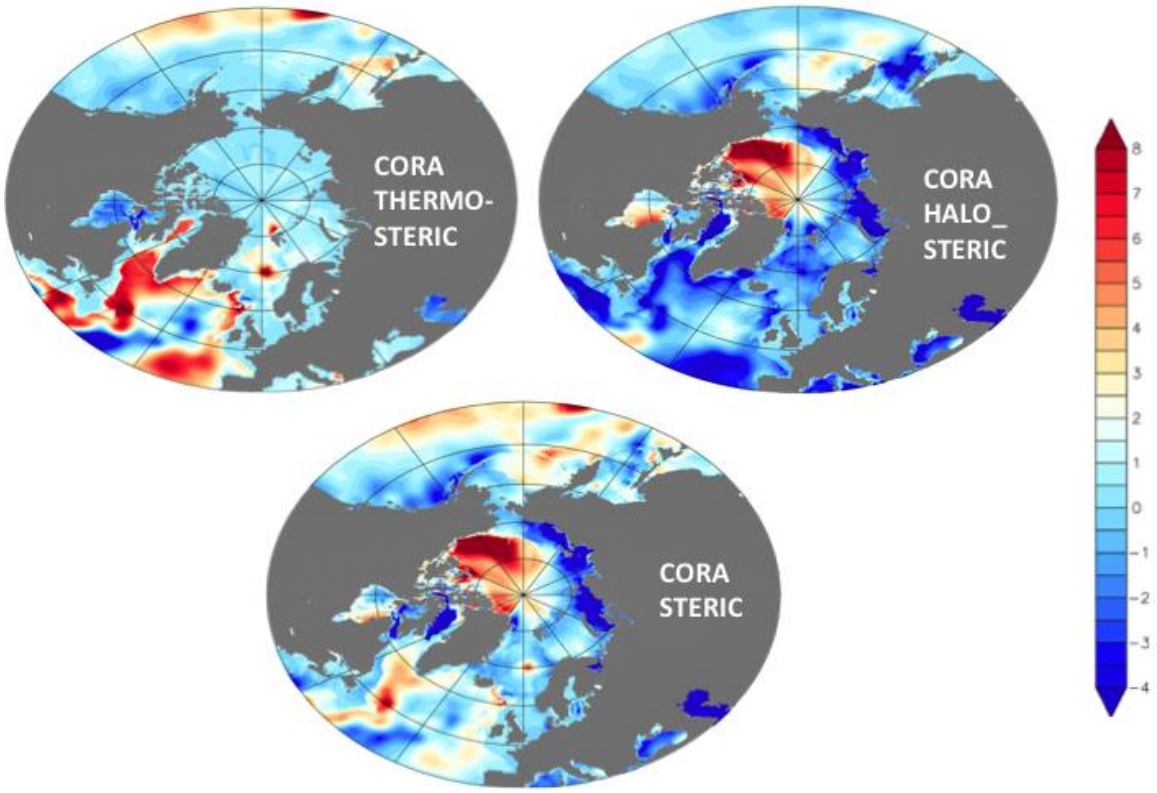

Figure 48:Trends (in mm/yr) in thermosteric (upper left), halosteric (upper right) and steric (lower) from the CORA hydrographic data for the time period 1993-2014.

Recently Counillon et al., (2016) reported on a study whereby sea surface temperature (SST) anomalies were assimilated into the ocean component of the coupled Norwegian Climate Prediction Model (NorCPM) for the period 1950 to 2010. The findings in the North Atlantic with particular focus on the Sub-Polar Gyre is very interesting and promising as shown in Figure 49. Here the Sub-Polar Gyre index (positive-weak; negative-strong) from NorCPM with and without assimilation of SST anomalies are inter-compared and assessed against the altimetry-based sea surface height anomalies from 1993 to 2010. As noticed there is clear reduction in the ensemble spread with assimilation included, and possible also a reduction with time. The ensemble mean in NorCPM shows distinct phases of positive and negative anomalies, that are not discovered in the free run simulations. Starting with a positive phase and weak gyre circulation from 1950-1970, a gradual strengthening of the gyre circulation takes place from 1970 to 1990. Since 1995, on the other hand, there has been a sharp transition towards a weak gyre circulation again peaking in 2005. Counillon et al (2016) find moreover that these phases of the gyre circulations are in good agreement with studies reported by Robson et al., (2012a, 2012b); Yeager et al., (2012); and Msadek et al., (2014). The very good agreement with the altimeter observations from 1993 is remarkable and indicates a very strong coupling between SST and sea level anomalies. This relationship might be highly

beneficial to advance the understanding of the thermodynamics of the Sub-Polar Gyre and its variability in relation to the annual to decadal variability of both the North Atlantic Current and the Atlantic Meridional Overturning Circulation (AMOC) (e.g. Rahmstorf er atl., 2015, Desbruyères, D., et al., 2015).

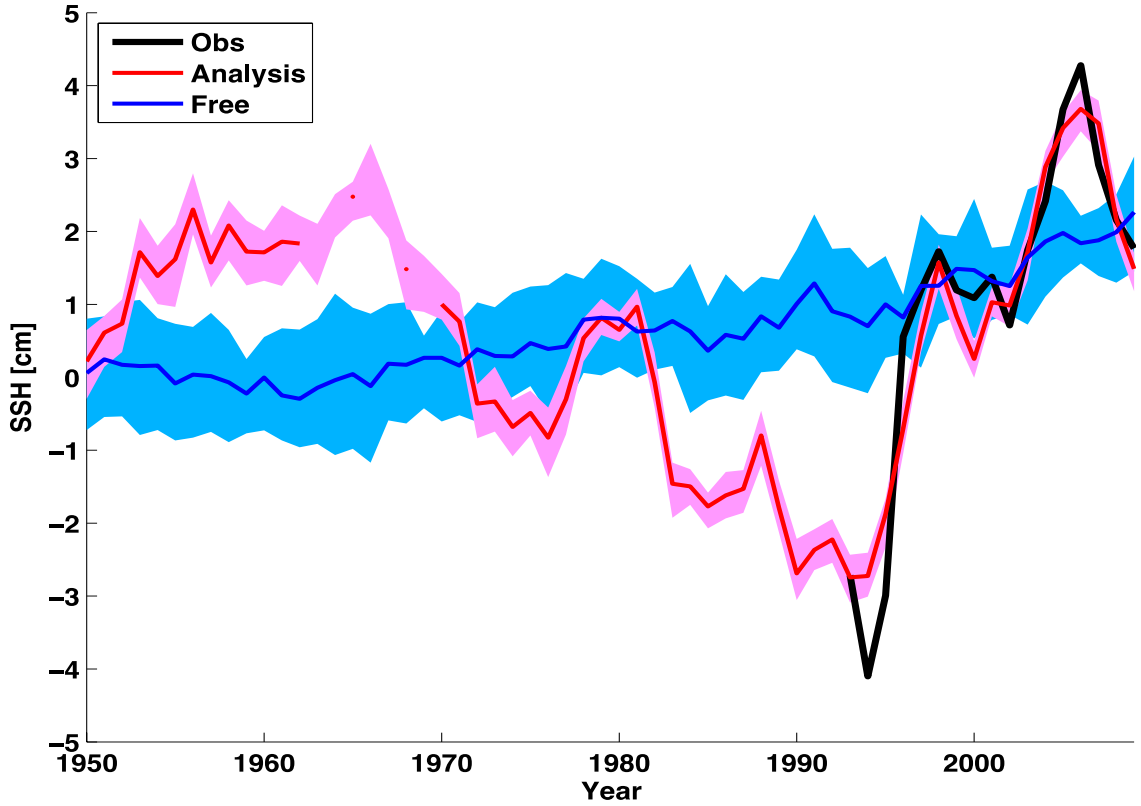

Figure 49: Subpolar Gyre index in NorCPM with assimilation (red), in the free run without assimilation (blue) and in altimeter-based satellite observations (black line). The shading represents the ensemble spread with and without assimilation.

1.3.5. Summary

The new ESA CCI Sea Level products have provided advanced opportunities for studies of sea level changes. The assessment of the ESA SL_ECV_V2 for the high latitude seas and the Arctic Ocean has focused on the Beaufort Gyre (BG), the Sub-Polar Gyre (SPG) and the Lofoten Basin (LB) in the Norwegian Sea. In so doing we have used the in-situ hydrography data from CORA (Cabanes et al., 2013), reanalyses from the TOPAZ4 operational system together with free runs from the NorESM and reanalyses from NorCPM with assimilation of SST. The inter-comparison and assessment have documented interesting results and sometimes very good agreement and consistency between observations and models. In particular the findings and achievements include distinct evidence of sea level rise of around:

- ✓ 4-5 mm/yr for the inner part of the SPG explained by the thermosteric contribution together with a barotropic source;
- ✓ 6-7 mm/yr for the central BG explained by the halosteric contribution and accumulation of fresh and cold Arctic water in the gyre;
- ✓ 3-4 mm/yr in the inner part of the LB assumed to result from the thermosteric contribution resulting from increased residence time of Atlantic Water in the basin.

In consistence with these findings, it is furthermore likely to conclude that a weakening of the anticlockwise circulation has occurred in the Sub-Polar Gyre during the last 20-25 years. In contrast the distinct sea level rise encountered in the Beaufort Gyre during the same period has lead to an intensification of the clockwise circulation in the gyre with possible trapping of more freshwater.

The coupled climate models, such as NorESM, are designed to provide projection of the Earth system changes at the global scale in the coming 100 years' time perspective. The regional inter-comparison of the NorESM fields to the ESA SL_ECV_V2 observations for the time period from 1993-2016 should therefore keep this in mind as the phases of changes in the coupled climate models may not necessarily exactly coincide with the observations. The assimilation of the SST fields in the coupled climate prediction model NorCPM, on the other, convincingly demonstrates the highly important impact to reduce the uncertainty in the reanalyses as well as to constrain the phases of the variability.

At the closing of this study it is highly appreciated that ESA under the Climate Change Initiative has supported the launch of a new extended cross-essential climate variable (ECV) study. This study is named Sea Level Budget Closure study and is coordinated by Technical University of Dresden in Germany with the following ECV´s included: - sea surface temperature; - sea level; - land water; - glaciers and ice sheets. Integrated to this is the gravity-based ocean mass signals.

1.3.6. References

Counillon, F., Keenlyside, N., Bethke I., Wang Y., Billeau, S., Shen M.-L. and Bentsen, M. (2016). Flow-dependent assimilation of sea surface temperature in isopycnla coordinates with the Norwegian Climate Prediction Model, Tellus A 2016, 68, 32437, http://dx.doi.org/10.3402/tellusa.v68.32437.

Cabanes, C., A. Grouazel, K. von Schuckmann, M. Hamon, V. Turpin, C. Coatanoan, F. Paris, S. Guinehut, C. Boone, N. Ferry, C. de Boyer Montégut, T. Carval, G. Reverdin, S. Pouliquen, and P. Y. Le Traon, 2013: The CORA dataset: validation and diagnostics of in-situ ocean temperature and salinity measurements. Ocean Science, 9, 1-18, http://www.ocean-sci.net/9/1/2013/os-9-1-2013.html, doi:10.5194/os-9-1-2013

Desbruyères, D., H. Mercier, V. Thierry (2015). On the mechanisms behind decadal heat content changes in the eastern subpolar gyre, Progress in Oceanography, March 2015, Vol. 132, pages 262-272.

Hatun, H., Sandø, A. B., Drange, H., Hansen, B., Valdimarsson, H., (2005). Influence of the Atlantic Subpolar Gyre on the Thermohaline Circulation. Science 309 (5742), 1841-1844.

Jiping Xie, Pavel Sakov, François Counillon, Laurent Bertino, Nicolas Finck, Christoph Renkl, COPERNICUS Quality Information Document, 2016.

Johannessen, J.A., R. P. Raj, J. E. Ø. Nilsen, T. Pripp, P. Knudsen, F. Counillon, D. Stammer, L. Bertino, O. B. Andersen, N. Serra and N. Koldunov (2014). Toward Improved Estimation of the Dynamic Topography and Ocean Circulation in the High Latitude and Arctic Ocean: The Importance of GOCE, *Survey in Geophysics*, Springer, DOI 10.1007/s10712-013-9270-y.

Msadek, R., Delworth, T., Rosati, A., Anderson, W., Vecchi, G. and co-authors. 2014. Predicting a decadal shift in North Atlantic climate variability using the GFDL forecast system. J. Clim. 27(17), 6472_6496.

Morison J, Kwok R, Peralta-Ferriz C, Alkire M, Rigor I, Andersen R, Steele M (2012). Changing Arctic Ocean freshwater pathways. Nature 481(7379):66–70. doi:10.1038/nature10705.

Rahmstorf, S., Box, J., Feulner, G., Mann, M., Robinson, A., Rutherford, S., Schaffernicht, E. (2015): Exceptional twentieth-Century slowdown in Atlantic Ocean overturning circulation. Nature Climate Change (online) - See more at: http://www.realclimate.org/index.php/archives/2015/03/whats-going-on-in-the-north-atlantic/#sthash.JA0XBfZ8.dpuf

Robson, J., Sutton, R., Lohmann, K., Smith, D. and Palmer, M. D. 2012a. Causes of the rapid warming of the North Atlantic Ocean in the mid-1990s. J. Clim. 25(12), 4116_4134.

Robson, J., Sutton, R. and Smith, D. 2012b. Initialized decadal predictions of the rapid warming of the North Atlantic Ocean in the mid 1990s. Geophys. Res. Lett. 39(19), L19713.

Yeager, S., A. Karspeck, G. Danabasoglu, J. Tribbia and H. Teng, (2012), A Decadal Prediction Case Study: Late Twentieth-Century North Atlantic Ocean Heat Content, Journal of Climate, DOI: 10.1175/JCLI-D-11-00595.1.

2. WP5200: Error characterization

2.1. Evaluation of the CCI sea level data through Sea Level Closure Budget Approach

2.1.1. Introduction

The global mean sea level (GMSL) budget is revisited during the whole altimetry era (January 1993 to December 2015) using a large number of data sets. This budget approach consists in computing the sea level components using different observing systems and model outputs, comparing their sum to the observed GMSL and estimating errors in one or several components.
The results of this study are available in Dieng et al., 2017.

Their approach:
- Allows quantifying the TOPEX-A altimeter drift and confirms the importance of correcting for this drift.

- Highlights that the use of an ensemble mean (EM) for each component of the sea level budget equation leads to better budget closure than when using individual data sets.

- Provides a new estimation of the GMSL rate
- The nearly zero residual trend (closure of the sea level budget) indicates that missing contributions (e.g., deep ocean warming) are still negligible (within 0.2 mm/yr)

2.1.2. Data

The dataset distributed by different groups have been taken into account for each sea level components as well as the ensemble mean of the different products. This includes:

- the altimeter GMSL,

- the steric sea level products,

- the glaciers time series,

- the Greenland and Antarctic ice mass loss components,

- the atmospheric water vapor content,

- the GRACE ocean mass contribution,

- the land water contribution,

- reservoirs and groundwater depletion.

For the steric data, three data sets have been used for January 1993 to December 2004 (updates from Ishii and Kimoto [2009] and from Levitus et al. [2012], plus the EN4 data set from Good et al. [2013] (see figure 50).
Another important source of GMSL interannual variability comes from terrestrial water storage in response to natural climate variability [e.g., Boening et al., 2012; Cazenave et al., 2014]. It can be quantified by using either GRACE space gravimetry over land [e.g., Fasullo et al., 2013] or global hydrological models. Here we use the latter approach. In addition to ISBA/TRIP, we also considered the Water Gap Hydrological Model [Döll et al., 2014a, 2014b], the Global Land Data Assimilation [Rodell et al., 2004], and the MERRA reanalysis [Mantas et al., 2015]. Comparison between detrended GRACE-based ocean mass (see Dieng et al. [2015a, 2015b] for information on the GRACE data) and detrended land water contribution (expressed in equivalent sea level) estimated with the four hydrological models over January 2003 to December 2015 led us to only consider ISBA/TRIP because of its higher correlation (of 0.95) with the ocean mass component (see Figure 51).

See Figure 50 and Figure 51 for the associated time series. More details are provided in Dieng et al., 2017.

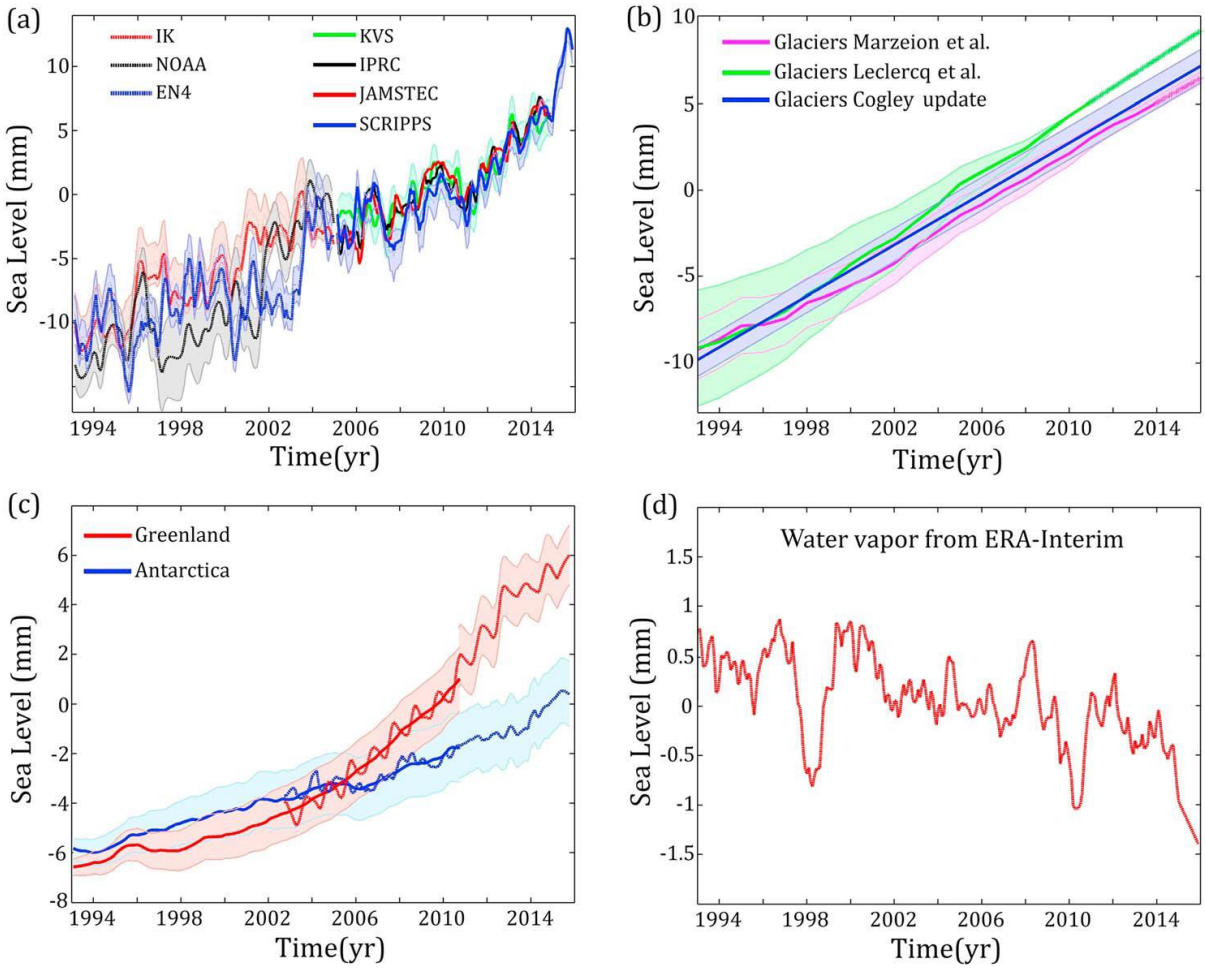

Figure 50: (a) Global mean steric sea level time series from IK, NOAA, and EN4 for January 1993 to December 2004 and Argo (data from update of von Schuckmann and Le Traon [2011], noted KVS, IPRC, JAMSTEC, and SCRIPPS) for January 2005 to December 2015. (b) Glacier component (data from Marzeion et al., Leclercq et al., and Cogley et al.—version R1501-). (c) Greenland and Antarctica components from IMBIE for 1993-2010 and CCI for May 2002 to December 2015. (d) Water vapor contribution expressed in equivalent sea level (data from ERA-Interim). For all curves, shaded areas represent 1 standard deviation uncertainty.

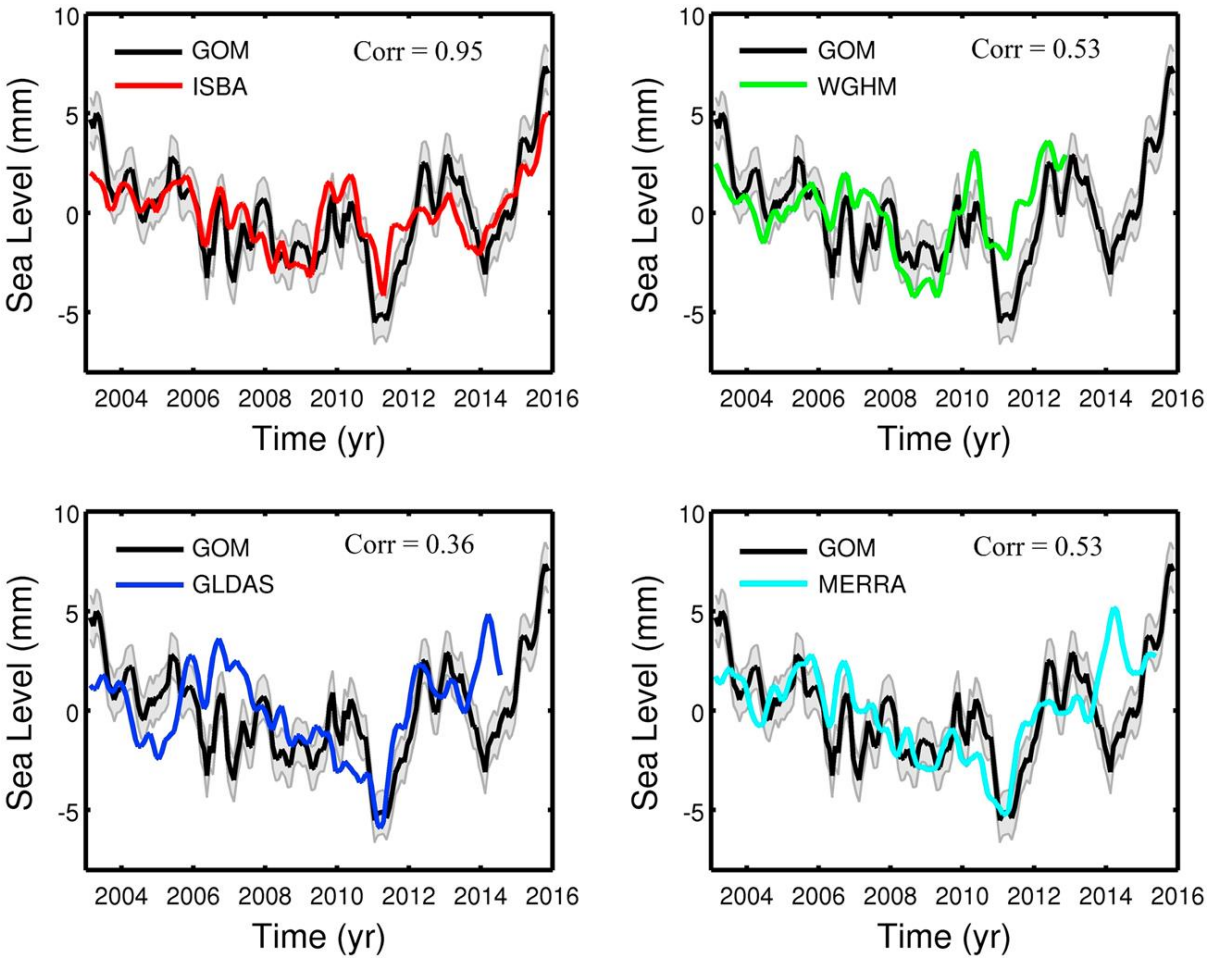

Figure 51: Detrended GRACE-based ocean mass (GOM; black curve) (data processed in Dieng et al. [2015b]) and detrended land water contribution from four hydrological models (colored curves) over 2003-2015. The correlation between detrended ocean mass and models is indicated.

Considering the different altimeter GMSL record, Figure 52 illustrates that the smallest residual compared to the ensemble mean is obtained with the SL_cci product (V2.0).

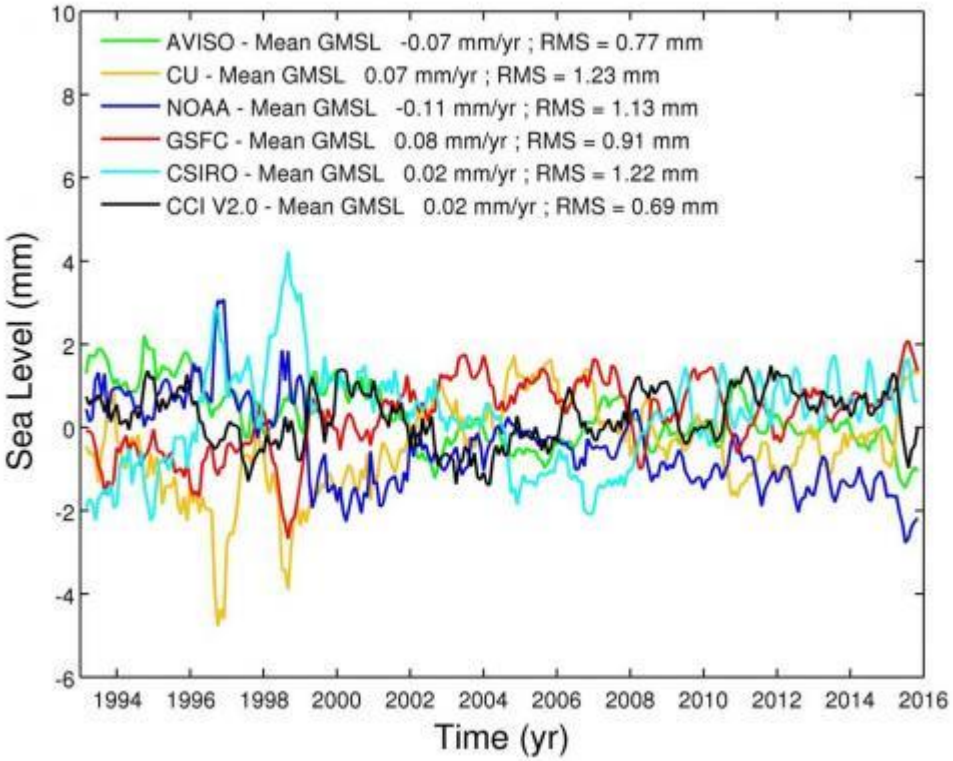

Figure 52: Different time series between individual GMSL products and the ensemble mean. Source: LEGOS.

2.1.3. Results

Figure 53a compares the EM GMSL (average of the six products) with the sum of all components over January 1993 to December 2015. We note very good agreement between observed EM GMSL and sum of EM components, except at the beginning of the record (from January 1993 to December 1998). It is attributed to the TOPEX-A instrumental drift. This budget closure approach allows estimating this drift to 1.5 +/- 0.5 mm/yr, in agreement with Watson et al., 2015 (see Dieng et al., 2017 for more details).

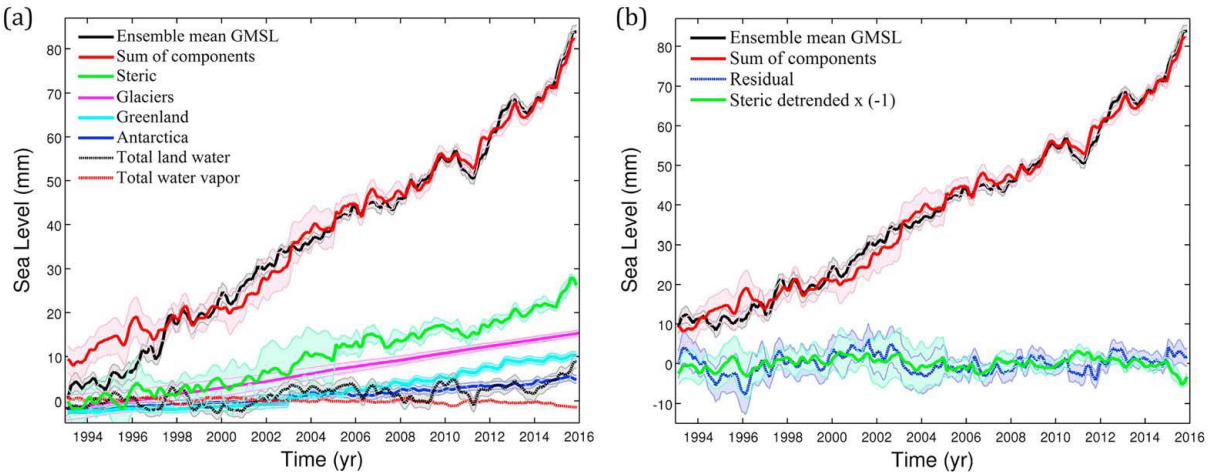

Figure 53: (a) EM GMSL without TOPEX A drift correction (black curve), sum of EM components (red curve), and individual EM components over January 1993 to December 2015. Shaded areas represent one standard error as described in text. (b) EM GMSL with TOPEX A drift correction (black curve), sum of the EM components (red curve), and residuals (calculated as the difference between EM GMSL and sum of EM components) over January 1993 to December 2015. The detrended EM steric component (multiplied by -1) is superimposed to the residual curve. Shaded areas represent one standard error as described in text.

The 1.5 mm/yr drift value is applied to the 1993–1998 EM GMSL time series. Figure 53b shows the corrected EM GMSL together with the sum of EM components. The residual time series (i.e., the difference between corrected EM GMSL and the sum of EM components) is also shown. The residual trend over 1993–2015 amounts to 0.03 ± 0.22 mm/yr, indicating closure of the sea level budget within ~0.2 mm/yr.

Accounting for the TOPEX A drift correction has another implication. As previously noticed by Watson et al. [2015] for the period 1993 to mid-2014, the new EM GMSL rate amounts to 3.0 ± 0.15 mm/yr for the 1993–2015 time span, a value lower than the 3.3 mm/yr rate generally reported [e.g., Ablain et al., 2017]. The EM GMSL rate is significantly lower during the first period compared to the second one (2.7 ± 0.2 mm/yr versus 3.5 ± 0.15 mm/yr). This 0.8 mm/yr EM GMSL increase dominantly results from increased land ice loss from Greenland (+0.5 mm/yr), while slight increases are also noticed for all other components (except for the water vapour component that shows slightly larger negative contribution).

2.1.4. Conclusion

In this study, the sea level budget has been investigated over the altimetry era (1993–2015) by comparing the temporal evolution of GMSL and the sum of the components using a large number of data sets and computing ensemble means for all terms of the sea level budget equation. The results confirm, as in previous studies, the importance of correcting for TOPEX A instrumental drift. The new approach based on the GMSL budget indicates a drift of 1.5 ± 0.5 mm/yr, in agreement with the preferred value of Watson et al. [2015] but lower than Zawadzki et al. [2016]. Applying this correction over the first 6 years of the altimetry record leads to lower GMSL rate (of 3.0 ± 0.15 mm/yr) over the altimetry era than previously assumed. More importantly, the GMSL rise since the mid-2000s shows significant increase compared to the 1993–2004 time span. This contradicts conclusion of previous studies [e.g., Cazenave et al., 2014] that reported slowing down of about 30% of the GMSL rise during the years 2000s (without TOPEX A drift correction), attributed to La Niña events. Here we show that in spite of the several temporary sea level drops caused by La Niña events, the GMSL rise has increased during the last decade.

Slower rate during the first decade of the altimetry era may result from lower contributions, including the persistent cooling impact of the 1991 Mount Pinatubo eruption as proposed by Fasullo et al. [2016]. Finally, our analysis shows that the use of an ensemble mean for each component of the sea level budget equation leads to better budget closure than when using individual data sets. The nearly zero residual trend indicates that missing contributions (e.g., deep ocean warming) are still negligible (within 0.2 mm/yr).

2.1.5. References

Boening C., J. K. Willis, F. W. Landerer, and R. S. Nerem (2012), The 2011 La Nina: So strong, the oceans fell, Geophys. Res. Lett., 39, L19602, doi:10.1029/2012GL053055.

Cazenave, A., H. Dieng, B. Meyssignac, K. von Schuckmann, B. Decharme, and E. Berthier (2014), The rate of sea level rise, Nat. Clim. Change, 4, 358–361, doi:10.1038/NCLIMATE2159.

Dieng, H. B., H. Palanisamy, A. Cazenave, B. Meyssignac, and K. von Schuckmann (2015a), The sea level budget since 2003: Inference on the deep ocean heat content, Surv. Geophys., 36, 209–229, doi:10.1007/s10712-015-9314-6.

Dieng, H. B., A. Cazenave, K. von Shuckmann, M. Ablain, and B. Meyssignac (2015b), Sea level budget over 2005–2013: Missing contributions and data errors, Ocean Sci., 11, 789–802, doi:10.5194/os-11-789-2015.

Dieng, H. B., A. Cazenave, B. Meyssignac, *and* M. Ablain *(*2017*),* New estimate of the current rate of sea level rise from a sea level budget approach, Geophys. Res. Lett., 44, *doi:*10.1002/2017GL073308.

Döll, P., M. Fritsche, A. Eicker, and S. H. Mueller (2014a), Seasonal water storage variations as impacted by water abstractions: Comparing the output of a global hydrological model with GRACE and GPS observations, Surv. Geophys., doi:10.1093/gji/ggt485.

Döll, P., H. Mueller Schmied, C. Schuh, F. T. Portmann, and A. Eicker (2014b), Global-scale assessment of groundwater depletion and related groundwater abstractions: Combining hydrological modeling with information from well observations and GRACE satellites, Water Resour. Res., 50, 5698–5720, doi:10.1002/2014WR015595.

Fasullo, J. T., C. Boening, F. Landerer, and R. S. Nerem (2013), Australia's unique influence on global mean sea level in 2010–2011, Geophys. Res. Lett., 40, 4368–4373, doi:10.1002/grl.50834.

Good, S. A., M. J. Martin, and N. A. Rayner (2013), EN4: Quality controlled ocean temperature and salinity profiles and monthly objective analyses with uncertainty estimates, J. Geophys. Res. Oceans, 118, 6704–6716, doi:10.1002/2013JC009067.

Ishii, M., and M. Kimoto (2009), Reevaluation of historical ocean heat content variations with time-varying XBT and MBT depth bias corrections, J. Oceanogr., 65 (3), 287–299, doi:10.1007/s10872-009-0027-7.

Levitus S., et al. (2012), World ocean heat content and thermosteric sea level change (0–2000 m), 1955–2010. Geophys. Res. Lett., 39, L10603. doi:10.1019/2012GL051106.

Mantas, V. M., Z. Liu, and A. J. S. C. Pereira (2015), A web service and android application for the distribution of rainfall estimates and Earth observation data, Comput. Geosci., 77, 66–76, doi:10.1016/j.cageo.2015.01.011.

Rodell, M., et al. (2004), The Global Land Data Assimilation System, Bull. Am. Meteorol. Soc., 85 (3), 381–394.